Glasses in colloid-polymer mixtures

Khoa Nguyen Pham

Thesis submitted for the degree of Doctor of Philosophy

School of Physics
University of Edinburgh
2003

To my parents

Abstract

This work consists of detailed experimental studies of the structure and dynamics of glassy states in hard spheres with short-range attraction. The well-characterized model system is a suspension of nearly-hard-sphere colloidal particles and non-adsorbing linear polymer which induces a depletion attraction between the particles.

Observation of crystallization reveals a re-entrant glass transition where the glass melts and freeze again upon increasing attraction at high volume fraction. Static light scattering shows a continuous change in the static structure factors across the re-entrant region. Dynamic light scattering results, which cover 11 orders of magnitude in time, are consistent with the existence of two distinct kinds of glasses, those dominated by inter-particle repulsion and caging, and those dominated by attraction. Samples close to the 'A3 point' predicted by mode coupling theory for such systems show very slow, logarithmic dynamics.

To measure the slow dynamics of non-ergodic glassy samples, a simple ensemble averaging method in dynamic light scattering, the echo technique, was developed. By rotating the sample continuously many sub-ensembles are probed thus the measured intensity correlation function contains peaks whose height follow the sample's true dynamics. The technique is described by a simple theoretical model and verified by computer simulations. It is shown that the profile of the peak is not affected by sample dynamics, hence imperfect rotation can be corrected. This technique allow me to measure dynamics over a relaxation time range from 1 to beyond 10^4 seconds in rel-

atively short measurement time. The technique can be used with any light scattering setups and thus has large potential in a wide range of applications where the dynamics of slowly-relaxing or non-ergodic samples is of interest.

Declaration

The work described in this thesis was carried out by myselft alone, except where otherwise indicated in the text. This thesis has been composed by myself and has not been submitted in any previous application for a degree.

Khoa Nguyen Pham

Acknowledgements

I would like to thank all the people who have given me advice, support and encouragement during the course of this work. First of all are my supervisors: Stefan Egelhaaf with extended discussions, Wilson Poon with his ingenious ideas, many of which I wish I had time and chance to persue, and Peter Pusey with his expertise in light scattering. Without their advice and guidance this work would not be possible.

My thanks also go to Andy Schofield, Abdellatif Mossaïd, George Petekidis, Matthias Fuchs and Mike Cates for very fruitful discussions and collaboration. I'd also like to thank my office mates with whom I have shared more than just space.

Many thanks to An and our 'gang' of friends in Glasgow and further afield, with their endless parties which kept me occupied most weekends. Also thanks to Vicent who suffers inconvenience I have caused at the flat.

Special thanks to my parents who have taught me how to live my life, and to Kim who gives me love. Despite not being here, they were always there.

Contents

List of Figures

List of Tables

Chapter 1

Introduction

1.1 Colloids

Colloid is the term used to describe a class of mesoscopic-sized objects suspended in another medium, usually liquids. These objects are nanometer to micrometer in size, much larger than molecules. They comes in many forms: macro-molecules (polymer chains, DNA,...), solid particles (latex, metal particles,...), liquid droplets (fat, oil, surfactant solutions,...), or biological matters (red blood cell, viruses,...). The variety of real life complex substances colloids represent makes them interesting in their own right for their many practical applications.

In the view of fundamental physics, colloids are small enough that statistical mechanics is relevant, yet they're large enough that their structure can be probed by light, their dynamics is slow enough (in the time scale of microseconds and longer) to be followed. Therefore colloids are good candidates to study phase behaviour and other fundamental phenomena as mesoscopic models of their molecular counterpart.

1.2 Colloids as hard-spheres

The simplest thermodynamic system other than ideal gas modelled by colloids is a collection of N hard spheres of radius R suspended in a liquid (solvent) with total volume V. The spherical particles do not interact except for an infinite hard core repulsion. There is only one thermodynamic variable to characterize the system: density — expressed as a dimensionless *volume fraction* $\phi = (4/3)\pi NR^3/V$. Hard-spheres are athermal, i.e. there is no temperature scale for them since the interaction potential presents no energy scale, the only thermodynamic driving force in play is entropy. Despite its simplicity, a hard-sphere system shows a complex phase behaviour [1, 2]. At low volume fraction, hard-spheres exist as an orderless fluid. In the range of volume fraction $0.494 < \phi < 0.545$, it develops a crystal phase at $\phi_m = 0.545$ coexisting with the fluid phase at $\phi_f = 0.494$. With ϕ above 0.545, the whole systems is crystalline. Even though there is no theory accounts for the exact values of the freezing and melting volume fractions of hard-spheres, experiments and simulations [1, 2, 3] agree well at the values quoted above. The phenomenon of colloid hard spheres freezing into a crystalline state, sacrificing configurational entropy of the system, is to increase local entropy of individual particles so that the total entropy is maximized. According to equilibrium thermodynamics, this crystalline phase is the most stable phase up to the maximum possible volume fraction of close packing $\phi_{\text{cp}} = \pi/3\sqrt{2} \approx 0.74$. However, the homogeneous crystallization of hard-spheres stops at volume fraction $\phi_g \approx 0.58$ [1, 2, 4]. Above this volume fraction, the system is stuck in a non-equilibrium state with fluid-like structure and frozen dynamics [2, 5, 6]. The volume fraction ϕ_g at which this happens is the *glass* transition for hard-spheres.

1.3 Glasses

1.3.1 Molecular glass

The term 'glass' is commonly used to describe materials that have an amorphous arrangement of molecules (particles) just like in a liquid, yet they are solid, i.e. do not flow and can withstand finite stress at zero frequency. Glasses can be obtained via many pathways, but the most common one is to cool a liquid quickly below a certain temperature. During cooling, the heat capacity C_p at constant pressure shows a sudden drop from a liquid-like value to a crystal-like value due to the loss of liquid degrees of freedom. The temperature at which this occurs is referred to as the *'glass transition temperature'*. Molecular substances that form glasses are divided into 2 types: *strong* and *fragile* glass formers depending on the behaviour of their viscosity in the temperature range leading up to the glass transition [7].

Glasses are non-equilibrium states, where the system prefers to get to the thermodynamically favourable state (crystalline) but is stuck kinetically forever or for an extremely long time. This is an interesting state of matter which many studies has been devoted to [7]. Studies of non-equilibrium states would shed light on the fundamental mechanisms of how they got stuck, and the kinetic path-way to equilibrium.

1.3.2 Colloidal glass

When colloids are used as models for molecules, the colloidal particles in suspension take the place of molecules and the suspending liquid is considered only as an environment for the system. There are however major differences of the models and molecular systems. First colloidal particles undergo Brownian motion in the bath of solvent rather than ballistic motion of molecules in vacuum. Nevertheless, those motions are in the time scale much smaller than that of the glass transitions so that the exact nature of

each individual microscopic motion is not directly relevant.

Secondly, colloidal particles are much larger than molecules and in constant exchange of momentum with the molecules of the (constant temperature) suspending liquids. Thus temperature does not play a very important role in the behaviour of colloidal suspensions. The important control parameters are volume fraction (density) and, in the case of non-hard-spheres, interaction strength between colloidal particles in unit of k_BT, where k_B is the Boltzmann's constant and T is temperature. The criterion for identifying the glass transition in colloids therefore takes a microscopic approach. It is accepted that a colloidal suspension reaches a glass transitions when the particle dynamics does not fully relax and homogeneous crystallization stops.

Practically, there are direct applications in understanding the colloidal glass transition. In cases where dense crystals are the desirable products, like green bodies in ceramic industry [8], or fabrication of colloidal crystals for photonic applications [9], knowing how to overcome the glass transition would be useful. In other applications where dense, glassy states are desirable, or crystallization and phase transitions are to be avoided, like in foodstuffs, cryo-biology, knowing how to enter the glass state quickly is of great help.

1.4 Hard-spheres with attraction

A natural extension to the hard-sphere system is to add attraction to make it closer to molecular substances. There are several ways to realize this experimentally, but the most controllable way is by adding non-adsorbing polymer coils to a suspension of colloids [10, 11]. The center of mass of a polymer coil of radius of gyration r_g is excluded from a zone of width r_g from the surface of each colloid. When two colloids come close enough to each other so that their polymer-excluded regions overlap, the imbalance in polymer osmotic pressure pushes them together. A model system of this

type has been studied extensively over the last decade [12], showing many features of a molecular systems: crystallization as first order phase transition, gas-liquid transitions, critical point and triple point of gas-liquid-crystal coexistence [13], gels and glasses [14, 15]. Therefore colloid-polymer mixtures were chosen as the experimental system of study in this work.

The colloid-polymer mixture approach to model attraction in hard-sphere systems carries two major advantages. Firstly, the two parameters characterizing the attraction — the range and depth of the attractive potential — can be easily fine-tuned experimentally. The dimensionless range of the attraction can be estimated by the ratio $\xi = r_g/R$, while its strength U_{max} is governed by the concentration of polymer. The three parameters ξ, ϕ, and U_{max} (at constant temperature) are the control parameters and determine the behaviour of the system. Secondly, this system can be implemented as an extension to the well-characterized hard-sphere colloids. Thus all experimental methods and data interpretation can start from a well-founded reference.

1.5 How to study them

There are two main microscopic descriptions that determine the state of matter: the structure — arrangement of particles relative to each other, and the dynamics — how particles move over time. Studying the structure and dynamics of a system as it crosses a glass transition will be very useful in the quest to understand the mechanisms of the glass transition.

From the early time of colloids study, light scattering has been used as a very good probe to measure the structure and dynamics of colloidal systems. Light scattering techniques essentially probe the magnitude and fluctuation in different Fourier components of the system density by shining a coherent beam of light to a sample and detect the scattered light as functions of time and scattering angle. The variations of averaged

scattered light intensity with scattering angles gives information about the structure of the system. The fluctuation of scattered intensity in time on the other hand gives information about the movement of particles inside the scattering volume: the dynamics of the system.

Recently, advances in technology enable microscopy to be used widely to look directly at microscopic structure and dynamics of colloids [6, 16, 17]. Microscopy is particularly good at studying local structure and single particle dynamics. Despite that, light scattering still has certain overwhelming advantages in some areas. First, it does not need to resolve each particles, thus allows the use of particles as small as one-tenth of the wavelength of light. Secondly, the scattering volume probed is much larger than the particle size, thus at any one time, scattered information is obtained from typically 10^8 particles, giving rise to very good statistics and low noise.

1.6 Aims and thesis layout

This work aims at studying the structure and dynamics of colloidal hard-spheres with a short-range depletion-induced attraction near the glass transitions for an experimental model system: nearly-hard-spheres polymethylmethacrylate (PMMA) colloids and linear polystyrene mixtures. The study used light scattering methods to measure the static structure factors and dynamic structure factors of samples near the glass transitions of the system, particularly at high volume fraction.

Chapter 2 lays out the theoretical background needed in carrying out this work and relevant in discussing results. It reviews equilibrium theoretical treatment for the colloid-polymer mixture, mode coupling theory predictions on the glass transitions in similar systems, and theories of light scattering methods. Chapter 3 describes in detail a new dynamic light scattering (DLS) method, the echo technique, developed during the course of this work. This technique allows measuring ensemble-averaged dynamics

from non-ergodic samples in relatively short measurement time with improved accuracy. Echo DLS was used in conjunction with other methods to obtain dynamics data for this work. Chapter 4 describes the methods and procedures used in preparing and calibrating samples, and in measuring their structure and dynamics. Chapter 5 shows results of the work, discussing their relevance and interpretation along the way. Finally, chapter 6 summarizes all the main results and understanding of the work, also suggests other directions further studies should pursue to gain more insight into the physics of the glass transitions.

Chapter 2

Theoretical background

2.1 Colloid-polymer mixtures and equilibrium theory

2.1.1 Colloid-polymer mixtures and depletion potential

Experimentally, colloid-polymer mixtures have been used extensively as a model of colloidal hard-sphere with depletion-induced attraction [12]. The attraction arises from the depletion phenomenon of non-adsorbing polymer coils from the surface of colloid particles first described by Asakura and Oosawa [10]. The centres of mass of any polymer coils with radius of gyration r_g are excluded from a region of width about r_g from the surface of any colloid particles (Fig. 2.1(a)). When two colloids come close enough so that their polymer excluded regions overlap, more free volume accessible to polymers is created, increasing the entropy of polymer coils. This creates an effective attraction between the colloid particles. The attraction can also be seen as the result of an imbalance in osmotic pressure by the polymer coils.

This 'effective' depletion attraction between two colloid particles of radius R has an

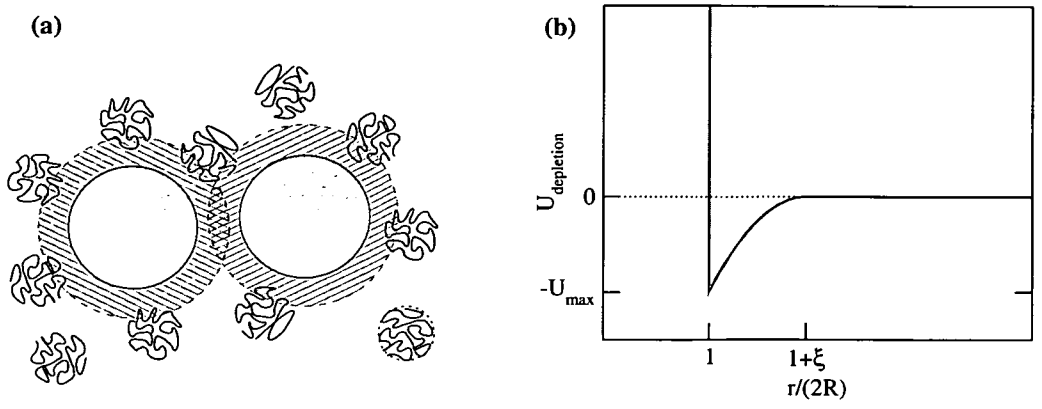

Figure 2.1: (a) Attraction due to overlapping of polymer-depleting volume around each colloid. The center of the polymer coils cannot enter the depleting hashed region around the colloid. When two colloids come close together so that their depletion layers overlap, there is more room for the polymer coils because the total depleted volume is now reduced. The increase in entropy of polymer coils effectively creates an attraction between the 2 colloids. (b) Asakura-Oosawa deleption attraction potential. The depth $U_{\max}$ is proportional to the polymer concentration in the volume accessible to the centres of the coils and the dimensionless range is determined by the size ratio ξ.

infinite hard-core repulsion at touching, particles' centre-to-centre distance $r = 2R$. The attrative well starts with a minimum at touching and increases to zero at $r = 2(R+r_g)$. The dimensionless range of the attractive potential is the size ratio $\xi = r_g/R$. In the case of $\xi < 2/\sqrt{3} - 1 \approx 0.15$, any one polymer coil can only touch at most two colloids at the same time, so the depletion interaction is purely pair-wise. The potential is well described [11, 18] by the Asakura-Oosawa form [10] (Fig. 2.1(b)):

$$U = \begin{cases} +\infty & \text{for } r \leq 2R \\ -\Pi_p V_{overlap} & \text{for } 2R < r < 2R + 2r_g \\ 0 & \text{for } r > 2R + 2r_g \end{cases}, \tag{2.1}$$

where Π_p is the osmotic pressure of polymer, $V_{overlap}$ is the overlap volume of the depleted regions, given by:

$$V_{overlap} = \left(1 - \frac{3r}{4R(1+\xi)} + \frac{1}{2}\left[\frac{r}{2R(1+\xi)}\right]^3\right) \frac{4\pi R^3}{3}(1+\xi)^3 . \tag{2.2}$$

When the polymer coils are in a theta-solvent, they are assumed to behave like ideal

gas. They do not interact with each other and are confined to the (dynamic) free volume available to them, V_{free}, which is the volume not occupied by colloids or their associated depletion regions. With this assumption, the polymer osmotic pressure is proportional to its number concentration n_p^{free} in V_{free}:

$$\Pi_p = n_p^{\text{free}} k_B T, \tag{2.3}$$

where $n_p^{\text{free}} = \frac{N_p}{V_{\text{free}}}$ with N_p the total number of polymer coils in the sample.

The actual free volume can be expressed as a fraction of the total volume $V_{\text{free}} = \alpha V$. The fraction α depends firstly on the colloid volume fraction ϕ as each colloid excludes polymer from a volume of $(4/3)\pi R^3(1+\xi)^3$. Secondly, since these excluded volumes can overlap, α also depends on how much they overlap. Equivalently α is a function of all colloid positions which in turn depend on polymer concentration. Therefore α is a complicated function of the colloid structure that is not easily obtained. However, one can approximate α from ϕ and ξ from scaled particle theory [19]:

$$\alpha = (1-\phi)\exp[-A\gamma - B\gamma^2 - C\gamma^3], \tag{2.4}$$

where $\gamma = \phi/(1-\phi)$, $A = 3\xi + 3\xi^2 + \xi^3$, $B = 9\xi^2/2 + 3\xi^3$, and $C = 3\xi^3$.

This approximation completely ignores the effect of polymer on the structure of colloids, and thus is not expected to work well, especially at high ϕ. Therefore to avoid unnecessary uncertainties, most experimental results use the mass concentration of polymer in the whole system, c_p, which is directly determined experimentally, as an alternative variable to describe the composition of the system [19]:

$$c_p = \frac{M_p N_p}{V}, \tag{2.5}$$

where M_p is the mass of one polymer coil and V is the total volume of the system. Conversion from c_p to the free polymer concentration is possible using the approximation of the free volume fraction α above. Note that α is also a function of the colloid volume fraction ϕ:

$$c_p = M_p \alpha(\phi) n_p^{\text{free}}, \tag{2.6}$$

or in terms of mass concentration in the free volume:

$$c_p = \alpha(\phi) c_p^{\text{free}} \ . \tag{2.7}$$

2.1.2 Equilibrium theory

It is well-known in experiment [1, 2] and simulation [3] that the freezing and melting volume fractions in hard-sphere systems are 0.494 and 0.545 respectively. Equilibrium thermodynamic theory [19] accounts for the change in melting and freezing transitions when attraction is added, as well as the introduction of a liquid phase for ξ above a critical value. The theoretical treatment is described in detail in [19, 20]. Experimental observations of equilibrium phases were reported in [13, 15]. This section will only summerize the key points of the theory for small ξ relevent to this work.

Consider a system of fixed volume V containing N_c hard-sphere colloids and N_p non-interacting ideal polymer coils behaving as ideal gas. The polymer is however only free to explore the free volume αV available to it. The system is in equilibrium with a reservoir containing a polymer solution of chemical potential μ_p. Since the number of colloids N_c is fixed but N_p is allowed to vary, the semigrand partition function Ξ which integrates over all values of N_p must be used.

The semigrand potential that needs to be minimized is derived from the semigrand partition function [20]:

$$H = -k_B T \ln \Xi \tag{2.8}$$

$$= F_c - k_B T n_p^{\text{free}} \alpha(\phi) V \ , \tag{2.9}$$

where F_c is the Helmholtz free energy for a hard-sphere colloid system that can be derived from the appropriate hard-sphere equation of state.

When colloidal fluid and crystal phases coexist in equilibrium, colloid osmotic pressure p_c and chemical potential μ_c, as well as polymer chemical potential — or equivalently n_p^{free}, have to be equal in the two phases. Keeping n_p^{free} constant, p_c and μ_c

can be derived from the dimensionless free energy concentration $h(\phi) = \frac{H}{k_BT}\frac{4\pi R^3}{3V}$ by applying simple changes in thermodynamic variables:

$$\mu_c = \frac{dh}{d\phi} \tag{2.10}$$

$$p_c = -\frac{3k_BT}{4\pi R^3}\left[h - \phi\frac{dh}{d\phi}\right] . \tag{2.11}$$

Using different expressions for F_c for the colloidal hard-sphere fluid and crystal, then equating μ_c and p_c of the two phases simultanously, one can find the coexisting volume fractions of the fluid and solid phase. Note that from Eqs. 2.10 and 2.11, μ_c and p_c are the slope and the intercept, respectively, of the tangent to $h(\phi)$. Therefore solving the simultaneous equations can be done by finding the common tangent to the two curves representing fluid and solid free energies: $h_f(\phi)$ and $h_s(\phi)$. A common tangent of $h_f(\phi)$ between its two minima will reveal the gas-liquid coexisting volume fractions.

An arbitrary integration constant in obtaining F_c from the hard-sphere equations of state is calibrated so that for pure hard-sphere (i.e. $n_p^{\text{free}} = 0$), the volume fractions of coexisting fluid and crystal are 0.494 and 0.545 respectively. Then the same constant is used with increasing value of n_p^{free} to find the coexisting volume fractions of mixtures with polymer. The calculated state points (ϕ, n_p^{free}) could be converted to the experimental state points (ϕ, c_p), by using eq. 2.6 and the approximated free volume fraction $\alpha(\phi)$ (eq. 2.4) with the corresponding ϕ for fluid and solid.

Equilibrium theory predicted that on increasing attraction, the fluid-crystal coexistence gap increases for small ξ and regions of coexistence of gas, liquid, and crystal appear for large ξ [19]. This was indeed observed by experiments [13, 15] and computer simulations [21]. Apart from the equilibrium states predicted by equilibrium theory, experiments also reveals that there exist other non-equilibrium states in colloid-polymer mixtures when either the colloid volume fraction or polymer concentration is high enough [14, 15, 22].

2.2 Mode coupling theory (MCT)

Mode coupling theory was used to explain and predict glass transitions in many systems. It essentially takes into account the 'coupling', or feedback between different modes of density fluctuation. At some critical conditions, the coupling becomes so strong that it prevents the fluctuations to decay completely, trapping the system in a non-ergodic glassy state. MCT has successfully predicted many features of the glass transition in hard-sphere systems [5], as well as many atomic ones [23]. Though successful in many areas, MCT is not a very comprehensive theory as to the underlying physics of the glass transition [24]. A detailed formalism of the theory is laid out in [25, 26]. This section will review the relevant key concepts in my understanding of the theory.

2.2.1 Structure and dynamics

First let us define the concepts of structure and dynamics of a colloidal system. Consider a colloidal suspension of N identical particles, the centres of which are located at $\mathbf{r}_j$, $j = 1, 2, \ldots, N$. One can define a $3N$-dimensional vector $\mathbf{r}^N$ as a collective position of all particles in the system. As particles move in time, their positions are functions of time t. The density of the system can be defined as delta functions at the particle centres:

$$\rho(\mathbf{r}, t) = \sum_{j=1}^{N} \delta(\mathbf{r} - \mathbf{r}_j(t)). \tag{2.12}$$

Its spatial Fourier transform is

$$\rho(\mathbf{q}, t) = \sum_{j} e^{i\mathbf{q}\cdot\mathbf{r}_j(t)} \tag{2.13}$$

The structure of the system in the wavevector q domain can be expressed as the static structure factor (SSF):

$$S(q) = \langle \rho(\mathbf{q})\rho^*(\mathbf{q}) \rangle , \tag{2.14}$$

where ρ^* is the complex conjugate of ρ, both of which are taken at the same time; and the angle brackets are ensemble average.

For the dynamics of the sample, the normalized collective dynamic structure factor (DSF) $f(q,\tau)$ describes the correlation in density fluctuation after a delay time τ:

$$f(q,\tau) = \frac{\langle \rho(\mathbf{q},0)\rho^*(\mathbf{q},\tau)\rangle}{\langle \rho(\mathbf{q})\rho^*(\mathbf{q})\rangle} \tag{2.15}$$

2.2.2 MCT formalism

For colloidal suspensions at time scales larger than the Brownian time scale, i.e. after the colloid particles have lost their initial momemtum to the solvent, the Langevin equation of motion for colloids can be reduced to Smoluchowski equation of motion, which describes the evolution of the position distribution function $P(\mathbf{r}^N(t))$ [27]:

$$\frac{\partial P(\mathbf{r}^N)}{\partial \tau} = \mathcal{O} P(\mathbf{r}^N)\,, \tag{2.16}$$

where $\mathcal{O}$ is the Smoluchowski operator:

$$\mathcal{O} = \sum_{i,j=1}^{N} \nabla_i \cdot \mathbf{D}_{ij}(\mathbf{r}^N) \cdot \left(\nabla_j + \frac{1}{k_B T}\nabla_j U(\mathbf{r}^N)\right), \tag{2.17}$$

with $\mathbf{D}_{ij}$ the diffusion tensor that generally depends on the configuration $\mathbf{r}^N$ of the system and includes hydrodynamic interactions.

The time correlation function of any two configuration-dependent functions $u(\mathbf{r}^N(t))$ and $v(\mathbf{r}^N(t))$ can be derived from Eq. 2.16:

$$\langle u(0)v(\tau)\rangle = \left\langle u(0)\exp(\tilde{\mathcal{O}}\tau)v(0)\right\rangle, \tag{2.18}$$

where $\tilde{\mathcal{O}}$ is the adjoint Smoluchowski operator:

$$\tilde{\mathcal{O}} = \sum_{i,j=1}^{N} \left(\nabla_j - \frac{1}{k_B T}\nabla_j U(\mathbf{r}^N)\right) \cdot \mathbf{D}_{ij}(\mathbf{r}^N) \cdot \nabla_i\,. \tag{2.19}$$

Using $\rho(q,t)$ and $\rho^*(q,t)$ as u and v, and the Zwanzig-Mori projection operator, one obtains an *exact* equation for $f(q,\tau)$ in the memory-function formalism (see e.g. [28, 29, 30]):

$$\frac{\partial f(q,\tau)}{\partial \tau} = -D_{\text{eff}} q^2 f(q,\tau) + \int_0^\tau f(q,t) M(q,\tau - t) dt, \tag{2.20}$$

where $D_{\text{eff}} = D_0 H(q)/S(q)$ is the effective diffusion constant at wave vector q, and the memory function $M(q,t)$ is given by:

$$M(q,t) = \frac{\left\langle R^*(q) \exp[(1-\mathcal{P})\tilde{\mathcal{O}}t] R(q) \right\rangle}{S(q)}, \tag{2.21}$$

with $R = (1-\mathcal{P})\mathcal{O}\rho(q)$, and the projection operator $\mathcal{P}$ that projects any function g of $\mathbf{r}^N$ onto a spatial Fourier component of the density:

$$\mathcal{P} = \frac{\langle \rho(-q) g \rangle}{N S(q)} \rho(q) . \tag{2.22}$$

Equation 2.20 is an exact equation for $f(q,t)$. However it is formidable to evaluate in general the memory function $M(q,t)$ which is a complicated functional of the DSF $f(q,\tau)$. The MCT approach to solving this equation is to approximate the memory function. This approach involves two approximations. Firstly, it approximates the projection operation $(1-\mathcal{P})$ by a projection onto bilinear products of density. Secondly, it assumes the fluctuation in $\rho(q,t)$ is Gaussian and factorises the four-point correlator: $\langle \rho\rho\rho\rho \rangle = \langle \rho\rho \rangle \langle \rho\rho \rangle$. For more details see e.g. [29]. This approach allows solving Eq. 2.20 knowing only the static structure factor $S(q)$.

Another derivation of MCT started from the Zwanzig-Mori formal results for a full system consisting of colloid and solvent particles, then simplified for a colloids by introducing a noise term while ignoring the momentum term to give [31]:

$$\frac{\partial f(q,\tau)}{\partial \tau} = -D_{\text{eff}} q^2 \left[f(q,\tau) + \int_0^\tau \frac{\partial f(q,t)}{\partial t} m(q,\tau - t) dt \right] , \tag{2.23}$$

where $m(\mathbf{q},t)$ is called the memory kernel, and is approximated as a quadratic functional of $f(q,\tau)$:

$$m(\mathbf{q},t) = \sum_{\mathbf{k}} V_{\mathbf{q},\mathbf{k}} f(\mathbf{k},t) f(\mathbf{k}-\mathbf{q},t) , \tag{2.24}$$

with $V_{\mathbf{q},\mathbf{k}}$ depends only on the structure of the system and can be evaluated from $S(q)$. Therefore Eq. 2.23 can be solved with only the knowledge of $S(q)$ to obtain $f(q,\tau)$ without any adjustable parameter. This approach with Eq. 2.23 and the approximated $m(\mathbf{q},t)$ readily calculated from $S(q)$ is regularly used in the MCT literature for colloidal systems.

The mathematics of MCT seems to obscure the underlying physics. To understand MCT a little more, it is better to consider some strip down versions of MCT where only the physics remains [24, 32]. This approach also starts from the Smoluchowski equation of motion, but with the force term $-\nabla_j U(\mathbf{r}^N)$ derived from the Hamiltonian functional $H\{\rho(\mathbf{r})\}$ as a functional derivative:

$$-\nabla_j U(\mathbf{r}^N) = -\rho(\mathbf{r})\nabla_j \left(\frac{\delta H\{\rho\}}{\delta \rho}\right) . \tag{2.25}$$

The form of H is approximated as harmonic expansion in density fluctuation, which corresponds to the approximation of bilinear product projection of the previous approach:

$$H = -\frac{1}{2}\int \rho(\mathbf{r})\rho(\mathbf{r}')c(|\mathbf{r}-\mathbf{r}'|)d^3\mathbf{r}\, d^3\mathbf{r}' , \tag{2.26}$$

where $c(|\mathbf{r}-\mathbf{r}'|)$ is the direct correlation function and its Fourier transform is connected to the static structure factor as $c(q) = V[1 - S(q)^{-1}]/N$. These give the equation for the density $\rho(\mathbf{r})$:

$$\frac{\partial \rho}{\partial t} = \nabla^2\rho + \nabla\cdot\mathbf{D}\left(\rho\nabla\frac{\delta H}{\delta\rho}\right) . \tag{2.27}$$

The first term gives rise to a pure diffusional solution that is recovered in dilute non-interacting system ($H = 0$). Schematically, the second term describes changes in ρ by a product of $\rho\rho$ (using Eq. 2.26). Similarly, other equations for higher correlation of ρ give a hierarchy of equations for $\langle\rho\rho\rangle$ involving $\langle\rho\rho\rho\rangle$ and $\langle\rho\rho\rho\rangle$ involving $\langle\rho\rho\rho\rho\rangle$. Now the Gaussian approximation is used for the factorisation $\langle\rho\rho\rho\rho\rangle = \langle\rho\rho\rangle\langle\rho\rho\rangle$, which then makes the set of equations of motion closed and solvable.

2.2.3 MCT results

Within the MCT framework, variation in control paramaters of the system, i.e. volume fraction ϕ and interaction potential (shape, range and strength), will change $S(q)$ smoothly. Nevertheless, in certain ranges of the control parameters, the solution of Eq. 2.23 shows 'bifurcation' of different orders identified as glass-transition singularities.

The simplest transition is the fluid-glass transtion found in hard-sphere systems by solving for the long time limit of the DSF, also called the non-ergodicity parameter f_q,

$$f_q = \lim_{\tau \to \infty} f(q, \tau). \tag{2.28}$$

If $f_q = 0$, the system is in an ergodic state, if $f_q > 0$, it is in a glassy state. MCT predicts this transition to occur at a critical volume fraction $\phi_c = 0.52$ [33], which is smaller than the experimental value of $\phi_g = 0.58$ [1, 2]. However, the dynamics near the glass transition predicted by MCT compares well with experiments [5] provided that MCT volume fractions are scaled up by ϕ_g/ϕ_c.

In systems with short-ranged attraction, the solutions of the MCT equations show higher-order singularities and the fluid-glass transition has a re-entrant shape (Fig. 2.2). Re-entrance means the glass that forms at high ϕ in a hard-sphere system melts when enough attraction is added, and freezes again if the attraction is even higher. In the ϕ-U parameter plane (U is the attraction strength), the re-entrant glass transition has a '>' shape [35, 36, 37, 38]. The glass formed at low attraction is arrested due to the caging effect of non-overlapping hard-core neighbouring particles and termed 'repulsive' glass. The glass formed at high attraction in the re-entrance scenario is however arrested by the strong attractive bonds (but still reversible) between neighbouring particles, and is termed 'attractive' glass. For systems with attraction range ξ smaller than a critical ξ_c, the fluid-repulsive glass and fluid-attractive glass transition lines intersect at a crossing point, where the latter continues into the glass region and terminates at an

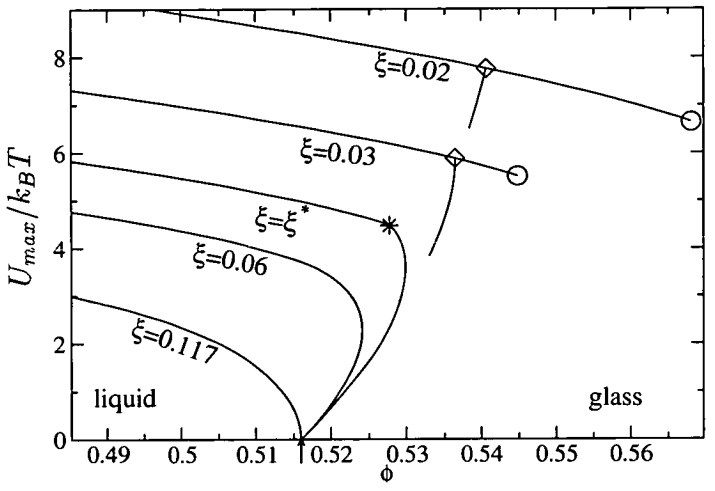

Figure 2.2: Glass transition diagram for the square well attractive system predicted by MCT at different attraction ranges, from [34]. For short-range attractions ($\xi < \xi^*$), the gel and glass lines intersect at a crossing point ($\diamond$) and the gel line terminates at an A3-endpoint singularity ($\circ$), at $\xi = \xi^*$, the gel and glass lines intersect at an A4 singularity ($*$). For larger range $\xi > \xi^*$, the transitions vary smoothly as attraction strength increases.

'A3' singularity. As ξ is increased, the transition line that separate repulsive and attractive glass becomes shorter and finally turns into an 'A4' singularity at the intersection for $\xi = \xi_c$. For $\xi > \xi_c$, MCT does not distinguish the two types of glass anymore. These features seem to be universal to many short-range attractive systems with different attraction potentials, e.g. adhesive hard-spheres [39], Yukawa [39], square-well [36], Asakura-Osawa (AO) [35].

With its detailed predictions of the glass transition and dynamics, MCT is well placed for comparisons with experimental data. However, for systems with attraction, the extra control parameter (attraction strength or temperature) makes it difficult to determine the corresponding state points between theory and experiments. This is particularly the case since MCT underestimates the glass transition volume fraction in hard-spheres. It also seems to underestimate the attraction strength of the attractive glass transition in colloid-polymer mixtures [37]. Despite the difficulties in quantitative verification, MCT agrees well qualitatively with several experiments [37, 40, 41, 42] and computer simulations [37, 43]. However detailed experimental data that can be compared with

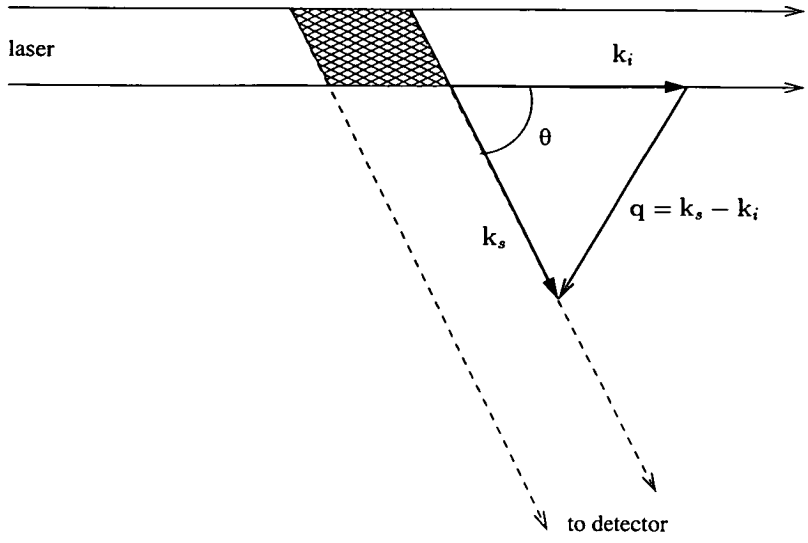

Figure 2.3: Schematic diagram of a simple light scattering setup. A laser beam is shone through the sample at direction $\mathbf{k}_i$. A detector measures the scattered intensity at an angle θ at direction $\mathbf{k}_s$. The intersection of the incident and detection light path defines the scattering volume (shaded region). The difference of scattered and incident wavevectors defines the scattering wavevector $\mathbf{q}$.

MCT do not yet exist for the repulsive-attractive glass system. The main part of this thesis presents and discusses just such data obtained from light scattering.

2.3 Light scattering

This section reviews the key relevant concepts and principles of light scattering that are the basis of experimental measurements of this work. Full details of the theory of light scattering can be found in e.g. [27, 28]. The procedures used to measure $S(q)$ and $f(q,\tau)$ will be presented in chapter 4.

2.3.1 General light scattering

Let us consider a simple light scattering experiment as in Fig. 2.3. A narrow plane-wave, monochromatic beam of light of wavelength λ is shone through a colloidal sus-

pension. The incident wavevector is defined in the direction of the beam with magnitude $|\mathbf{k}_i| = 2\pi n/\lambda$, where n is the refractive index of the suspending medium of the sample (the solvent). A detector is arranged through some optics so that it will detect light in the far field at an angle θ relative to the incident beam in the scattering plane perpendicular to the incident polarization. The detection light path defines the direction of the scattered wavevector $\mathbf{k}_s$. Since the mass of a colloidal particle is much larger than the rest mass of the incident photon, energy transfer in scattering events can be ignored. So we assume the scattering is quasi elastic, thus $|\mathbf{k}_s| = |\mathbf{k}_i|$. The scattering vector of this experiment is defined as $\mathbf{q} = \mathbf{k}_s - \mathbf{k}_i$ and $q = 4\pi n \sin(\theta/2)/\lambda$.

Let us first asumme that the particles scatter weakly enough that only single scattering is considered (corresponding to the first Born approximation). Then the scattering volume — intersection of incident and detection light path — is the only region where detected scattered light originates. The magnitude of the scattered field from a *single* isotropic spherical particle j of radius R is

$$b_j(q) = 4\pi \int_0^R r^2 [n_j(r) - n_0] \frac{\sin(qr)}{qr} dr \ , \tag{2.29}$$

where $n_j(r)$ is the refractive index of particle j at a distance r from its centre and n_0 is the refractive index of the solvent. For monodisperse particles all $b_j(q)$ are the same, $b_j(q) = b(q)$.

The instantaneous scattered field amplitude $E(\mathbf{q}, t)$ from all N identical particles in the scattering volume is

$$E(\mathbf{q}, t) = b(q) \sum_{j=1}^{N} e^{i\mathbf{q}\cdot\mathbf{r}_j(t)} \ , \tag{2.30}$$

where $\mathbf{r}_j(t)$ is the postion of the centre of particle j at time t. Apart from the prefactor $b(q)$, $E(\mathbf{q}, t)$ is the same as the Fourier transform $\rho(\mathbf{q}, t)$ of the position density of the system (c.f. Eq. 2.13). The instantaneous scattered intensity is

$$I(\mathbf{q}, t) = |E(\mathbf{q}, t)|^2 \ . \tag{2.31}$$

The ensemble-averaged intensity $\langle I \rangle$ is defined as the average of $I(\mathbf{q}, t)$ over many different realisations of the system. For isotropic sample, i.e. where the arrangement of particles is independent of direction, the ensemble average can be taken over many scattering vectors $\mathbf{q}$ with the same magnitude. Thus the average intensity can be expressed as a function of q — the magnitude of the scattering vector. In the case of an ergodic sample where particles in the scattering volume can fully explore all possible arrangements, the ensemble average is equivalent to the (long enough) time average. From now on, 'average' means ensemble average unless explicitly stated otherwise.

2.3.2 Static light scattering

The average scattered intensity as a function of scattering wavevector q is given by (Eqs. 2.30 and 2.31):

$$\langle I(q) \rangle = [b(q)]^2 \sum_{j=1}^{N} \sum_{k=1}^{N} \left\langle e^{i\mathbf{q}\cdot(\mathbf{r}_j - \mathbf{r}_k)} \right\rangle \ . \tag{2.32}$$

It can also be written as a product of an intra-particle interference term $P(q)$, and an inter-particle interference term $S(q)$:

$$\langle I(q) \rangle = N[b(0)]^2 P(q) S(q) \ , \tag{2.33}$$

where $P(q)$ is the single particle form factor, essentially the normalized diffraction pattern from the refractive index distribution in single particles:

$$P(q) = \left[\frac{b(q)}{b(0)} \right]^2 , \tag{2.34}$$

and $S(q)$ is the static structure factor:

$$S(q) = \frac{1}{N} \sum_{j=1}^{N} \sum_{k=1}^{N} \left\langle e^{i\mathbf{q}\cdot(\mathbf{r}_j - \mathbf{r}_k)} \right\rangle \ . \tag{2.35}$$

It is the measure the correlation of particle positions, and is effectively the Fourier transform of the pair distribution function $g(r)$ [27]:

$$S(q) = 1 + 4\pi\bar{\rho} \int_0^\infty r^2 [g(r) - 1] \frac{\sin(qr)}{qr} \, dr, \tag{2.36}$$

where $\bar{\rho}$ is the average number density of the sample.

Theoretically, the Ornstein-Zernike equation can be used to formulate an integral equation for $g(r)$ [44]. Some closure approximations are needed to solve for $S(q)$. For hard-spheres, the Percus-Yevick approximation [44] and Verlet-Weis semi-empirical correction [45] provides an analytical expression for the static structure factor that agrees quite well with computer simulation results [28]. In systems of short-range attraction, Percus-Yervick approximation and mean-spherical approximation can be used to obtained $S(q)$ [36, 44, 46, 47]. For colloid-polymer mixtures where the interaction is of AO form, Bergenholtz et.al. [35] used a mapping procedure to an equivalent attractive Yukawa system to calculate $S(q)$ as input to MCT. Their results agree well with simulation except in the low attraction regime (near hard-sphere like). Comparisons between theoretical $S(q)$ and experiments are hindered mainly because experimental $S(q)$ are not accurate for $qR \geq 4$ as $P(q)$ decays very quickly for homogenous spherical particles [28].

Experimentally, the SSF can be obtained from the average intensity if one knows the form factor $P(q)$. The latter in turn can be obtained from the scattered intensity of a dilute sample where the positions of particles are uncorrelated so that its SSF $S_{dil}(q) = 1$. From Eq. 2.33, $S(q)$ of a concentrated sample is obtained from the ratio of scattered intensities of that sample and a dilute one of the same particle, provided the incident intensity is the same (so that $b(0)$ is the same):

$$S(q) = \frac{\langle I(q) \rangle \, N_{dil}}{\langle I_{dil}(q) \rangle \, N} \,, \tag{2.37}$$

where the subsript 'dil' refers to the dilute sample. The ratio of numbers of particles in the same scattering volume can be replaced by the equivalent ratio of volume fractions.

2.3.3 Dynamic light scattering

To measure the dynamics of the system, we need to measure how the particles move in time. Eqs. 2.30 and 2.31 show that as time progresses, the positions of particles change, then the instantaneous scattered field and intensity also change with time. The correlation of the instanstaneous field $E(q,t)$ with itself at a later time $t+\tau$ is a measure of the density time auto-correlation function. Its normalised function is called 'intermediate scattering function':

$$g^{(1)}(q,\tau) = \frac{\langle E(\mathbf{q},0)E^*(\mathbf{q},\tau)\rangle}{\langle I(q)\rangle} \,. \tag{2.38}$$

Knowing that $E(\mathbf{q},t) \propto \rho(\mathbf{q},t)$, Eq. 2.15 shows that $g^{(1)}(q,\tau)$ is the same as the DSF $f(q,\tau)$. Experimentally one measures the scattered intensity $I(\mathbf{q},t)$ and constructs its time correlation function — the intensity correlation function (ICF):

$$g^{(2)}(q,\tau) = \frac{\langle I(\mathbf{q},0)I(\mathbf{q},\tau)\rangle}{\langle I(\mathbf{q})\rangle^2} \,. \tag{2.39}$$

The DSF can be obtained from the ICF and the Siegert relation [28]:

$$g^{(2)}(q,\tau) = 1 + \beta^2 \left[f(q,\tau)\right]^2 , \tag{2.40}$$

where β^2 is the intercept of the correlation function and depends on the specific DLS instrument. Because of the normalization condition $f(q,0) = 1$, the intercept β^2 can be obtained from the ICF: $g^{(2)}(q,0) = 1 + \beta^2$.

It should be noted that the Siegert relation only holds if the scattered field $E(\mathbf{q},t)$ is a zero mean random Gaussian variable [28, 48], i.e. if the averages in Eqs. 2.38 and 2.39 are ensemble averages [49]. Therefore it is essential that the measured ICF is an ensemble-averaged quantity so that Eq. 2.40 can be used to obtain the DSF.

For a fast-relaxing equilibrium sample, any correlation in density fluctuation vanishes after some time τ_r which can be characterized as the relaxation time. So a DLS measurement at the same scattering vector $\mathbf{q}$ will observe many independent realizations

of the system if the measurement time is much longer than τ_r. Then the time-averaged correlation function is the same as the ensemble-averaged one. The correlation function is also independent of starting time. Such systems are called ergodic and have $f(q, \infty) = 0$.

However, in non-equilibrium systems, some components of the density fluctuation do not completely relax, or do so extremely slowly. In these cases, $f(q, \tau)$ is finite for very large τ, and a time-averaged correlation function will not sample all realizations of the system during the measurement time at one $\mathbf{q}$. Ensemble average of isotropic systems can be taken by averaging measurements at different scattering vectors $\mathbf{q}$ of the same magnitude. Experimentally averaging over many different $\mathbf{q}$ is not a trivial task, especially when one wants to obtain dynamical information at large τ at the same time. Many different experimental schemes have been developed for this purpose and each has its own advantages and disadvantages. During the course of this work, a different ensemble averaging scheme was developed and will be discussed in detail in chapter 3.

2.3.4 Light scattering on turbid samples

So far the theory on light scattering has been discussed only under the assumption that the sample is weakly scattering and only single scattering events are significant. However, many colloidal systems are turbid, especially at high concentration. In the case where the sample is significantly turbid but multiple scattering does not overwhelmingly dominates, cross-correlation techniques in some special scattering arrangements [50] can be used to extract the single-scattering static and dynamic information. One of those arrangements is the two-colour light scattering, the detailed descriptions and analysis of which was described in [51] and its modifications used in this work in chapter 4. Here I just summerize relevant results.

Two laser beams of different wavelengths, says blue (λ_B) and green (λ_G) and two

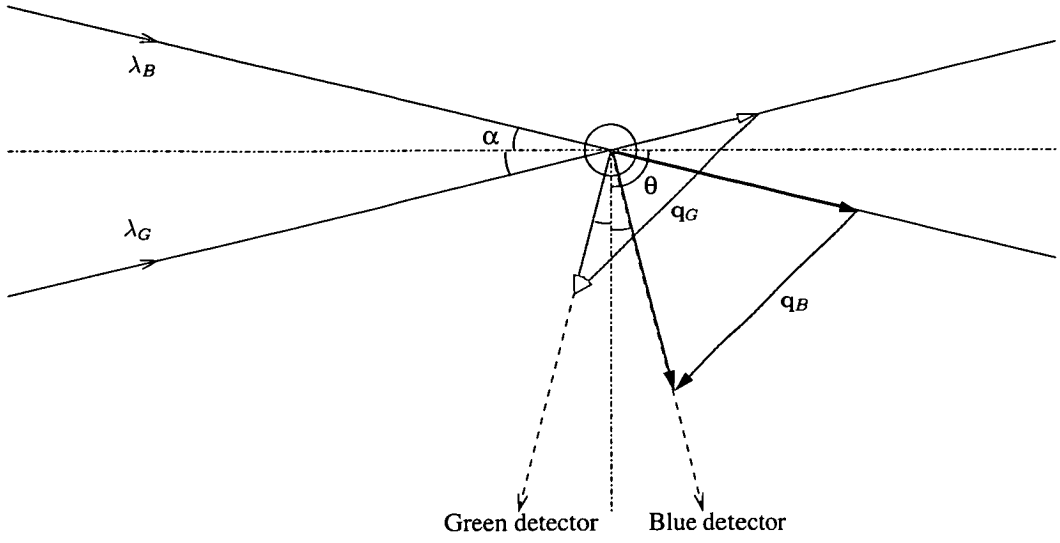

Figure 2.4: Schematic setup of the two-colour light scattering arrangement. The incident and detection paths of the two colours λ_B and λ_G are separated by 2α such that the scattering vectors $\mathbf{q}_B$ and $\mathbf{q}_G$ are identical, both in magnitude and direction. This ensures only single-scattering events on each colour are correlated and contribute to the time-dependence of the cross-correlation function.

detectors with filters are used essentially as two separate scattering experiments simultanuously on the same scattering volume at different scattering angles for each wavelength. The incident and scattered beams are arranged such that the scattering angles θ_B and θ_G are different but the scattering vectors are identical, i.e. $\mathbf{q}_B = \mathbf{q}_G = \mathbf{q}$. This is achieved by separating the incident and detection beams of the two colours by an angle 2α (Fig. 2.4) so that $\theta_G = \theta + 2\alpha$, $\theta_B = \theta - 2\alpha$, and α satisfies

$$\tan\alpha = \frac{\lambda_G - \lambda_B}{\lambda_G + \lambda_B} \tan\left(\frac{\theta}{2}\right). \tag{2.41}$$

The outputs of the two dectectors are cross-correlated to give the intensity correlation function (ICF):

$$g^{(2)}(q,\tau) = \frac{\langle I_B(q,0) I_G(q,\tau)\rangle}{\langle I_B(q)\rangle \langle I_G(q)\rangle}, \tag{2.42}$$

where $\langle I_B\rangle$ and $\langle I_G\rangle$ are the average scattered blue and green intensities respectively.

In this arrangement, it can be shown [51] that only single scattering events in both colour probe exactly the same Fourier component of the density fluctuation and thus

they are correlated. All other, multiply-scattered, light does not probe the same component in both colours and is completely uncorrelated and thus does not contribute to the time-dependence of the cross-correlation function $g^{(2)}(q,\tau)$. The ICF can be expressed [51] in terms of the normalised single scattering dynamic structure factor $f(q,\tau)$ by the Siegert relation (Eq. 2.40):

$$g^{(2)}(q,\tau) = 1 + \beta^2\beta_{MS}^2\left[f(q,\tau)\right]^2, \tag{2.43}$$

where the intercept now is $\beta^2\beta_{MS}^2$. The factor β^2 has the same meaning as before and depends on the ratio of detector area and coherence area for single scattering and also on the overlap of the scattering volumes by each colour. This factor is instrument related and dependent on scattering angle but not on the sample used. The extra factor β_{MS}^2 reflects the amount of singly-scattered intensities, $\langle I_B^S\rangle$ and $\langle I_G^S\rangle$, relative to the total (singly and multiply) scattered intensity:

$$\beta_{MS}^2 = \frac{\langle I_B^S\rangle\langle I_G^S\rangle}{\langle I_B\rangle\langle I_G\rangle}\,. \tag{2.44}$$

Knowing β_{MS}^2 will allow extraction of the singly-scattered intensity $\langle I^S(q)\rangle$ from the total measured intensity. Hence a proper static structure factor can also be obtained from two-colour light scattering for turbid sample [52].

Chapter 3

Echo DLS

3.1 Introduction

The main characteristic of glassy states is their partially frozen dynamics. In fact, the definition of a kinetic glass transition is when the long time limit of the dynamic structure factor becomes positive, $f(q, \infty) > 0$. In these cases, since the density fluctuation at a particular fixed wavevector $\mathbf{q}$ does not fully relax, the time-averaged intensity correlation function (ICF) at that $\mathbf{q}$ explores only a subsection of the configuration phase space and therefore does not measure the true dynamics [49]. Therefore to study dynamics of non-ergodic systems, or those with very slow relaxation, one needs to average over many realizations of the system. This can be achieved by averaging over many scattering vectors $\mathbf{q}$ of the same scattering volume or at the same $\mathbf{q}$ for many scattering volumes.

A good ensemble averaging method is useful not only in study of colloidal glassy dynamics encountered in this work, but also in various other fields [53]. These include aging in many soft systems [54, 55, 56, 57], restructuring of granular materials [58, 59] to list a few. Other scattering techniques like X-ray photon correlation spectroscopy also need ensemble averaging to study the dynamics of this class of materials.

However, practical ensemble averaging is not trivial. Brute-force method of averaging over many measurements at different $\mathbf{q}$ takes a prohibitively long time to complete. For example, a time-averaged measurement of $g^{(2)}(q,\tau)$ of up to a maximum delay time τ_{max} requires measurement time of the order of at least τ_{max}. Many hundred such measurements need to be carried out to obtain a statistically meaningful ensemble average. This pushes the total measurement time to the order of $\sim 1000\tau_{max}$. Therefore to measure dynamics of a non-ergodic sample up to $\tau_{max} = 1000$ s, normal brute-force ensemble averaging method requires $\sim 10^6$ seconds (12 days) of measurement time.

Several other methods have been developed to overcome this difficulty. They however have some limitations on the light scattering arrangements or types of samples that can be used. The Pusey-vanMegen method [49] utilizes the relationship between time- and ensemble-average intensity to obtain the proper dynamics from time-averaged ICF. This method requires that the intercept of the measured ICF in Eq 2.40 be ideal $\beta^2 = 1$. This is a difficult condition in conventional DLS setup and impossible in cross-correlation schemes [50, 51, 60] as the intercept β^2_{MS} is always less than 1 because of multiple scattering. Multiple speckle methods [61, 62, 63] measure time-averaged ICF at many different $\mathbf{q}$ of the same magnitude simultaneously. Since the arrangement of the scattering vectors $\mathbf{q}$ spreads out in space, these methods prevent the use of special arrangements like two-colour or 3-D DLS which require a strict spatial constraint on the incident and scattered beams.

We have developed a new ensemble averaging method that requires simple hardware design, yet is robust and produces good data the quality of which can be monitored. This technique achieves ensemble averaging by rotating the sample continuously so that averaging is done over many different wave-vectors of the same magnitude. Because of the rotation, the correlation function decays quickly. However after the sample completes an exactly whole number of revolutions, it comes back to the same orientation where any de-correlation due to rotation vanishes and correlation due to the dynamics of particles inside the sample recovers, where an 'echo' in the correlation

function is detected, similar to those obtained in shear experiments [64]. The shapes of echoes in the correlation function can be used as a measure of rotation quality and also to correct for effects of imperfect rotation. As will be discussed in section 3.4, the new method has features in common with the interleaved sampling technique [65].

First a simple model of this technique will be analysed in section 3.2, predicting the shape of echoes which is shown to be independent of the dynamics of the sample. Results from simple simulations of the model are also presented, showing very good agreement with theory. A common practical problem, imperfect rotating speed, is also analysed and shown that it can be corrected for using the areas under echoes. Then in section 3.3 I will describe the implementation of the technique and methods of data analysis. Finally, section 3.4 will end this chapter by discussing the advantages and disadvantages of the technique as well as its potential applications.

3.2 Theory

3.2.1 Theoretical model

Instead of rotating the sample in a fixed light scattering setup, let us consider an equivalent set up where the incident beam and detector rotate about a fixed cylindrical scattering volume scattering volume of radius R_v, containing N particles (fig. 3.1). The incident light beam enters the sample at direction $\mathbf{k}_i$ and a detector collects photon counts at direction $\mathbf{k}_s$ in the far field. Both vectors rotate about the z-axis of the sample but are fixed relative to each other so that the scattering vector $\mathbf{q}(t) = \mathbf{k}_s - \mathbf{k}_i$ is constant in magnitude but rotates about the origin with constant angular speed ω.

The scattered field and intensity defined by Eqs. 2.30 and 2.31 at the detector at time t

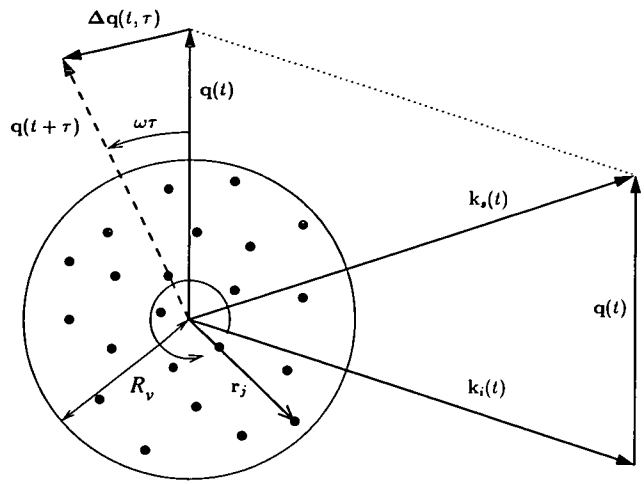

Figure 3.1: A model of N particles in a cylindrical scattering volume of radius R_v. Incident beam (in direction $\mathbf{k}_i$) and detector (in direction $\mathbf{k}_s$) rotates at constant angular speed ω. The scattering wave-vector $\mathbf{q}(t)$ therefore also rotates with time but fixed in magnitude. The difference $\Delta\mathbf{q}$ of scattering vectors at times $t+\tau$ and t rotates in time along with the scattering vector $\mathbf{q}(t)$ and its magnitude depends on τ: $\Delta q = 2q\sin(\omega\tau/2)$.

are functions of t and the (time-dependent) scattering vector $\mathbf{q}(t)$:

$$E(\mathbf{q}(t),t) = b(q)\sum_{j=1}^{N} e^{i\mathbf{q}(t)\cdot\mathbf{r}_j(t)} , \tag{3.1}$$

$$I(\mathbf{q}(t),t) = E(q,t)E^*(q,t) . \tag{3.2}$$

The measured unnormalized field correlation function at delay time τ, averaged over sufficient time, i.e. over many rotations:

$$G^{(1)}(q,\tau) = \langle E[\mathbf{q}(t),t]E^*[\mathbf{q}(t+\tau),t+\tau]\rangle_t \tag{3.3}$$

$$= \sum_{j=1}^{N}\sum_{k=1}^{N}\left\langle e^{i\mathbf{q}(t)\cdot\mathbf{r}_j(t)}e^{-i\mathbf{q}(t+\tau)\cdot\mathbf{r}_k(t+\tau)}\right\rangle_t . \tag{3.4}$$

Since the vectors $\mathbf{q}(t)$ and $\mathbf{q}(t+\tau)$ are rotating many times around the scattering volume, sampling many independent Fourier components, the time averages $\langle\ldots\rangle_t$ in the above equations are equivalent to ensemble averages over many scattering vectors $\mathbf{q}$. The order of this summation is not important, therefore the explicit dependence of $\mathbf{q}$ in time t will be omitted in places for clarity.

One can define a vector $\mathbf{\Delta q}$ as the difference between the scattering vectors at time t and $t+\tau$: $\mathbf{\Delta q}(t,\tau) = \mathbf{q}(t+\tau) - \mathbf{q}(t)$. For a specific value of τ, $\mathbf{\Delta q}$ is fixed in magnitude and rotating in time with angular speed ω (fig 3.1). The correlation function in Eq. 3.4 now becomes:

$$G^{(1)}(q,\tau) = \sum_j \sum_k \left\langle e^{i\mathbf{q}\cdot[\mathbf{r}_j(t)-\mathbf{r}_k(t+\tau)]} e^{-i\mathbf{\Delta q}(\tau)\cdot\mathbf{r}_k(t+\tau)} \right\rangle . \tag{3.5}$$

For values of τ that are exact multiples of the period of rotation, $\tau = nT$, $n = 0, 1, 2, \ldots$ the scattering vectors $\mathbf{q}(t)$ and $\mathbf{q}(t+\tau)$ are exactly the same, therefore $\mathbf{\Delta q}(nT) = 0$. Then the second exponential in Eq. 3.5 is simply one. The correlation function at these values is exactly the same as an ensemble average over all $\mathbf{q}(t)$ of the dynamic structure factor:

$$G^{(1)}(q,\tau = nT) = \sum_j \sum_k \left\langle e^{i\mathbf{q}\cdot[\mathbf{r}_j(t)-\mathbf{r}_k(t+\tau)]} \right\rangle . \tag{3.6}$$

For τ away from but close to nT, i.e. $\sin(\pi\tau/T) \ll 1$ so that Δq is small, the factor $\exp(-i\mathbf{\Delta q}(\tau)\cdot\mathbf{r}_k(t+\tau))$ is less than one. It reduces $G^{(1)}(q,\tau)$ from the value it would have if there were no rotation. In other words, the exponent in equation (3.5) that contains Δq gives rise to a decay in $G^{(1)}(q,\tau)$ due to rotation of the sample. For τ far enough from nT, i.e. $\sin(\pi\tau/T) \sim 1$, the fields at $\mathbf{q}(t)$ and $\mathbf{q}(t+\tau)$ are independent of each other, therefore Eq. 3.4 is a product of 2 field averages so equal to zero.

Ideally, equation (3.5) allows us to measure the ensemble-averaged correlation function at delay times equal to multiples of rotation period ($\tau = nT$) without the need to know the effect of rotation on the functional form of $G^{(1)}(q,\tau)$. However, it will be clear in section 3.2.3 that this knowledge is essential for further understanding of the technique and more importantly for correcting imperfection of the rotation in experimental conditions.

We can split the sum in equation (3.5) into 2 terms: one with $j = k$ and one with

$j \neq k$:

$$G^{(1)}(q,\tau) = \sum_k \left\langle e^{i\mathbf{q}\cdot[\mathbf{r}_k(t)-\mathbf{r}_k(t+\tau)]} e^{-i\Delta\mathbf{q}\cdot\mathbf{r}_k(t+\tau)} \right\rangle + \sum_k \sum_{j\neq k} \left\langle e^{i\mathbf{q}\cdot[\mathbf{r}_j(t)-\mathbf{r}_k(t+\tau)]} e^{-i\Delta\mathbf{q}\cdot\mathbf{r}_k(t+\tau)} \right\rangle \tag{3.7}$$

$$= \sum_k \left\langle e^{i\mathbf{q}\cdot[\mathbf{r}_k(t)-\mathbf{r}_k(t+\tau)]} e^{-i\Delta\mathbf{q}\cdot\mathbf{r}_k(t+\tau)} \right\rangle + \sum_k \sum_{j\neq k} \left\langle e^{i\mathbf{q}(t)\cdot\mathbf{r}_j(t)} e^{-i\mathbf{q}(t+\tau)\cdot\mathbf{r}_k(t+\tau)} \right\rangle . \tag{3.8}$$

Let us consider first the case of dilute non-interacting particles, where positions of different particles are uncorrelated. Thus the 2 phase factors in the second sum are independent and can be separated into 2 averages, each of which is an average of random phase factor thus equals to zero. Therefore only the first sum remains in the correlation function:

$$G^{(1)}(q,\tau) = \left\langle \sum_k e^{i\mathbf{q}\cdot[\mathbf{r}_k(t)-\mathbf{r}_k(t+\tau)]} e^{-i\Delta\mathbf{q}\cdot\mathbf{r}_k(t+\tau)} \right\rangle . \tag{3.9}$$

On changing the index k, any changes in the first phase factor $\exp(i\mathbf{q}\cdot[\mathbf{r}_k(t)-\mathbf{r}_k(t+\tau)])$ depend only on the intrinsic motion of particle k, while changes in the second phase factor $\exp(-i\Delta\mathbf{q}\cdot\mathbf{r}_k(t+\tau))$ depend only on the position of particle k. If it is assumed that there is no centrifuging and external field, then the motion of any particle does not depend on its position. These two phase factors thus change independently with respect to k. The sum can then be separated:

$$G^{(1)}(q,\tau) = \frac{1}{N} \left\langle \sum_k e^{i\mathbf{q}\cdot[\mathbf{r}_k(t)-\mathbf{r}_k(t+\tau)]} \sum_l e^{-i\Delta\mathbf{q}\cdot\mathbf{r}_l(t+\tau)} \right\rangle . \tag{3.10}$$

By the same argument, the motions of particles at length scale $1/q$ (the first sum) do not depend on the distribution of their positions over length scale $1/\Delta q$ (comparable to the scattering volume size) on going from one scattering vector $\mathbf{q}$ to the next. The assumption here is that $\Delta q \ll q$, i.e. τ is close to nT. Note that the second sum

depends on the distribution of particle positions and not the structure of the sample as the first. Therefore the ensemble sum can also be separated:

$$G^{(1)}(q,\tau) = \frac{1}{N}\left\langle \sum_k e^{i\mathbf{q}\cdot[\mathbf{r}_k(t)-\mathbf{r}_k(t+\tau)]} \right\rangle \left\langle \sum_l e^{-i\Delta\mathbf{q}\cdot\mathbf{r}_l(t+\tau)} \right\rangle \tag{3.11}$$

$$= \frac{1}{N}\sum_k \left\langle e^{i\mathbf{q}\cdot[\mathbf{r}_k(t)-\mathbf{r}_k(t+\tau)]} \right\rangle \sum_l \left\langle e^{-i\Delta\mathbf{q}\cdot\mathbf{r}_l(t+\tau)} \right\rangle . \tag{3.12}$$

This indicates the separation in the correlation function between sample dynamics and rotation of the sample. The calculation so far assumes independent particle positions. However, for strongly interacting systems where particle positions are correlated, the same result still holds. This can be proved by replacing independent particles in the above calculation by small regions of the sample between which there is no correlation in configuration. Then the scattered phase factor from different regions are independent and can be separated. It must be assumed that these 'correlated' regions are very small compared to the scattering volume. This assumption is already implicit in the derivation of the Siegert relation (Eq. 2.40) for concentrated systems [28, 48].

It is shown above that the correlation function (Eq. 3.5) can be factorized into 2 terms (Eq. 3.12): one depends on the dynamics of the sample we want to probe, the other depends only on the rotation of the sample with three assumptions. These are (i) the rotation is slow so that there is no centrifuging and there is no radial external field acting on the particles. (ii) The regions in which particle positions are correlated are very small compared to the scattering volume. (iii) The separation is valid only for τ close to nT, i.e. $\sin(\pi\tau/T) \ll 1$.

From Eq. 3.12, the normalized field correlation function is:

$$g^{(1)}(q,\tau) = \frac{\left\langle \sum_{j,k} e^{i\mathbf{q}\cdot[\mathbf{r}_j(t)-\mathbf{r}_k(t+\tau)]} \right\rangle}{\left\langle \sum_{m,n} e^{i\mathbf{q}\cdot[\mathbf{r}_m(t)-\mathbf{r}_n(t)]} \right\rangle} \times \frac{\left\langle \sum_l e^{-i\Delta\mathbf{q}\cdot\mathbf{r}_l(t+\tau)} \right\rangle}{N} \tag{3.13}$$

$$g^{(1)}(q,\tau) = f(q,\tau) \times g_\tau^{(1)}(q,\tau) , \tag{3.14}$$

where the first term is the ensemble averaged dynamic structure factor (DSF) as if the sample were not rotating, $f(q,\tau)$. This measures the dynamics of the sample at wave-vector q and is the quantity of interest. The second term, $g_r^{(1)}(q,\tau)$, reflects the rotation of the sample. Averaged over many speckles with the assumption that the size of the scattering volume is much larger than any correlation length in particle positions of a homogeneous sample, this term can be rewritten as an integral with a uniform distribution $P(\mathbf{r})$ of particle position $\mathbf{r}$:

$$g_r^{(1)}(q,\tau) = \frac{1}{N}\left\langle \sum_l e^{-i\mathbf{\Delta q}\cdot\mathbf{r}_l(t+\tau)} \right\rangle = \int e^{-i\mathbf{\Delta q}\cdot\mathbf{r}} P(\mathbf{r})d\mathbf{r}\,, \tag{3.15}$$

where the integral is evaluated over the scattering volume. Since $\mathbf{r}$ is uniformly distributed in a circle of radius R_v, the probability distribution function can be written in terms of a radial and an angular component:

$$P(\mathbf{r}) = P(r)P(\phi) = \frac{1}{2\pi}\frac{2r}{R_v^2}\,. \tag{3.16}$$

The scalar product of $\mathbf{\Delta q}$ and $\mathbf{r}$ in the same polar coordinates: $\mathbf{\Delta q}\cdot\mathbf{r} = \Delta q r\cos\phi$. So,

$$g_r^{(1)}(q,\tau) = \int_{r=0}^{R_v}\int_{\phi=-\pi/2}^{3\pi/2} e^{-i\Delta q r\cos\phi}\frac{r}{\pi R_v^2}drd\phi \tag{3.17}$$

$$= \frac{1}{\pi R_v^2}\int_{r=0}^{R_v}\int_{\phi=-\pi/2}^{3\pi/2} re^{-i\Delta q r\cos\phi}drd\phi \tag{3.18}$$

$$= \frac{1}{\pi R_v^2}\int_{r=0}^{R_v}\int_{\phi=-\pi/2}^{\pi/2} r\left(e^{-i\Delta q r\cos\phi} + e^{+i\Delta q r\cos\phi}\right)drd\phi \tag{3.19}$$

$$= \frac{4}{\pi R_v^2}\int_{r=0}^{R_v}\int_{\phi=0}^{\pi/2} r\cos(\Delta q r\cos\phi)drd\phi \tag{3.20}$$

Evaluating this integral with Maple gives:

$$g_r^{(1)}(q,\tau) = \frac{2J_1(\Delta q R_v)}{\Delta q R_v}, \tag{3.21}$$

where $\Delta q = 2q\sin(\omega\tau/2)$ and $J_1(x)$ is a first order Bessel function of the first kind, so that $\frac{2J_1(x)}{x} = \sum_{k=0}^{\infty}\frac{(-1)^k}{k!(k+1)!}\left(\frac{x}{2}\right)^{2k}$.

Let us make a change of variables to more intuitive quantities. Put $u = qR_v$, which represents the dimensionless wave-vector of the light scattering experiment with the size of the scattering volume set as the length scale; and $\vartheta = 2\sin(\omega\tau/2)$, which is a measure of the angle rotated by the sample after a delay time τ. Then $\Delta qR_v = 2qR_v\sin(\omega\tau/2) = u\vartheta$. The expression for the rotational correlation in Eq. 3.14 becomes:

$$g_r^{(1)}(q,\tau) = \frac{2J_1(u\vartheta)}{u\vartheta} \ . \tag{3.22}$$

One can recognize that this expression has the form of the Airy function of the diffracted field from a circular opening in diffraction optics. However here the main variable ϑ is the (measure of) rotating angle rather than wave vector since we look at correlation of field at one specific wave-vector while rotating the diffracting object.

It should be noted that in real equipment the precise functional form of $g_r^{(1)}$ depends on the geometry of the scattering volume which is essentially determined by the profile of the incident and scattered beams. Nevertheless, the separation of sample dynamics and rotation in Eq. 3.14 still holds as it makes no assumption on scattering volume geometry.

The Siegert relation (equation 2.40) and the factorization of the correlation function (equation 3.14) give the experimentally-observed ICF:

$$g^{(2)}(q,\tau) = 1 + \beta^2\left[f(q,\tau)\right]^2\left[g_r^{(1)}(q,\tau)\right]^2 \ . \tag{3.23}$$

Let us look at some properties of the rotational factor $\left[g_r^{(1)}(q,\tau)\right]^2 = (2J_1(u\vartheta)/(u\vartheta))^2$ via the ICF of a rotating rigid sample whose $f(q,\tau) = 1$ for all τ. The corresponding ICF is

$$g^{(2)}_{\text{rigid}}(q,\tau) = 1 + \left(\frac{2J_1(u\vartheta)}{u\vartheta}\right)^2 \ . \tag{3.24}$$

Since this is a function of $\vartheta^2 \propto \sin^2(\omega\tau/2)$, it is a periodic function with period $\omega\tau = 2\pi$ and has main maxima of 2 at $\tau = nT$, which correspond to exact n complete

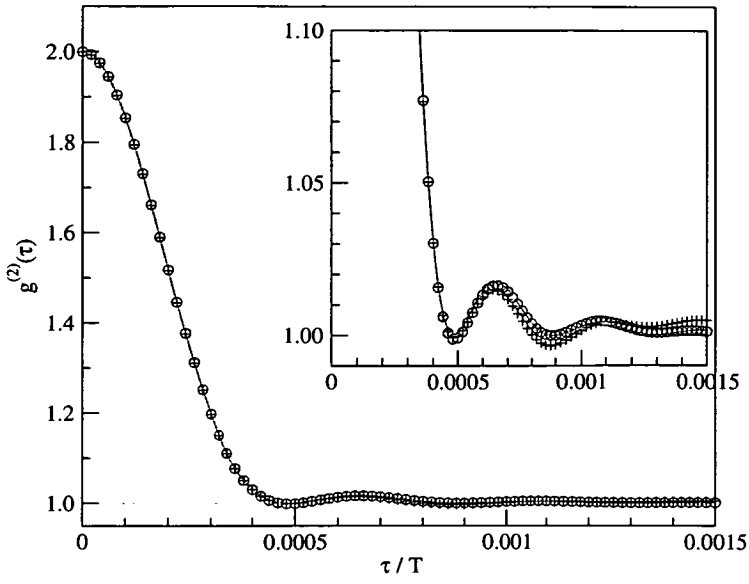

Figure 3.2: Intensity correlation function of the model with $u = 400\pi$. The line was calculated from theory by equation 3.24. The points are results from a simulation of a rigid (crosses) and a fluid (circles) sample. The inset with enlarged vertical axis shows subsequent minima in the pattern.

revolutions of the sample with period T. Away from the maxima, the function decays very quickly to a series of decaying local maxima very close to zero. Figure 3.2 shows a plot of $g_r^{(2)}(q,\tau)$ at the main peak near $\tau = 0$. Figure 3.3 compares the theoretical form to an experimental zero-th peak obtained from an experiment described in figure 3.14.

For typical DLS arrangements with $q \sim 10\mu m^{-1}$ and $R_v \sim 100\mu m$, i.e. $u \sim 1000$, the width of the main peak is of the order of a thousandth of the period, which corresponds to $\omega\tau \sim 2\pi/1000 \ll 1$. Therefore the approximations that lead to the separation of particle dynamics and rotation components in equation (3.14) still hold for values of τ within and even well beyond the main peak.

The decay of the ICF at $\tau = 0$ can be explained with the following physical picture. When the sample is rotated, a random speckle pattern is moving across the detector. The intensity measured at the detector thus fluctuates. Each speckle in that pattern has

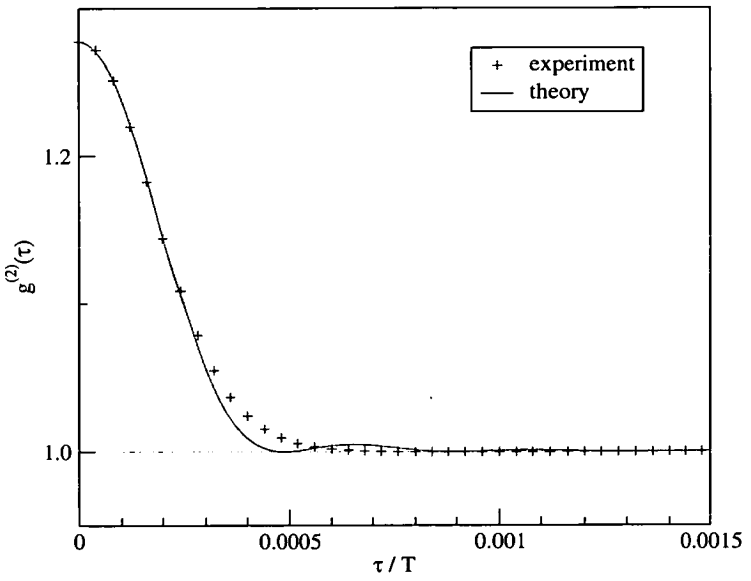

Figure 3.3: Intensity correlation function decays quickly due to rotation of sample, obtained from an echo DLS experiment (crosses). The higher part of the peak agrees well with the theoretical form (continuous line) with intercept of $\beta^2 = 0.277$ and $u = 1250$. The discrepancy near the base line could be due to slight smearing and different scattering volume geometry. The full data for this sample is shown in figure 3.14.

a certain size and intensity both of which vary randomly from one speckle to the next, hence the decay from the maximum at $\tau = 0$. The width of this peak is a measure of the angular size of the speckles, which relates to the size of the scattering volume R_v and the magnitude of the scattering vector q.

The interesting phenomenon is when the sample completes an exact number of revolutions. At this point the positions of all particles in a rigid sample come back exactly as at time $t = 0$, thus the intensity pattern of the speckles repeats. This corresponds to other complete correlations, hence maxima in $g^{(2)}$ at $\omega\tau = 2n\pi$ or $\tau = nT$. For a non-rigid sample, any changes in particle positions after n complete revolutions of the sample are simply due to intrinsic fluctuation of particles but not due to the rotation of the sample. Therefore there is a peak in the correlation signal after exactly every round trip of the sample, and the main peaks in the ICF are called 'echoes'.

3.2.2 Computer simulation

I also did two computer simulations of 10^4 non-interacting point-like particles, one with a rigid sample, the other with a dilute fluid sample. All particles resided in a cube of side $2R_v$ with periodic boundary conditions. Only particles inside the inner cylinder with its axis along z and radius R_v were used in the light scattering calculations to ensure directional invariance in the scattering plane while the scattering vector rotated.

Scattering parameters were chosen to be similar to real experimental DLS conditions. The scattering vector $\mathbf{q}$ with constant magnitude $q = 400\pi/R_v$ was rotated in the x-y plane about the z-axis with period T in time steps $s = T/50000$. Every time step, the scattered intensity was calculated with equation 3.2, and for the fluid sample each particle was moved one step in a 3-D random walk with step length $b = 3.2 \times 10^{-6} R_v$ to simulate Brownian motion. The normalized auto correlation function of the series of intensities obtained was calculated. Several tens of correlation functions of different initial configurations were averaged to reduce the random noise in the average intensity. The ICFs obtained were then compared to theoretical prediction (fig. 3.2).

The size of the step length b controlled how quickly the dynamics of the sample decays. For a 3-D random walk Brownian motion, the mean square displacement of particles after time τ is $\langle \Delta r^2 \rangle = b^2\tau/s$, so that the expected intensity correlation function is [27]:

$$g^{(2)}(q,\tau) = 1 + \exp\left(-\frac{b^2 q^2 \tau}{3s}\right) . \tag{3.25}$$

The peaks of all echoes obtained in the fluid simulation follow the expected dynamics described in Eq. 3.25 extremely well (Fig. 3.4). Fig. 3.2 shows a comparison between the theoretical form of the echo (Eq. 3.24) and results from computer simulation for a rigid and a fluid sample. It shows a remarkable agreement up to the second maximum away from the main peak. Fig. 3.5 shows the 1st, 2nd, 7th and 10th echoes from the dynamics of the simulated fluid sample. The correlation function from the rigid

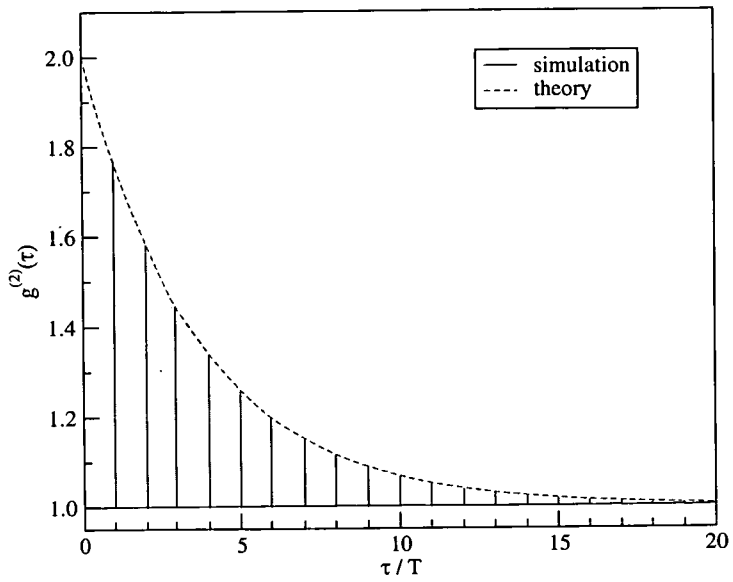

Figure 3.4: Intensity correlation function of the simulated echo DLS of a fluid (continuous line) and the predicted dynamics from its Brownian motion (dashed line) showing that the peaks of the echoes follow the dynamics of the sample.

sample was scaled so that the maxima of the peaks from 2 samples are the same. The factor used in the normalization is the actual particle dynamics since $\Delta q = 0$ at $\tau = T, 2T, 7T, 10T$. The good agreement in shape of the echoes from the fluid sample and the scaled correlation due to rotation verifies that the dynamics of particles does not affect the shape of the echo and can be separated as in Eq. 3.14.

3.2.3 Imperfect rotation

One important assumption of the theoretical treatment above is that the angular speed of the rotation remains strictly constant during the experiment. This requires an absolutely smooth and stable rotation, which in practice is rather difficult to achieve.

The ideal functional form of the echo peaks worked out above assumes the scattered intensity measured at time t is the ideal intensity I_{id} at the angular position $\phi = \omega_0 t$.

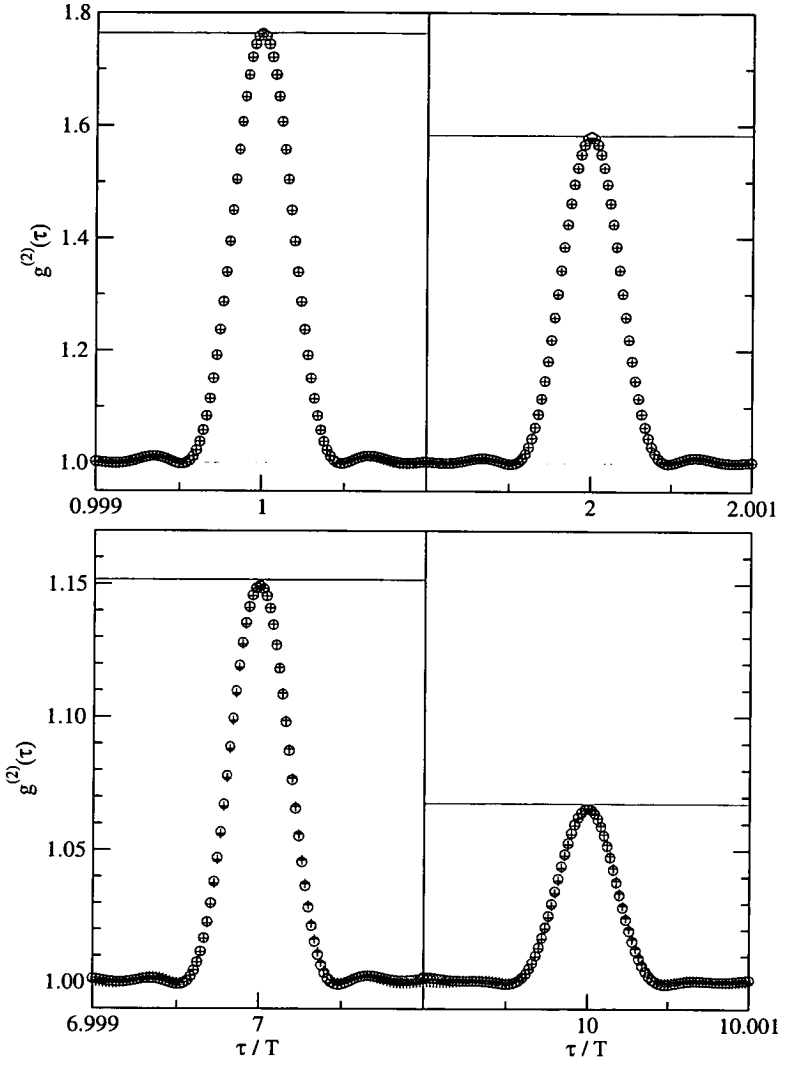

Figure 3.5: Different echo peaks from simulation of a fluid (circles) and a rigid (crosses) sample with $u = 400\pi$. The correlation function of the rigid sample was normalized to the maxima of the fluid peaks. The good agreement of the shape of the peaks shows that the particle dynamics does not affect the correlation due to rotation as in equation (3.14). The continuous line is the expected exponential decay from the Brownian motion of particles in the simulation, which hardly decays at all over the narrow range of each peak.

The ideal ICF obtained from an experiment of duration $\mathcal{T}$ is:

$$g_{id}^{(2)}(\tau) = \frac{1}{\langle I \rangle^2 \mathcal{T}} \int_0^{\mathcal{T}} I_{id}(t) I_{id}(t+\tau) dt \ . \tag{3.26}$$

However, for a realistic rotation, the angular speed is not constant but varies with time: $\omega(t) = \omega_0 + \delta_\omega(t)$, where $\delta_\omega(t)$ is the limited fluctuation of ω. As a result, the intensity measured at time t is now not the same as in the ideal case but the same as the ideal intensity at a shifted time t': $I(t) = I_{id}(t')$ (Fig. 3.6(a)). Therefore a particular pair of intensities measured τ apart appears to be those of the ideal case but with slightly different delay time $\tau - \delta$:

$$I(t)I(t+\tau) = I_{id}(t')I_{id}(t'+\tau-\delta(t,\tau)), \tag{3.27}$$

where δ is a limited function of initial time t and delay time τ (Fig. 3.6(b)). If the fluctuation in angular speed is limited about a fixed mean, it is possible to assume that δ fluctuates about zero in time within a small range $\delta_{\max}$. It is also reasonable to assume that such fluctuation in speed is slow, i.e. its time scale is much longer than the time scale of one speckle passing the detector (typically less than $10^{-3}T$). Therefore, for τ less than this limit, i.e. for τ within the main peak of the zeroth echo, $\delta_{\max}$ is very small (fig. 3.6(c)). In fact, $\delta(t, \tau = 0) = 0$ exactly for all t. This means the shape and size of the zeroth echo is not affected significantly by any limited fluctuation in angular speed, i.e. $g^{(2)}(\tau \sim 0) = g_{id}^{(2)}(\tau)$.

For $\tau \geq T$, δ can be significant. From Eq. 3.27, the ICF taken over a long time $\mathcal{T} \gg T$:

$$g^{(2)}(\tau) = \frac{1}{\langle I \rangle^2 \mathcal{T}} \int_0^{\mathcal{T}} I(t) I(t+\tau) dt \tag{3.28}$$

$$= \frac{1}{\langle I \rangle^2 \mathcal{T}} \int_0^{\mathcal{T}} I_{id}(t') I_{id}(t'+\tau-\delta(t,\tau)) dt' \ . \tag{3.29}$$

The integral in Eq. 3.29 can be split into many integrals over sub-domains Γ_n, each of which comprises many small intervals in t such that $\delta(\tau, t)$ in each domain has

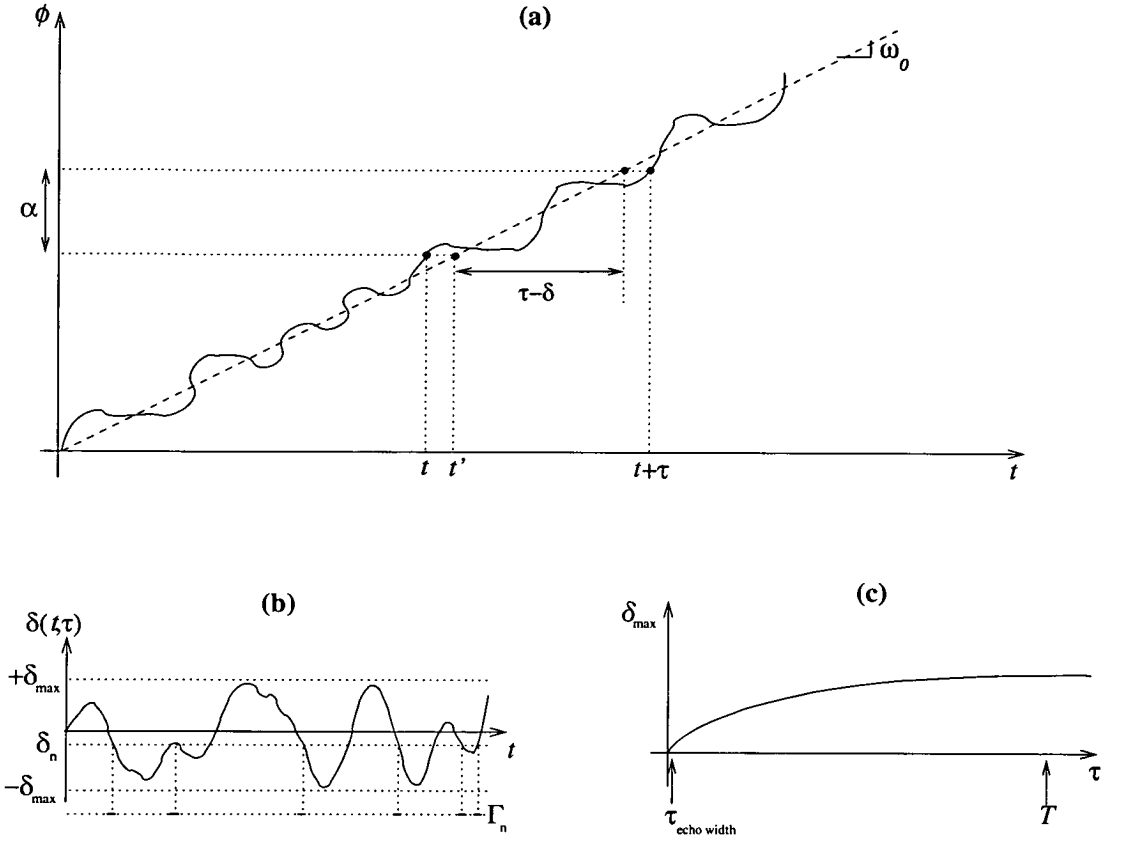

Figure 3.6: Sketches of quantities involved in imperfect rotations of a sample. (a) As the angular speed fluctuates, the angular position of the sample, or equivalently scattered intensity measured, at time t is the same as that in the ideal case but shifted to t', so that ideal delay time τ is effectively shifted by a random limited amount δ. (b) The random shift δ in delay time for a particular τ also fluctuates with initial time t. The collection of time intervals when $\delta(t,\tau) = \delta_n$ constitute the domain Γ_n. (c) The maximum amplitude of fluctuation δ increases with delay time τ from zero to a limiting value. It is assumed that the time scale of this increase is much larger than echo width but smaller than period of rotation.

approximately the same value δ_n (Fig. 3.6(b)):

$$g^{(2)}(\tau) = \frac{1}{\langle I \rangle^2 \mathcal{T}} \sum_n \left[\int_{\Gamma_n} I_{id}(t') I_{id}(t' + \tau - \delta_n) dt' \right] . \tag{3.30}$$

Provided that the total measurement time $\mathcal{T}$ is long enough, each domain Γ_n contains intensities from many speckles, thus the integral over Γ_n represents an ensemble average. Then by comparing to equation 3.26, it is recognized that the integral inside the sum is proportional to the ideal ICF with τ shifted by δ_n. Thus Eq. 3.30 can be re-written as:

$$g^{(2)}(\tau) = \sum_n \frac{\gamma_n}{\mathcal{T}} g^{(2)}_{id}(\tau - \delta_n) , \tag{3.31}$$

where γ_n is the total length of domain Γ_n. Thus the factor $\gamma_n/\mathcal{T}$ is essentially the probability of finding $\delta(t, \tau)$ having a value δ_n. Therefore, Eq. 3.31 in the continuous limit $\gamma_n \to 0$ is in fact a convolution of the ideal correlation function $g^{(2)}_{id}(\tau)$ with the probability distribution $\gamma(\delta)$ of δ:

$$g^{(2)}(\tau) = \int g^{(2)}_{id}(\tau - \delta) \gamma(\delta) d\delta . \tag{3.32}$$

The effect of this 'smearing' of the correlation function means the apparent maximum of the main peak will drop and the width increases. However, it can be shown that the area under $g^{(2)}(\tau)$ is the same as that under $g^{(2)}_{id}(\tau)$. Let us define the *area under the echo* A as the area between the echo peak and the baseline $g^{(2)}(\tau) = 1$ in the vincinity of the echo peak (Fig. 3.7):

$$A = \int_\Omega [g^{(2)}(\tau) - 1] d\tau \tag{3.33}$$

$$= -\Omega + \int_\Omega g^{(2)}(\tau) d\tau , \tag{3.34}$$

where Ω is the integration interval around the echo peak and is large enough that the value of $[g^{(2)}_{id}(\tau) - 1]$ is zero at the limits even if it is shifted by $\pm\delta_{\max}$. Rewriting

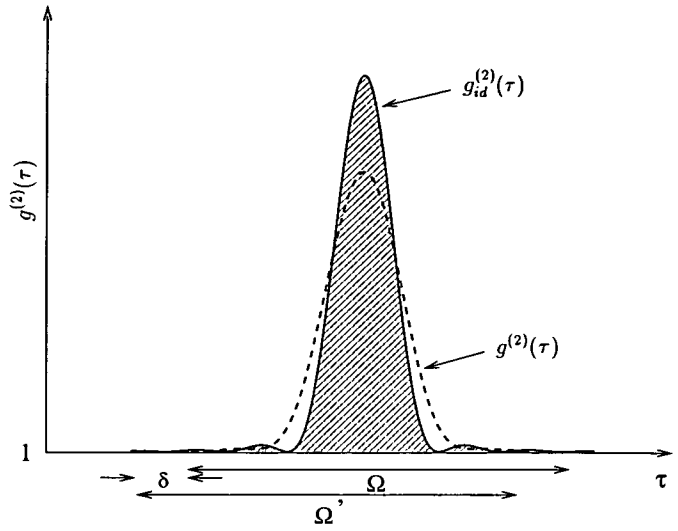

Figure 3.7: Area under an ideal echo peak (continuous line) is unchanged if the integration interval Ω shifts a small amount δ. The effect of 'smearing' is that the measured $g^{(2)}(\tau)$ (dashed line) has a lower peak and increased width but the area is the same as that of the ideal peak.

$g^{(2)}(\tau)$ in terms of the convolution of the ideal ICF (Eq. 3.32), one obtains a double integral

$$A = -\Omega + \int_{\Omega} d\tau \int_{-\delta_{\max}}^{+\delta_{\max}} d\delta \; g_{id}^{(2)}(\tau - \delta)\gamma(\delta) \; . \tag{3.35}$$

A change of variable $v = \tau - \delta$ gives:

$$A = -\Omega + \int_{\Omega'} g_{id}^{(2)}(v)dv \int_{-\delta_{\max}}^{+\delta_{\max}} \gamma(\delta)d\delta \; . \tag{3.36}$$

Since $g_{id}^{(2)}(\tau)$ approaches a constant of 1 for τ at the limits of Ω, the new limits of Ω' do not affect the first integral, thus it can be separated from the second. The second integral is unity since $\gamma(\delta)$ is a normalized probability distribution function. Thus the area under the real echo peak A is the same as that under the ideal echo, independent of any smearing effects.

$$A = -\Omega + \int_{\Omega} g_{id}^{(2)}(v)dv = A_{id} \; . \tag{3.37}$$

It has been shown in section 3.2.1 that the measured correlation function can be factorized into the particle dynamics and the rotation correlation, so that Eqs. 2.40 and 3.14

give:

$$g_{id}^{(2)}(\tau) - 1 = \beta^2[f(q,\tau)]^2[g_r^{(1)}(\tau)]^2, \tag{3.38}$$

where β^2 is the usual intercept in the Siegert relation.

Combining Eqs. 3.33, 3.37 and 3.38, the area under the n-th echo measures the dynamics free of interference from the smearing effect of imperfect rotation:

$$A_n = A_{n,id} = \int_{\tau\sim\tau_n} \beta^2[f(q,\tau)]^2[g_r^{(1)}(\tau)]^2. \tag{3.39}$$

Since the particle dynamics $f(q,\tau)$ is much slower than the time scale it takes for the rotation to sample one speckle ($\sim 10^{-3}T$), $f(q,\tau)$ is constant in the range of the echo width, $f(q,\tau) = f(q,\tau_n)$ where τ_n is the position of the n-th echo maximum. Thus $[f(q,\tau)]^2$ can be taken out of the integral:

$$A_n = [f(q,\tau_n)]^2 \underbrace{\int \beta^2[g_r^{(1)}(\tau)]^2}_{A_0}, \tag{3.40}$$

where the remaining integral is in fact the area under the zero-th echo. Therefore the real dynamics simply scales the area under an echo by a factor of $[f(q,\tau_n)]^2$ relative to the zero-th echo.

3.3 Implementation

In this section I will describe the implementation of experimental arrangements and data analysis for this technique. The DLS setup employed here is two-colour DLS [51] to extract single scattering information from turbid samples. However, if conventional DLS were used, all following details still hold with a replacement of the two colour intensities by the same single colour intensity.

3.3.1 Instrument setup and data acquisition

The construction of the sample holder was very important to obtain a smooth rotation of the sample (Fig. 3.8). Samples were put in cylindrical glass cells with outer diameter $\approx$ 7mm. The sample cell was fixed into a brass inner sample holder by centering screws on top and bottom. The inner holder rotated with very little friction inside a nicely fit Teflon outer holder. The inner holder was driven by a DC servo motor (Faulhaber DC-Minimotor 2444S with encoder feedback, best resolution at $\pm 0.18°$/rev) via 2 perpendicular pairs of pins, one pair on the holder and the other fixed to the motor (Fig. 3.8). This 'pin-driving' mechanism decoupled any wobbling between the motor and the sample, making it unnecessary to line up the motor axis exactly to the optical axis of the DLS setup. The construction of the sample holder alone could ensure the sample was at the centre of the setup, which needed to be checked only once.

Scattered light in the far field was detected by photo-multiplier tubes, and scattered intensity $I(t)$ as a function of time t was measured by counting the number of photon pulses produced by the detector in consecutive time intervals $[t, t+s]$, where the length of this interval s, called *sample time*, can be set prior to the experiment. Therefore intensities were realized as discrete numbers of photon counts in discrete unit of sample time s, which is typically a few tens of microseconds. The cross correlation function of the blue intensity - $I_B(t)$, and green - $I_G(t)$, was constructed as:

$$g^{(2)}(k) = \frac{N \sum_{j=1}^{N} I_B(j) I_G(j+k)}{\left(\sum_{j=1}^{N} I_B(j)\right)\left(\sum_{j=1}^{N} I_G(j+k)\right)}, \tag{3.41}$$

where $g^{(2)}(k)$, $I(j)$ are the correlation function and photon counts at delay time $\tau = ks$ and at time $t = js$, respectively. This formulation of the correlation function where the normalizing intensity is the product of the average of direct intensity $I(j)$ and that of delayed intensity $I(j+k)$ is the *symmetric normalization* scheme which improves the accuracy of the result if the input intensity is varied slowly [66].

Since the echo technique requires correlating the intensity at one speckle with that at

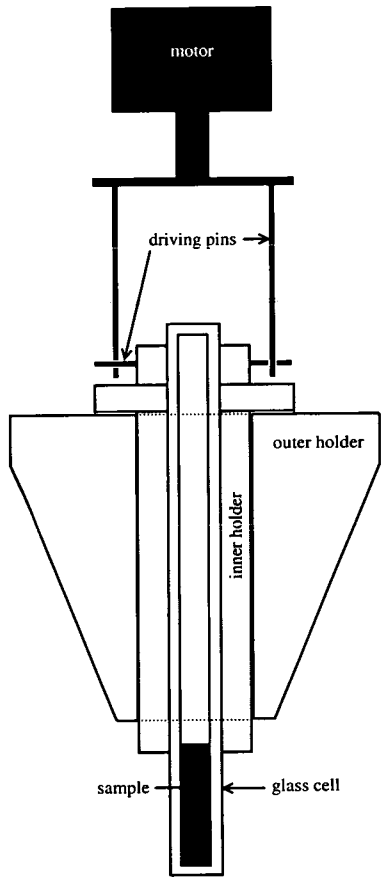

Figure 3.8: Schematic diagram of the sample holder construction. The inner and outer holders are made so that the inner one can rotate smoothly. The sample is driven by a DC servo motor via 2 pairs of pins.

exactly the same place after some delay time τ , it is necessary that a linear sampling scheme is used. This means the sample time s has to be constant for all delay times τ. In order to calculate the correlation function for a large delay time τ of say 1000s, a very large number of samples ($\tau/s \approx 10^8$) have to be stored in a buffer. The constraint of storing large number of samples makes the use of a software correlator more effective and inexpensive, especially with increasing processing speed of modern personal computers (PC).

Two channels of photon counts were acquired by the counter card PCI-6602 manufactured by National Instrument. The card is plugged to a PCI extension slot on a PC and

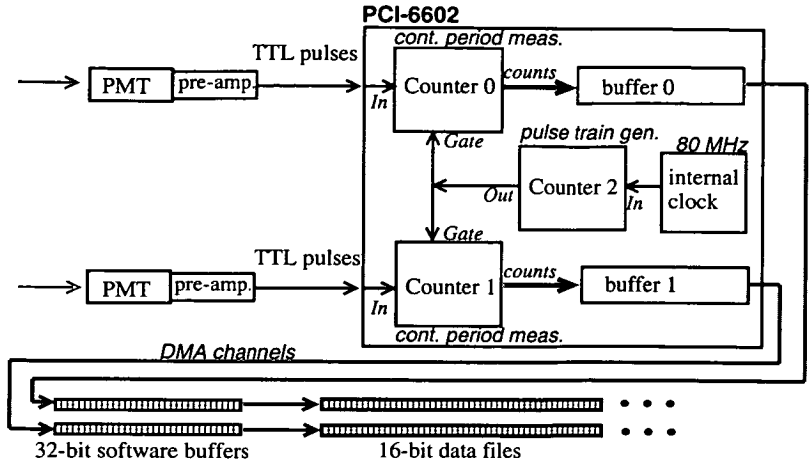

Figure 3.9: Schematic data acquisition path and counter card configuration. Photons arriving at the PMT generate pulses that are pre-amplified to TTL level. The signals enter the counter card as inputs for counters 0 and 1, both of which are configured to operate in *continuous period measurement* mode. Note that input lines are already terminated with 50Ω impedance inside the card. Counter 2 is configured to *pulse train generation* mode, which takes input from the internal clock and generate a train of pulses of period equal to the selected sample time s. This sampling clocking signal is used to gate counting in counters 0 and 1. The results of photon counts are continuously put in 2 internal buffers which are periodically read out by the software program `LinCount`. The software saves 2 streams of photon counts as 2 series of fixed-size files.

configured to count the number of detected photon pulses every sample time s (see figure 3.9). These counts are saved as 16-bit *samples* in 2 series of binary files, one for the blue stream (stream 0: `namebase.0.000`,`namebase.0.001`, ...), and one for the green stream (stream 1: `namebase.1.000`, `namebase.1.001`, ...), where `namebase` is a user-defined name. All characteristics of the data streams are saved in a text file named `namebase.inf`. This informative file is then read by other data analysing programs that can be run simultaneously while data is being acquired, resulting in an almost real-time analysis of the scattering experiment.

3.3.2 Modified multi-tau scheme

For almost all cases, a very large range of dynamical information is of interest. Therefore one usually needs to know the correlation function at delay times logarithmically spaced out. The results of this is that a very large amount of information 'between the points' at large τ is not used in linear sampling scheme. In order to make use of this 'lost' information, Schätzel introduced the multi-tau scheme [67], in which the sample time used to calculate a correlation channel is proportional to the delay time of that channel. However, in echo DLS the requirement of correlating intensity at one speckle to that at the same speckle a long time afterwards is absolutely crucial. Thus a simple multi-tau scheme as in [67] does not work as it averages intensities of neighbouring speckles in the process.

I introduced a modified multi-tau scheme where correlation between intensities at exactly the same speckle was maintained while the sample time s was effectively increased for increasing delay time. The main feature of this modified scheme was that sample time was increased by averaging intensities at exactly the same speckle at neighbouring revolution (figure 3.10). Intensities from the same angular position at two consecutive periods were averaged to give one new sample. Thus the effective sample time for each new sample was now twice the old one. The new averaged values were then put into new streams which were then correlated in the same way for longer delay time. In order to ensure that intensities at the same speckle were added, precise measurement of the period was required. This value was readily available by computing at least one echo from the original intensity without using multi-tau. The position of this echo allows the period to be calculated with relative uncertainty of about 10^{-6}.

As the sample time was doubled, the actual two samples that were averaged were separated by one period in time. Therefore the delay time of the correlation channel calculated with the averaged sample must be considerably larger than one period to reduce distortion due to averaging. In this scheme, I used the original data stream to

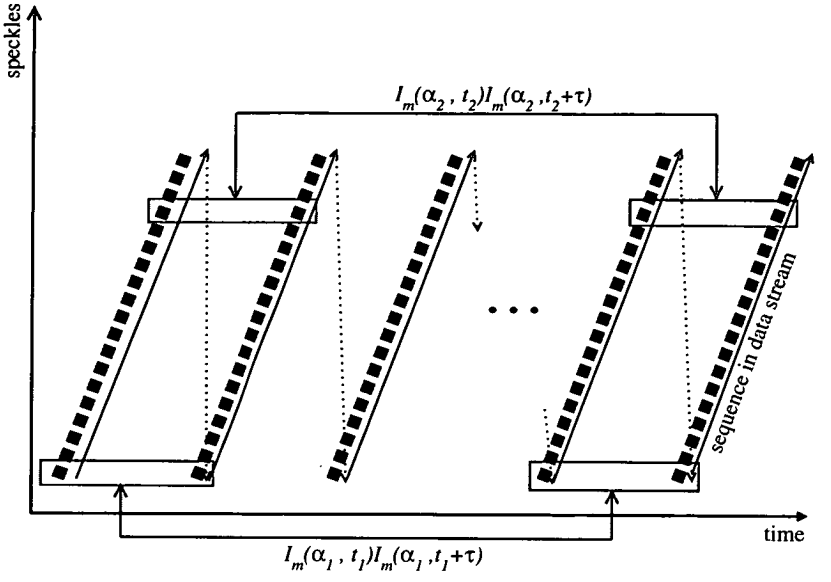

Figure 3.10: Modified multi-tau scheme for echo DLS. Pairs of counts from the same angular position are averaged to give a new sample. These make up a new sample stream with the sample time effectively doubled. The new streams are then used to calculate the correlation function in the same way for larger delay time. This procedure is repeated several times.

	Effective sample time	Sample temporal coverage	echoes	range in τ
Original data	s	s	0-16	1-16 T
1st average	$2s$	T	9-16	18-32 T
2nd average	$4s$	$3T$	9-16	36-64 T
3rd average	$8s$	$7T$	9-16	72-128 T
...	...	...	...	...

Table 3.1: A typical choice for effective sample time and correlation delay time in modified multi-tau scheme. s is the sample time, T is the period of rotation. There are 16 echoes in the first octave, then 8 every subsequent octave. The sample time is doubled every step, so the total number of samples is halved. The total time for calculating the correlation function is therefore reduced.

calculate $g^{(2)}$ up to the 16th echo. Then the sample time was doubled and the new stream was used for $g^{(2)}$ from the 9th to 16th echoes of the new sample time, which corresponded to echoes 18 to 32 of the original sample time. This was repeated as many times as necessary to achieve the longest delay time. The procedure is summarized in table 3.1. This selection of sample times and delay times ensured that the delay time was at least 16 times larger than the separation between averaged samples, which introduced a triangular distortion of no more than 10^{-3} [68].

3.3.3 Echo symmetry

The theoretical prediction of the echo profile is a symmetric peak always greater than 1 (equation 3.23 and figure 3.2). However, in practice, we know that there is smearing of this profile, and this smearing is by no reason symmetric. In fact, one would expect this smearing to be asymmetric as the sample is rotated only in one direction. We indeed found that most echoes are somewhat asymmetric, especially near the base line (figure 3.11).

With two-colour DLS, I performed the cross-correlation between the two intensity signals from two wavelengths of the setup. Thus there were 2 choices for the direct stream. These are denoted by $g^{(2)}_{0\times1}(\tau)$ and $g^{(2)}_{1\times0}(\tau)$, with $I_0(t)$ comes from the blue stream, and $I_1(t)$ comes from the green stream:

$$g^{(2)}_{0\times1}(\tau) = \frac{\langle I_0(t)I_1(t+\tau)\rangle}{\langle I_0(t)\rangle\langle I_1(t+\tau)\rangle} \tag{3.42}$$

$$g^{(2)}_{1\times0}(\tau) = \frac{\langle I_1(t)I_0(t+\tau)\rangle}{\langle I_1(t)\rangle\langle I_0(t+\tau)\rangle} . \tag{3.43}$$

The definition of $g^{(2)}_{1\times0}(\tau)$ can be re-written with a shift of $-\tau$ in time t:

$$g^{(2)}_{1\times0}(\tau) = \frac{\langle I_1(t-\tau)I_0(t)\rangle}{\langle I_1(t-\tau)\rangle\langle I_0(t)\rangle} = g^{(2)}_{0\times1}(-\tau) . \tag{3.44}$$

Therefore one can transform the 1×0 cross-correlation to a negative delay time simply by negating τ and put both $g^{(2)}_{0\times1}(\tau)$ and $g^{(2)}_{0\times1}(-\tau)$ together for comparison.

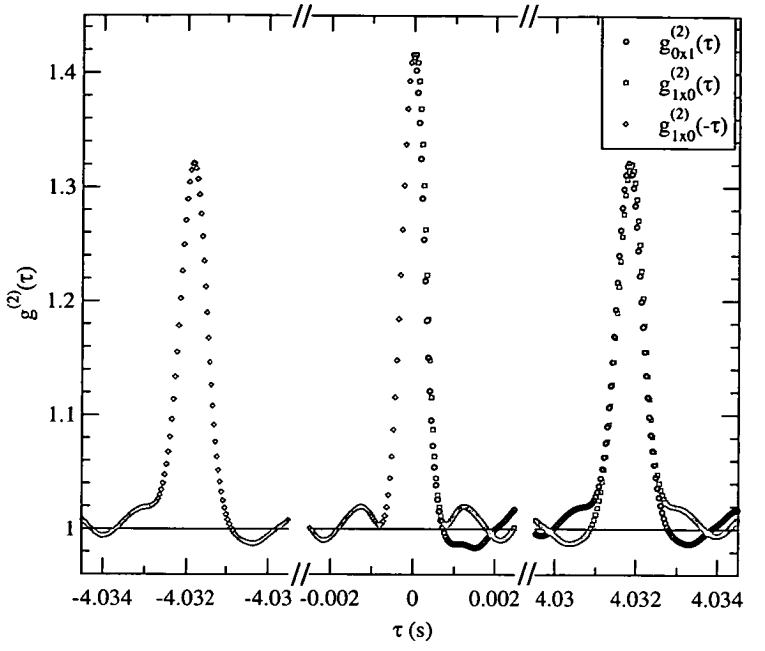

Figure 3.11: Comparison of 0×1 and 1×0 correlation modes of a rigid sample. The shape of the peaks of the 2 modes are not symmetrical about $\tau = 0$ but shifted in τ domain (the full diamond and circle peaks on the sides). The full zero echo is made up from the 0×1 mode and the reflected 1×0 mode (diamonds and circles at the centre). The non-zero peaks are wider and lower than the zero-th echo due to smearing effect as discussed in section 3.2.3. Some fluctuations near the baseline of the zero-th echo are smeared out in other echoes.

As the peaks are not symmetric, these two cross-correlation are not exactly the same but related in a rather interesting manner.The shapes of the echoes at τ and $-\tau$ are not symmetric about zero but simply translated by $2\tau_n$, where $\pm\tau_n$ are the positions of the peaks in comparison (figure 3.11). This 'direction of time' in the τ space indicates that the distortion of the peak shapes strongly correlates to the rotation of sample, i.e. it is the imperfect rotation that gives rise to the distortion.

There are two channels of data available in two-colour DLS that are slightly different due to the reasons described above. To improve the statistics of the final result by making use of both channels, they were averaged before further analysis. Moreover, the asymmetry of echo peaks should be preserved before any smearing correction as it is the manifestation of the smearing. Therefore the following procedures were used to

obtain the averaged ICF for further analysis. The 1×0 mode function $g^{(2)}_{1\times0}(\tau)$ is first reflected about $\tau = 0$ to give the negative delay time section $g^{(2)}_{0\times1}(-\tau)$. Each echo in this function is then shifted by $2\tau_n$ before averaged with the peak from $g^{(2)}_{0\times1}(\tau)$. So the average ICF at the n-th echo ($n > 1$) with a maximum at τ_n that is used for further analysis is calculated as:

$$g^{(2)}(\tau \sim \tau_n) = \frac{1}{2}\left(g^{(2)}_{0\times1}(\tau) + g^{(2)}_{1\times0}(2\tau_n - \tau)\right), \tag{3.45}$$

where τ_n is the average of the two maximum positions from $g^{(2)}_{0\times1}(\tau)$ and $g^{(2)}_{1\times0}(\tau)$, both of which were found to be very close (typically $\sim 10^{-6}T$) in all cases.

For the zero-th echo ($\tau \sim 0$), the 1×0 data was simply reflected and joined to the 0×1 section:

$$g^{(2)}(\tau) = \begin{cases} g^{(2)}_{1\times0}(-\tau) & \text{for } \tau < 0 \\ g^{(2)}_{0\times1}(\tau) & \text{for } \tau \geq 0 \end{cases} \tag{3.46}$$

It should be noted that in a conventional single-colour DLS experiment, there is only one incident-scattered beam pair, producing one intensity stream. Thus there is no way to sense the direction of the rotation. The obtained ICF is therefore symmetrical about $\tau = 0$, and the above averaging procedure is not necessary.

3.3.4 Smearing correction

Imperfect sample rotation and its smearing effect were observed in almost all measurements with the echo method (see e.g. Fig. 3.11). The effects are introducing significant noise and even systematic error to the maximum values of the echoes (Fig. 3.12). It was shown in section 3.2.3 that in such cases, it is essential to use the area under the echo peak to measure the intrinsic dynamics of the sample. The normalization by area is done as following. First, the area under each echo and above the baseline, $A(\tau_n)$, including the zero-th echo, is calculated:

$$A(\tau_n) = \int_{\tau\sim\tau_n} \left(g^{(2)}(\tau) - 1\right) d\tau, \tag{3.47}$$

where $g^{(2)}(\tau)$ is the measured ICF (or in the case of two-colour DLS, is the average according to Eqs. 3.45 and 3.46). The integral limits will be discussed below.

Knowing the area under the echo is conserved under smearing but scaled by the dynamics (Eq. 3.40), the smearing-corrected correlation function $g_s^{(2)}(\tau_n) \equiv 1+\beta^2[f(q,\tau_n)]^2$ at echo n was then constructed as:

$$g_s^{(2)}(\tau_n) = \frac{A(\tau_n)}{A(\tau_0)}\left[g^{(2)}(0) - 1\right] + 1, \tag{3.48}$$

where $A(\tau_n)$ and $A(\tau_0)$ are the areas under the n-th and the zero-th echoes respectively; $g^{(2)}(0)$ is the maximum value of the zero-th echo, $g^{(2)}(\tau = 0)$.

It should be noted that the application of the modified multi-tau scheme to improve statistical accuracy may inadvertently 'average out' the effect of smearing. Thus the additional smearing correction may not have the same effect as rigorously proved in section 3.2.3. However, it seemed that even though the modified multi-tau scheme reduced the random fluctuation due to smearing from one echo to the next, it could not eliminate the accumulated smearing effect (the rise in relative FWHM at $\tau \approx 5 \times 10^3$ seconds in Fig. 3.12(a)). Yet the smearing correction that followed seemed to eliminate that almost entirely (Fig. 3.12(b)). Many experiments carried out on rigid samples showed that the smearing correction worked well with the modified multi-tau scheme.

The above smearing correction however does not verify the assumption that the fluctuation in rotating angular speed is limited and the average speed is stable over the whole experiment. To verify that assumption and monitor the extent of the smearing effect, one can use another feature of the echo: the full widths at half maximum (FWHMs) of the peaks above the baseline (Fig. 3.13). Since the FWHM is not dependent on the area under each echo, i.e. independent of the intrinsic dynamics of the sample, it is a good candidate for the measure of the 'quality' of the rotation. The relative FWHM compared to that of the zero-th echo is a measure of the extent of smearing on the shape of the obtained echo (Fig. 3.12(a)). For perfectly constant speed rotation, the values of all FWHM of all echoes should be the same as that of the zero-th echo, therefore all

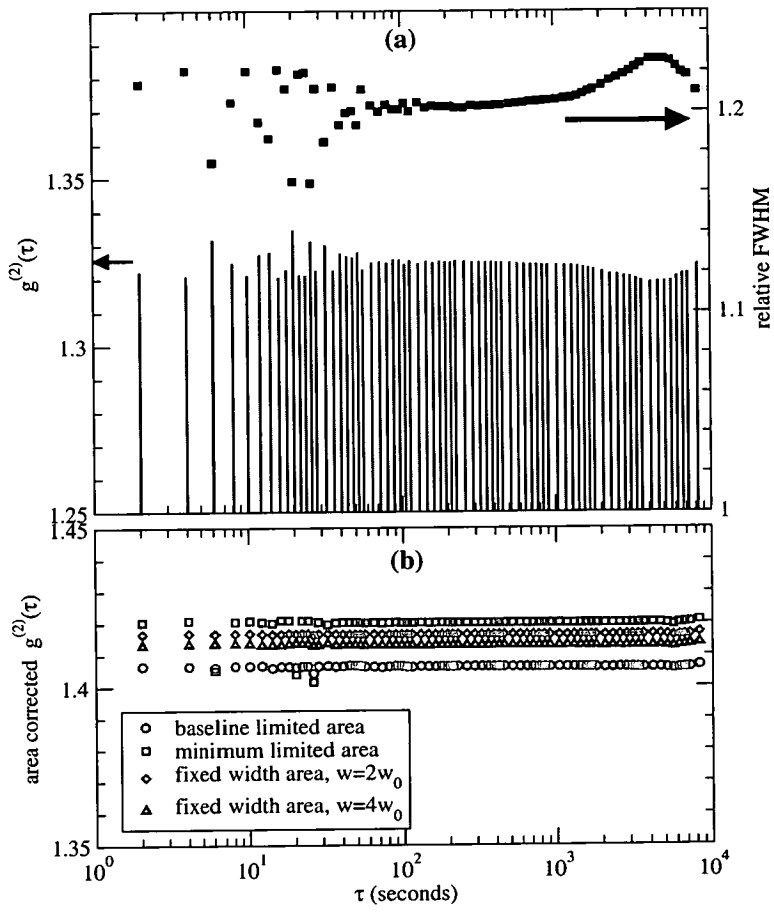

Figure 3.12: Echo ICF from a rigid sample calculated with modified multi-tau scheme. (a) The vertical lines are echoes with large fluctuation at low τ due to smearing, part of which has been averaged out yet still present at large τ. The filled squares are corresponding full width at half maximum (FWHM) of each echo, measured relative to the FWHM of the zero-th echo, scales on right. (b) Smearing corrected correlation functions using different area integration schemes. There are offsets between the schemes but data within each scheme are consistent and more accurate than prior to correction.

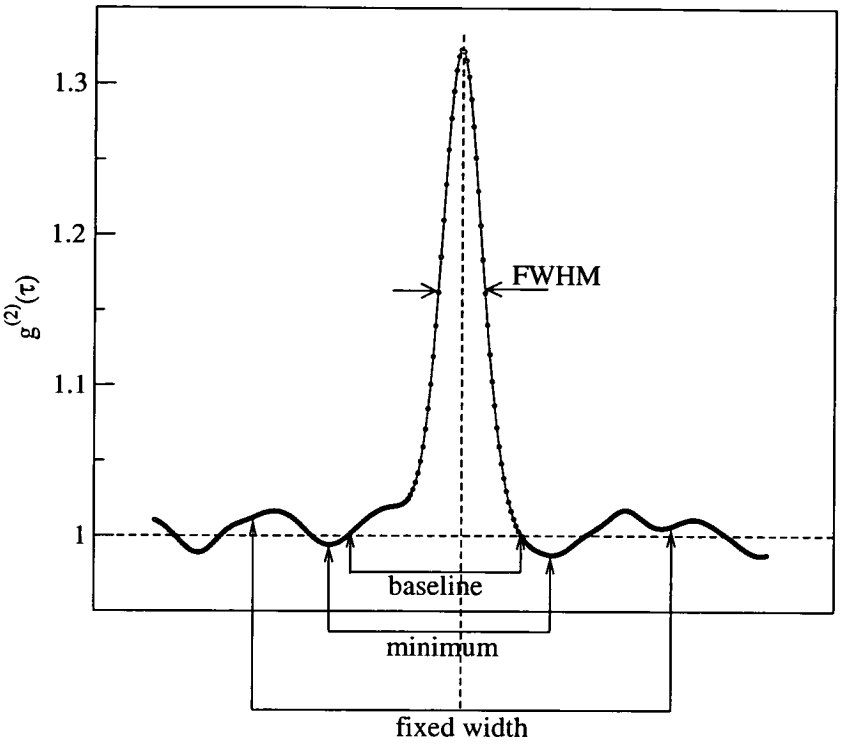

Figure 3.13: Limits to calculations of the area under each echo peaks. The full width at half maximum (FWHM) is used as a measure of the extent of smearing effect.

relative FWHMs are equal to one. If the rotation is not completely smooth, then smearing will occur and the relative FWHMs will not be constant and greater than one. If the rotation speed is not stable, i.e. average speed drifts away due to large friction, the relative FWHM will diverge at large τ. Thus by monitoring the FWHM as a function of τ, one can evaluate the quality of the rotation before applying smearing correction.

There are several ways to choose the integration limits in equation 3.47. Theoretically, the correlation function $g^{(2)}(\tau)$ is never less than and approaches the baseline value of 1 away from the main peak. However, in almost all measurements, $g^{(2)}(\tau)$ fluctuates about 1 even very far from the echo peak. This fluctuation is due to random noise in the average intensity used for normalization from the limited number of independent speckles observed. Our typical experimental setup observed about $p = T/(\text{echo width}) \sim 3000$ speckles, which gives a random error of $\sqrt{1/p} \approx 2\%$.

This uncertainty also applies to the intercept of the ICF. This fluctuation in the base-line is unavoidable and too complicated to correct for in data analysis. Instead I tried different empirical limits to calculate the area and typical results for a rigid sample are presented in figure 3.12(b). The measured correlation function is the result of a 'true' echo superimposing on a fluctuating background around 1. Furthermore, the relative position of the real echo changes with respect to minima and maxima of the background, and it seems this relative position that complicates the choice of the most appropriate limits. The simplest choice is the '*base line*' limit. The limits of integration are chosen to be the last point above 1 when moving away from the peak of the echo. This works relatively well in some cases. However, in the case where the echo does not reach 1 in a rather large range of τ, several background fluctuations are included in the area calculation. Results in these cases are not very smooth.

Another simple choice is the '*minimum*' limit, where the first local minima in $g^{(2)}(\tau)$ either side of the peak are used as limits. This method seems to work well with quickly decaying ICF from ergodic samples, where the background fluctuation is very small due to a large number of independent speckles observed. In most of other cases it does not give very good results, usually with a few points having very high or very low values (squares in Fig. 3.12(b)).

The last choice is the '*fixed-width*' limit where the range of integration for area is fixed to the same value either side of the peak and the same for all echoes, including zero-th echo. This method seems to work relatively well for most cases. However, the difficulty is to make the right choice of the integration width. Ideally, one would like to calculate the area with an infinite width to average out all fluctuation in the background. However, even if that approach were practical, the area calculated would not converge but fluctuate about a mean value. It is this mean value that we need for the area. It was found that a value for the width equal to a multiple (no less than the maximum value of the relative FWHM) of the zero-th echo width w_0 produced rather good results, with w_0 defined by the first minimum in $g^{(2)}(\tau)$ in the zero-th echo. Even the choice of

integration limits made seemed somewhat arbitrary to make the end result of $g_s^{(2)}(\tau)$ a smooth function, the correction eliminated spurious fluctuations in the original data due to imperfect rotation, yet did not introduce any other except from small random noise.

The intercept $g^{(2)}(0)$ obtained with echo DLS was in general less than that obtained in brute-force ensemble averaging. This was mainly because the rotation of the sample introduces a different alignment of the sample to the light scattering setup (thus a different β^2), and random wobbling of the sample leads to an incomplete returning of the same speckle. The latter effect cannot be corrected by the smearing correction. These factors were instrument-related and different in different samples, different scattering angles, so very difficult to determine or calibrate. Therefore in order to join echo data to those obtained by ensemble averaging at shorter delay time, I scaled the intercept by an arbitrary factor (in the range 1–2) to match with data obtained by other techniques in the region of overlap.

3.4 Discussion

A comparison of $f(q,\tau)$ obtained using echo DLS and an average of 100 conventional time-averaged correlations of a metastable ergodic colloid-polymer sample at $q = 14.51\ \mu\text{m}^{-1}$ is presented in figure 3.14. A more detailed description of this sample can be found in [69]. The agreement of the two techniques in the overlap region is excellent. Note that the echo data was of much better quality at large τ despite a 20-fold shorter measurement time. This good agreement of the two techniques and that with the expected result in a rigid sample (Fig. 3.12) are very convincing that the echo DLS method can give very good quality data in much shorter measurement time.

Ideally, the measurement time t_m required to obtain dynamical data of maximum delay time τ_{max} is just τ_{max} plus one period for ensemble averaging of the longest delay time:

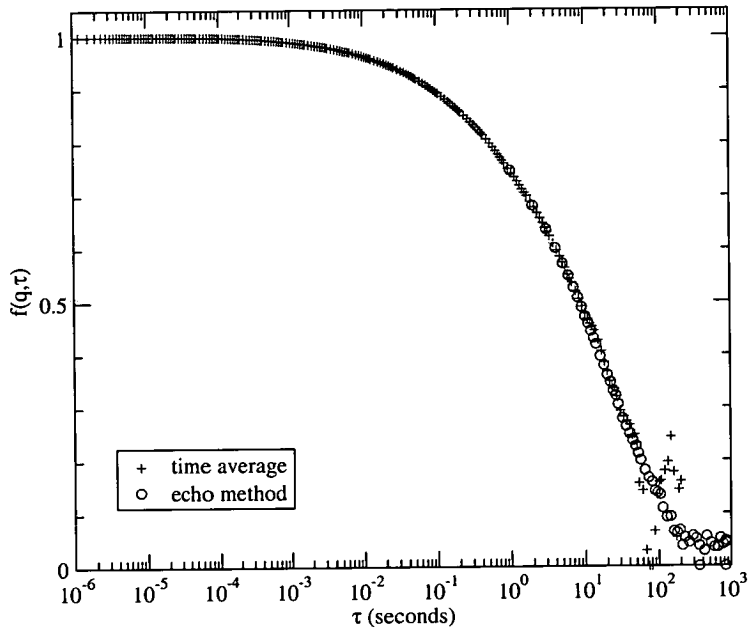

Figure 3.14: Comparison of the normalized DSF of a slowly-relaxing colloid-polymer mixture measured by average of 100 time-averaged measurements (crosses) and by echo technique (circles). The echo data were scaled by an arbitrary intercept to match to time-average ones. There was good agreement of the two methods in the overlap region. The echo measurement taken in 2300 seconds gives significantly better statistics at long τ than the time-averaged one which took 5×10^4 seconds (~ 14 hours) in total to complete.

$t_m = \tau_{max} + T$. Even with imperfection in rotation, this measurement time is required to extend for only a few hundred periods to average over all fluctuations in angular speed, so that t_m is still of the order τ_{max}. With today's computer speed and hard drive capacity, the computation of ICFs with modified the multi-tau scheme had about the same speed as data being acquired. Thus echo DLS data can be obtained almost in real time, and there is virtually no upper limit for τ_{max}. One can easily obtain dynamical information up to 10^4 seconds in about 1.5×10^4 seconds (4 hours) of measurement time.

Compared to other methods of measuring non-ergodic dynamics, echo DLS has certain advantages. Firstly, it does not require high spatial coherence over detector aperture as in the Pusey-vanMegen method [49]. In fact, an ICF with any intercept, i.e. any level

of coherence, can be measured with echo DLS. Therefore this technique is suitable for use in cross-correlation schemes like two-colour [51] or three-dimensional [60] DLS where the intercept depends on sample turbidity and is often significantly lower than one.

Secondly, echo DLS is not constrained to the small scattering angle limit as with some multispeckle setups [61, 62]. Compared to another multispeckle arrangement which uses a CCD camera as detector in a conventional DLS setup [63], echo DLS can average the dynamics over a larger number of speckles, typically several thousands (ratio of period to echo width) without compromising the resolution of the scattering angle. This advantage gives echo DLS the ability to produce data with low level of random noise due to a limited number of independent speckles sampled. This noise is particularly pronounced in highly non-ergodic samples, i.e. samples whose measured dynamics is almost frozen and have a high value of $f(q, \infty)$.

Finally, compared to the interleaved sampling method [65] whose principles of obtaining ensemble average is very similar, echo DLS introduces some major improvements. The interleaved sampling method also rotates the sample but by a stepper motor through a large number of positions. At each position, a sample of the scattered intensity is acquired and correlated to the intensities at the same position in previous revolutions so that a time-averaged ICF is obtained for each position. These ICFs are then averaged to obtain the ensemble-averaged ICF. This method is equivalent to calculating a single delay time $\tau_n = nT$ at the exact peak of every echo. On the other hand, echo DLS calculates the correlation function over a range of delay time around $\tau = nT$ thus also obtains the shape of the echo, thus it is possible to correct for any smearing due to imperfect rotation by using the echo area. It is also unnecessary to synchronize sample rotation and correlator, enabling the use of a continuous servo motor that can produce a smooth rotation. Moreover, the quality of any rotation can be monitored by the apparent width of the echoes, to ensure that the smearing effect is not too large and correction can be applied.

However, there is a drawback of this method. That is its complete lack of data for $\tau < T$, which is typically about one second. Any much faster rotation will produce, apart from mechanical difficulties, instability of rotational speed and possible unwanted disturbance to the sample. Therefore some other methods such as brute-force ensemble averaging should be used to obtain short time data up to $\tau \sim 10$s. These data joined with echo DLS allow one to measure dynamics of non-ergodic samples over a very large dynamical range, typically from 10^{-6} to 10^{4} seconds.

Chapter 4

Methods and experiments

This chapter describes the methods and procedures used in sample preparation, as well as observation and light scattering experiments to obtain structural and dynamic information of colloid-polymer mixture samples near the glass transitions.

4.1 Sample preparation

4.1.1 Colloids

The colloidal particles used in this study were poly-methylmethacrylate (PMMA) spheres sterically stabilized by chemically-grafted poly-(12-hydroxystearic acid) (PHSA). The particles, synthesized by Dr. A. B. Schofield with methods in [70], were originally dispersed in dodecane which is not a suitable solvent for this work. The chosen solvent is instead *cis*-decahydronapthalene (*cis*-decalin) as its refractive index is close to that of PMMA (1.48 and 1.49 respectively). To replace the solvent, colloids were 'washed' several times. Suspensions were centrifuged before discarding dodecane and re-dispersed in *cis*-decalin. Since the old solvent was trapped between close packed particles after centrifuging and cannot be discarded completely, the particles were

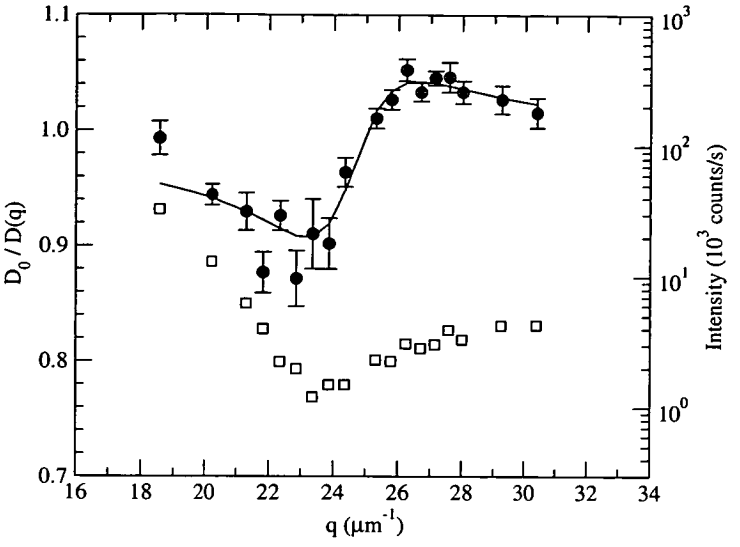

Figure 4.1: Variation in diffusion coefficient $D(q)$ in dilute colloid stock near the form factor minimum (filled circles) measured with two-colour DLS. The continuous line are fit of Eq. 33 in [72] to measured data, giving the polydispersity $\sigma = 0.069 \pm 0.004$. The singly-scattered intensity (squares) are shown with scale on the right.

washed for at least 6 times so that the fraction of dodecane left in the solvent is less than 10^{-4}. Refractive index of the final solvent was also measured with an Abbe refractometer and found to be the same as that of *cis*-decalin within the instrumental error ($\sim 0.05\%$).

The PMMA particles with the solvated PHSA, approximately 10nm thick, behave like nearly-hard-sphere [71]. The particle hard-sphere radius, $R = 202$nm, was determined by Dr. A. B. Schofield from the lattice spacing of the crystal phase at fluid-crystal coexistence with static light scattering, using the crystal volume fraction $\phi_m = 0.545$. Particle size polydispersity was 0.069 (Fig. 4.1), measured from the apparent angle dependence of the diffusion coefficient in a dilute suspension [72].

The colloidal volume fraction was calibrated by measuring the amount of crystal phase in the coexistence region and assuming the fluid and crystal volume fraction to be at 0.494 and 0.545 respectively, taking into account slow compaction of the crystal phase by gravity [73]. This volume fraction corresponds to the 'hard-sphere' size of the

particles which include the stabilizing layer and is larger than the PMMA core.

The effective density of the composite particle (core + stabilizing layer) is needed for further sample preparation. Consider the particle as a sphere with a PMMA core of density ρ_{core} and volume V_{core} surrounded by a stabilizing layer of volume χV_{core}. Since *cis*-decalin is a good solvent for PHSA, the stabilizing layer is a solvated polymer layer, its density is assumed to be close to that of the solvent: $\rho_s \approx \rho_{\text{cis-decalin}}$. The effective density of the colloid particle is

$$\rho_c = \frac{\rho_{\text{core}} + \rho_s \chi}{1 + \chi}. \tag{4.1}$$

It depends only on the ratio χ of the volume of the stabilizing layer to that of the core. This ratio is a constant for each batch of colloids and needs to be measured once only by the following drying procedure.

Samples of the volume-fraction-calibrated stock were weighed to get the total mass m. They were then dried in a vacuum oven at 40°C for 24 hours so that all solvent was evaporated, and re-weighed to get the mass of the core m_{core} (the mass of PHSA polymer is negligible compared to that of the core). If the hard-sphere volume fraction of the sample is ϕ_0, the ratio χ can be shown to be

$$\chi = \phi_0 \left[1 + \frac{\rho_{\text{core}}}{\rho_s} \left(\frac{m}{m_{\text{core}}} \right) \right] - 1 \, . \tag{4.2}$$

The volume fraction of the colloid stock was also re-calibrated from time to time with the same drying and weighing procedures, by solving for ϕ_0 in the above equation knowing the ratio χ.

4.1.2 Polymer and mixing with colloids

To induce attraction between the colloids, non-adsorbing linear polystyrene was added. This well-characterized model colloid-polymer mixture has been studied extensively over the last decade [12]. The polymer used was purchased from Polymer Laboratories

and had a molecular weight of $M_w = 370000$ daltons and polydispersity $M_w/M_n = 1.03$. Its radius of gyration in *cis*-decalin at 20°C was calculated from the data in [74] to be $r_g = 17.8$ nm. Thus the dimensionless range of the depletion attraction is $\xi \sim r_g/R = 0.09$. The polymer is dispersed in *cis*-decalin to make a polymer stock of known mass concentration.

Colloid-polymer mixture samples were prepared by adding colloid stock, polymer stock and solvent together in appropriate proportions. The sample composition is quoted as colloid volume fraction and polymer mass concentration in the total sample volume (ϕ, c_p). However in practice, adding components by mass is much more accurate than by volume. The calculation of final composition as well as prediction of the amount of each component for a desired composition can be done straightforwardly by mass concentration. Let us define the mass concentration of colloid and polymer in a sample as $x = m_c/m$ and $y = m_p/m$, where m_c, m_p and m are masses of colloids (consist of PMMA core and stabilizing layer), polymer and total sample respectively. These can be calculated from ϕ and c_p from simple conservations of mass and volume:

$$x = \frac{\phi \rho_c}{\bar{\rho}} \tag{4.3}$$

$$y = \frac{c_p}{\bar{\rho}}, \tag{4.4}$$

where ρ_c is the effective density of colloids obtained from Eq. 4.1, $\bar{\rho}$ is the total density of the sample: $\bar{\rho} = \phi\rho_c + c_p + (1 - \phi - c_p/\rho_p)\rho_s$, with ρ_p and ρ_s are densities of polystyrene and solvent respectively. Since the volume taken up by polymer coils in a mixture is not known, ρ_p is not easily determined. In the simplest approximation, I used the tabulated density of solid polymer (1.05 g.cm^{-3}) for ρ_p and found that this quantity make very small changes in the final compositions of the sample due to small polymer mass fraction. Therefore the errors from not using the appropriate polymer density can be safely neglected.

Conversely, the volume fraction and polymer concentration can also be calculated from

mass concentrations x and y:

$$\phi = \frac{x}{v\rho_c} \tag{4.5}$$

$$c_p = \frac{y}{v}, \tag{4.6}$$

where $v = 1/\bar{\rho}$, calculated from x and y as: $v = x/\rho_c + y/\rho_p + (1 - x - y)/\rho_s$.

Since the volume concentration (ϕ, c_p) and mass concentration (x, y) can be calculated from one another, all calculations for sample preparation and actual concentrations was done in mass concentrations.

To prepare a new sample from a known one, with known total mass m_0 and known concentrations (x_0, y_0), one has to go through 2 stages. First, an estimated amount of stocks (either two of colloid, polymer stocks or solvent) to be added for the desired composition is calculated. Then, the final composition of the new sample is calculated from the actual amounts of stocks added. The second stage is straight forward, the same as calculating position of centre of mass:

$$x = \frac{m_0x_0 + m_1x_1 + m_2x_2}{m_0 + m_1 + m_2} \tag{4.7}$$

$$y = \frac{m_0y_0 + m_1y_1 + m_2y_2}{m_0 + m_1 + m_2}, \tag{4.8}$$

where m_1,x_1,y_1 and m_2, x_2, y_2 are masses and concentrations of the 2 stocks added.

In the first stage, the masses of added stocks are found by solving Eqs. 4.7 and 4.8 simultaneously for m_1 and m_2, given the desired x and y. If a solution is infinite, that scenario is impossible. If a solution is negative, the corresponding stock has to be taken out of the original sample — an impossible situation unless the original sample is a colloid stock and solvent is to be taken out. Since there are three possible stocks, three pairs of them are used in Eqs. 4.7 and 4.8 which were solved until an acceptable solution is found. However, to reduce uncertainties in the final concentrations, only the following combinations were used: (i) adding/removing solvent from colloid stock, then add polymer stock to make new sample. (ii) adding solvent to a known sample

to reduce concentrations. (iii) removing solvent by slow evaporation from a known sample to achieve higher concentrations.

Samples with a total volume of about 1 cm^3 were prepared in glass vials. The size of the sample requires the mass of each constituent component of no less than about 40 mg, large enough to be weighed accurately on a 100g electronic balance. For highly concentrated samples that need removal of solvent, appropriate amount of colloid stocks were centrifuged to compact all colloids before the desired amount of solvent was sucked out. Then the colloids was redispersed before adding polymer stock. Total sample mass was recorded for subsequent diluting or concentrating.

Samples with all components added were tumbled for prolonged periods of time (about 10^4 revolutions) to ensure proper mixing of the components. After homogenizing, a small amount of each sample was transferred to 3 mm inner diameter glass tubes and sealed with Araldite Rapid epoxy glue for light scattering experiments. The rest of the sample was then left undisturbed for visual observation of any phase transitions until sedimentation appeared. Then some samples may be diluted with solvent while others were left opened at room temperature for solvent to evaporate slowly before re-homogenizing by tumbling for at least 6000 revolutions. In this way, a sequence of samples, some very close in composition, could be prepared.

The main uncertainty in sample composition comes from a systematic uncertainty in the calibrated volume fraction of the colloid stock. This is because the volume fractions of coexisting fluid and crystal phases for slightly polydisperse hard-spheres are slightly different from those in a monodisperse colloid, but the exact values are uncertain [75, 76]. However, all samples were prepared from the same stocks of colloids and polymer solutions, or stocks calibrated against each other. Some samples were also derived from others in a controlled way (described above). Therefore despite some systematic uncertainties in the estimation of absolute volume fractions due to polydispersity, the uncertainties in sample compositions relative to each other were mostly from random

errors in weighing which are below a percent in the worst case and are insignificant in this work.

4.2 Two-colour light scattering

The high colloid volume fraction ($\phi > 0.5$) and difference in the refractive indices of PMMA and *cis*-decalin (1.49 and 1.48 respectively) was enough to render all the samples of interest turbid (transmission coefficients $\approx$ 20–40%). I therefore used two-colour light scattering to extract the singly-scattered component. The theoretical background of the two-colour technique was outlined in section 2.3.4 and fully laid out in [51]. In this section I will describe the modifications to the setup of [51].

The two-colour light scattering setup was arranged in principle as that described in Fig. 4 of [51], except a few modifications (Fig. 4.2). First the whole setup was powered by a single Ar^+ laser set to emit all lines. The beam after attenuation by the reflective neutral density filter NF was split by the beam splitter cube BS. Each beam is passed through an interference band-pass filter so that a green ($\lambda_G = 514.5$ nm) and a blue ($\lambda_B = 488$ nm) beam are produced for the scattering experiment. On the detection optics, the imaging lens L2 was a compound lens consisting of 2 identical planar-convex lenses and was arrange with the planar surfaces pointing *outwards* to reduce abberation in the 1:1 imaging configuration. Thus the scattering volume image position (P1) does not change for different scattering angles. The outputs of the two detectors were cross-correlated to give the intensity correlation function (ICF) according to Eq. 2.42.

The concentrations of polymer in my samples were low. The highest ratio of intensity scattered from polymer to that from colloid was measured to be 4×10^{-3}. This highest ratio only applied for one sample (H in Fig. 5.3) at the lowest scattering angle. Therefore I assume that the scattered intensity is from colloids only. Under these conditions, all light scattering measurements probe the structure and dynamics of colloid particles

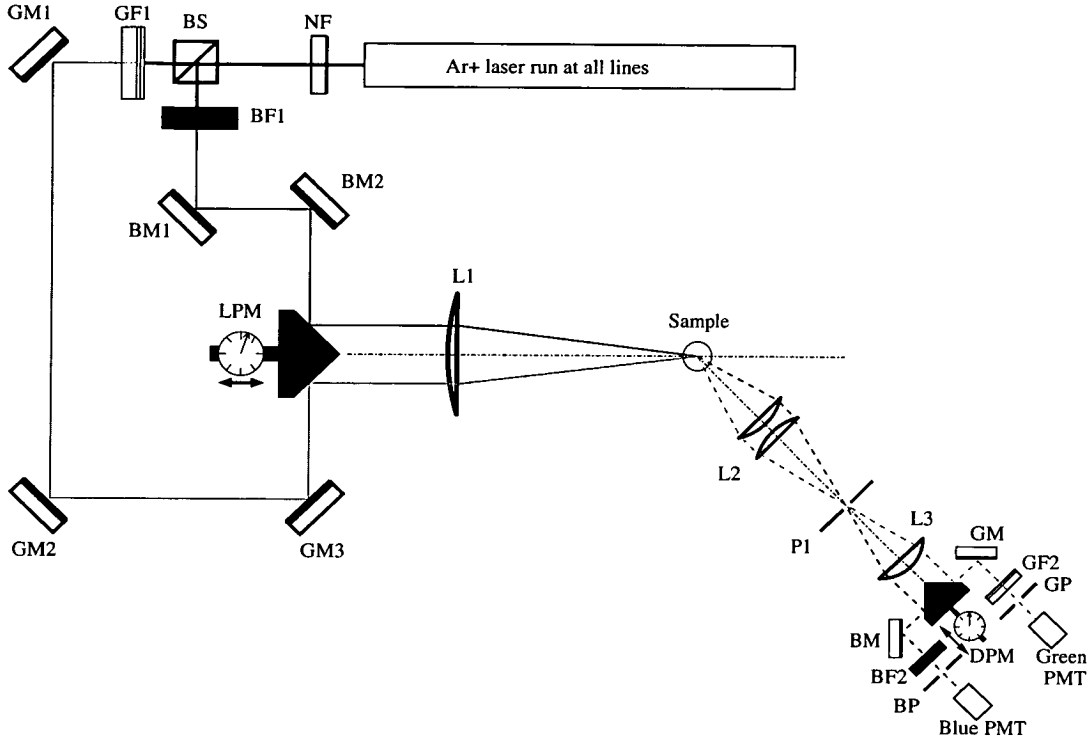

Figure 4.2: Schematic arrangement of the two-colour light scattering setup. The basic arrangement is the same as Fig. 4 of [51], except it is powered by a single laser with beam splitter BS and bandpass filters BF1, GF1, and L2 is a compound lens. The drawing is not to scale.

alone. All light scattering experiments were carried out at 20°C .

4.3 Static light scattering

The static structure factor was measured with the procedure described in [52]. First, the total average intensities, $\langle I_B \rangle$ and $\langle I_G \rangle$, and the intercept, $c \equiv g^{(2)}(q,0) - 1 = \beta^2 \beta_{MS}^2$ (from Eq. 2.43), of a concentrated sample of interest were measured at different scattering vectors q. The sample was rotated continuously during the measurement to obtain an ensemble average. Since the rotation only changes the time-dependence of $g^{(2)}(q,\tau)$, the intercept and average intensity were not affected. It was found that it was necessary to average measurements at different vertical positions in the non-ergodic samples to reduce random noise from the finite number of speckles observed. From Eq. 2.44, the average single-scattered intensity is $\langle I^S \rangle = \sqrt{\beta_{MS}^2 \langle I_B \rangle \langle I_G \rangle}$.

The factor β_{MS}^2 is not yet known but the product $\beta^2 \beta_{MS}^2$ is from the intercept. Besides, the particle form factor $P(q)$ is also needed for the SSF. Therefore the same measurements were made on a dilute suspension of known volume fraction ϕ_{dil} to obtain the single-particle form factor. The volume fraction of this dilute sample was $\phi_{dil} = 0.01$, small enough that multiple scattering can be ignored, so that the measured intercept contains only the instrument related factor: $c_{dil} \equiv g_{dil}^{(2)}(q,0) - 1 = \beta^2$, which was the same as that in the measurement of the concentrated sample. The factor β_{MS}^2 can now be obtained: $\beta_{MS}^2 = c/c_{dil}$. The measurements of concentrated and dilute samples were made immediately after one another to reduce uncertainties in laser beam intensity and stability.

The volume fraction of the dilute sample, $\phi_{dil} = 0.01$, though small is enough to make its SSF $S_{dil}(q)$ vary slightly with q according to Percus-Yevick results. To compensate for this variation, the dilute sample is assumed to have Percus-Yevick SSF at the corresponding volume fraction.

Since multiple-scattering is significant, the attenuation of light along the path must be taken into account. Any emerging scattered light has gone through a path equal to the diameter of the sample cell and is reduced by a factor T due to scattering along the path. The transmission T is measured as the ratio of intensities of transmitted beam which went straight through the sample and incident beam (without sample). This quantity was measured separately for each colour on each concentrated and dilute sample as the ratio of transmitted to input light intensity. The static structure factor was then calculated according to Eq. 2.37, taking attenuation and dilute SSF into account:

$$S(q) = \frac{\phi_{dil}}{\phi} \frac{\sqrt{T_{B,dil} T_{G,dil}}}{\sqrt{T_B T_G}} \frac{\sqrt{\langle I_B \rangle \langle I_G \rangle c/c_{dil}}}{\sqrt{\langle I_{B,dil} \rangle \langle I_{G,dil} \rangle}} S_{dil}(q) \,, \tag{4.9}$$

where the subscripts B, G, dil are for blue, green light, and dilute sample respectively.

4.4 Dynamic light scattering

The objective of DLS is to measure the normalized collective dynamic structure factor $f(q,\tau)$ introduced in section 2.2. This is done by measuring the intensity correlation function $g^{(2)}(q,\tau)$ with two-colour DLS (Eq. 2.42) and normalizing it with the Siegert relation (Eq. 2.40):

$$f(q,\tau) = \sqrt{\frac{g^{(2)}(q,\tau) - 1}{g^{(2)}(q,0) - 1}} \tag{4.10}$$

However, since most samples investigated in this study either were non-ergodic or had very slow relaxation times, the time-averaged ICF did not represent the proper ensemble-averaged dynamics. The DSF was therefore separately measured in two regimes: the long-time dynamics by echo DLS, and the short-time one by brute-force ensemble averaging as a compliment to echo DLS technique.

Brute-force ensemble averaging was done for the short-time regime $10^{-7}\text{s} < \tau <$ 20s. Several hundred (typically between 500-865) of time-averaged ICFs, $g_t^{(2)}(q,\tau)$,

and associated scattered intensities, I_{Bt} and I_{Gt}, were measured with an ALV-5000 correlator, each for a duration of 40–60 seconds. Between each measurement, the sample was rotated by a small angle to a different position so that each time-averaged ICF sampled a different Fourier component. The time-averaged ICF is:

$$g_t^{(2)}(q,\tau) = \frac{\langle I_B(0) I_G(\tau)\rangle_t}{I_{Bt} I_{Gt}} . \tag{4.11}$$

So the ensemble-averaged ICF is

$$g^{(2)}(q,\tau) = \frac{\langle \langle I_B(0) I_G(\tau)\rangle_t \rangle}{\langle I_B\rangle \langle I_G\rangle} \tag{4.12}$$

$$= \frac{\left\langle I_{Bt} I_{Gt} g_t^{(2)}(q,\tau)\right\rangle}{\langle I_{Bt}\rangle \langle I_{Gt}\rangle} . \tag{4.13}$$

In the long time range $1 - 10^4$ seconds, echo DLS was used with period of rotation $T = 1$ or 2 seconds. Details of the procedures and data analysis method were given in section 3.3. The smearing corrected ICF at $\tau = nT$ ($n = 1, 2, 3, \ldots$) was calculated from the measured ICF according to Eq. 3.48 and normalized according to Eq. 4.10.

Since the rotation used in echo DLS introduced slightly different alignment in the DLS setup (hence different β^2), the resulting intercept was different from that obtained by brute-force ensemble averaging. Therefore I scaled the intercept of the echo DLS results by an arbitrary factor (in the range of 1–2) so that the resulting DSF from both methods matched in the region of overlap.

4.5 Polymer viscosity for re-scaling colloid dynamics

The goal of studying the DSF is to find out how the polymer-induced depletion attraction affects the particle dynamics. But the presence of the polymer influences the dynamics in another (uninteresting) manner — by increasing the effective viscosity of

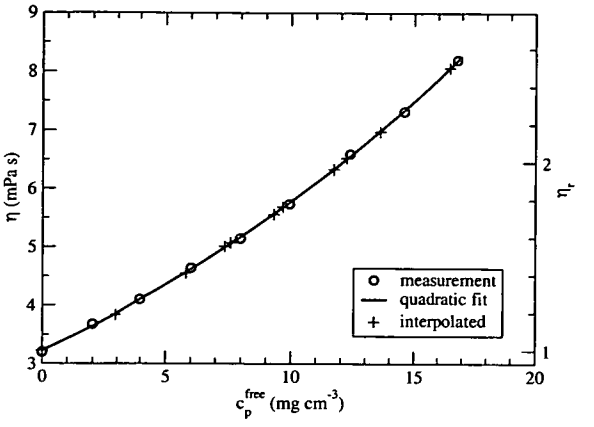

Figure 4.3: Viscosity of polystyrene solutions in *cis*-decalin at 20°C at different polymer concentrations. A quadratic fit (solid line) was used to interpolate to viscosities of samples with different c_p^{free}.

the medium in which the particles diffuse from that of the pure solvent, η_0, to that of a polymer solution, η at concentration c_p^{free}. The real effects of adding polymer to colloids dynamics is rather complicated [77]. Nevertheless, to the simplest approximation I assume the dynamics of colloid particles due to added polymer can be separated to two factors: a trivial slowing down due to an increase in viscosity of the medium, and a complicated effect due to the induced attraction. It is the second effect that is the main objective of this work.

To compensate for the slowing down due to increase in background viscosity, the relative viscosity, $\eta_r = \eta/\eta_0$, of the polymer solution suspending the colloids is required. The viscosity of pure polystyrene solutions at a number of concentrations was measured with a miniature suspended-level viscometer as described in [77]. The results at 20°C are presented in Fig. 4.3. Since the polymer concentration in my samples was small, the viscosity was expected to follow an Taylor expansion of concentration up to order two [78]. The result was fitted to a quadratic dependence in concentration to interpolate the relative viscosity at concentrations c_p^{free} corresponding to free polymer concentration in samples used in DLS. The value of c_p^{free} in each sample was estimated with Eq. 2.7 from c_p, ϕ and ξ using an approximate expression (Eq. 2.4) based on

scaled-particle theory [19].

Chapter 5

Results and discussion

This chapter will describe results from many colloid-polymer mixture samples of different compositions, prepared by methods described in chapter 4. Their phase behaviour were observed to draw up a phase diagram. Structure and dynamics of selected samples were measured to explore the physics behind the glass transition.

5.1 Phase behaviour

5.1.1 Equilibrium phase behaviour

After being homogenized by prolonged tumbling, samples were left undisturbed for observation. Because the size of colloidal particles is similar to wavelengths of visible light, colloidal crystals can be seen with the naked eye as iridescent specks. The equilibrium phase behaviour of this system is in general agreement to that of other well-known colloid-polymer mixture with small size ratio [13].

The phase behaviour is shown in Fig. 5.1. In agreement with equilibrium theory [19] for systems with short-range attraction, I observed an expansion of the fluid-crystal coexistence region upon increasing polymer concentration (open circles and diamonds).

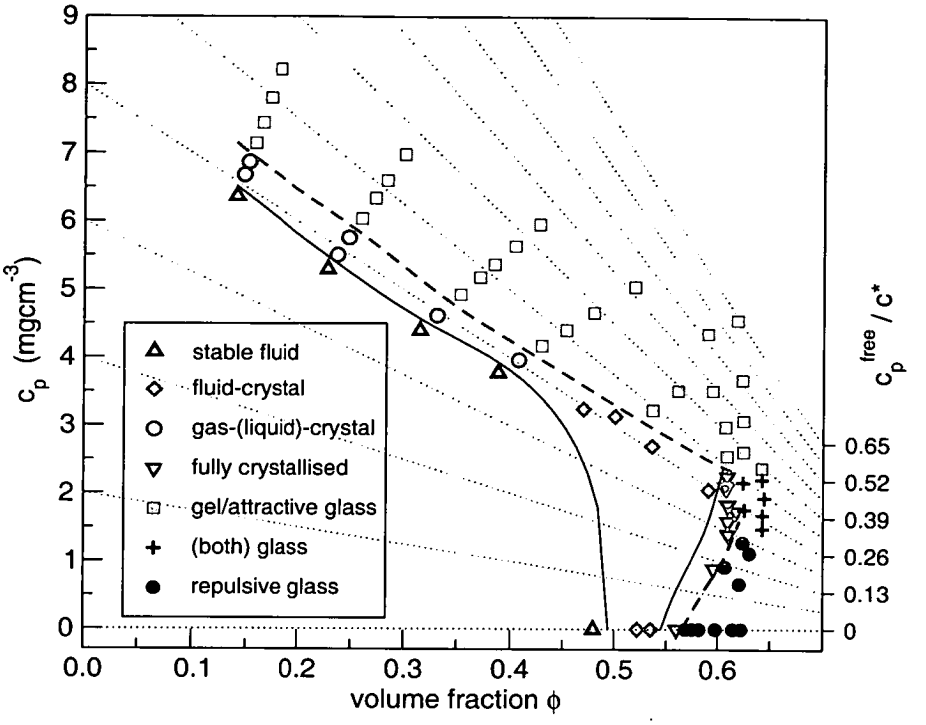

Figure 5.1: Equilibrium and non-equilibrium behaviour of a colloid-polymer mixture of $\xi = 0.09$. Open symbols are those that reached thermal equilibrium (fluid, fluid-crystal coexistence, and fully crystallized), the samples denoted by circles went through a gas-liquid separation before a final fluid-crystal (see text). Other samples did not crystallize: some showed characteristics of hard-sphere glasses at the onset of sedimentation (filled circles), some showed those of attraction-driven glasses and gels (filled squares), and some showed both (pluses). Dashed and solid curves are guides to the eye of the observed boundary where crystallization ceased and fluid-crystal coexistence boundary respectively. The dotted lines are lines of equal c_p^{free} estimated by scaled particle theory, expressed as fractions of the overlap concentration on the right.

To the left of this region is a stable fluid phase (triangles) and to the right is the fully crystalline phase (inverted triangles). These observations also agree with previous experiments on similar systems [13].

However, there was a difference between fluid-crystal coexisting samples at low volume fraction ($\phi < 0.45$, open circles in Fig. 5.1) and those at higher volume fraction. The low volume fraction samples first underwent a gas-liquid transition before most or all of the liquid crystallized. This delay in crystallization may be attributed to the

slight polydispersity ($\sigma \approx 0.07$) of the colloids. A previous study of a similar system with higher polydispersity ($\sigma \approx 0.09$) also observed gas-liquid separation where fluid-crystal coexistence was expected [79]. The rest of section 5.1.1 will be a digression to further elucidate these observations.

It is known that the induced short-range attraction compresses the colloidal crystals to a higher volume fraction. Particles in a denser crystal phase are closer together and thus can accommodate less polydispersity. A simple criterion by Pusey based on Lindemann [79, 80] suggests that a crystal phase is not stable if the mean nearest neigbour distance is shorter than touching separation of two large particles with radius $\sim (1 + \sigma)\bar{R}$. Thus the maximum volume fraction of polydisperse crystals in this system is estimated to be $\phi_{\max} \approx 0.74/(1 + \sigma)^3 = 0.60$. If this simple explanation is adequate, even qualitatively, for the suppression of direct crystallization in some samples, all samples above a certain tie line (say, the dark thin line in Fig. 5.2) which will give crystal with $\phi > \phi_{\max}$ cannot crystallize. However, this is *not* supported by experimental observations. Samples lying around a single dotted curve in Fig. 5.1 with similar attraction strength (i.e. approximately on the same tie line) showed a range of crystallizing behaviour, including some at higher ϕ that reached fluid-crystal coexistence and even full crystallization in one step (diamonds and inverted triangles in Fig. 5.1).

Relaxing the Pusey-Lindemann criterion of a discrete threshold for polydisperse crystals, one realizes that the difficulty of obtaining a polydisperse crystal is encapsulated in the cell theory of solids [81] as a decrease in entropy for larger polydispersity. Using the free energy for polydisperse hard spheres estimated by cell theory, it was possible to calculate an approximate theoretical equilibrium phase diagram for a polydisperse colloid-polymer mixtures (details in appendix). The results show that polydispersity simply narrows the fluid-crystal coexistence region relative to the monodisperse case (Fig. 5.2).

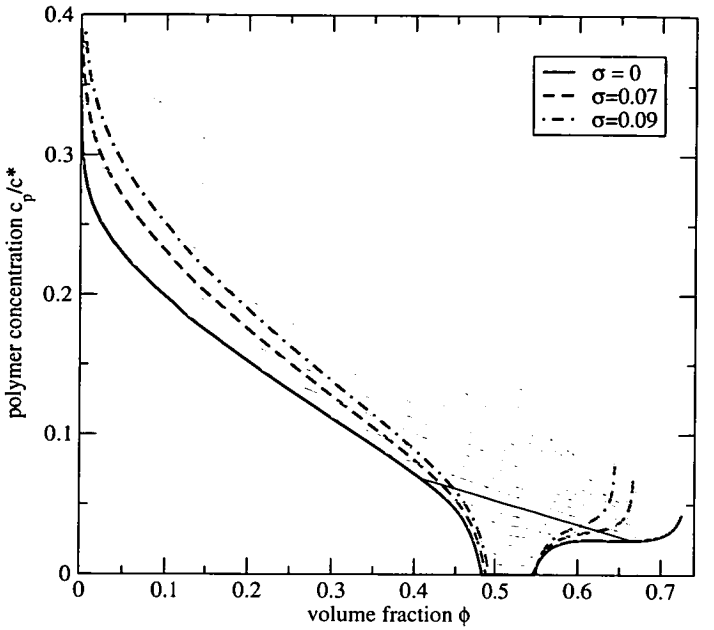

Figure 5.2: Theoretical equilibrium phase diagram for polydisperse colloid-polymer mixture with $\xi = 0.08$ using cell theory free energy. The thick lines are fluid-crystal coexistence lines for different polydispersities, showing fluid-crystal coexistence region narrows when polydispersity increases. The thin lines are tie lines of the monodisperse case, the dark one indicates the limit above which no crystallization is possible with the Pusey-Lindemann criterion.

It could be speculated that polydispersity brings the equilibrium fluid-crystal coexistence boundary much closer to the metastable gas-liquid binodal. Just inside the former, crystallization would not be observed because the low thermodynamic driving force. But when there is enough polymer to bring the system inside the metastable gas-liquid binodal, gas-liquid demixing may occur, and occur very quickly because it requires no symmetry breaking. The dense liquid phase resulting from this process may then subsequently crystallize. This two-stepped crystallization process has been observed before in colloid-polymer mixtures [82], where the close proximity of the metastable gas-liquid binodal and the equilibrium fluid-crystal boundary was brought about by tuning the temperature.

It is known that gas-liquid demixing in a polydisperse colloid-polymer mixture leads to fractionation in the average size as well as polydispersity in the two phases [83]. In

Sample	$\bar{R}$ (nm)	σ
Parent	182 ± 1	0.069 ± 0.004
HS fluid	182 ± 1	0.075 ± 0.004
HS crystal	181 ± 1	0.070 ± 0.004
CP fluid	174 ± 1	0.095 ± 0.003
CP crystal	183 ± 1	0.060 ± 0.002

Table 5.1: Fractionation of size and polydispersity in fluid-crystal transition. In hard sphere (HS), fractionation does not seem to be significant, whereas fractionation of both size and polydispersity is significant in a colloid-polymer mixture (CP). The measured mean radius quoted is hydrodynamic radius.

the two-stepped scenario suggested above, one therefore may expect that the resulting crystals were also fractionated relative to the parent homogeneous fluid.

To verify the fractionation of two coexisting phases in this system, polydispersities of the fluid and crystal phases were measured for two samples in the fluid-crystal coexistence: sample HS is a hard sphere suspension with $\phi = 0.54$, $c_p = 0$, sample CP with $\phi = 0.47$, $c_p = 3.2$ mg.cm^{-3}. Both samples showed normal one-step crystallization to a fluid-crystal coexistence. After the phase separation was completed, a small amount of each phase was extracted and its polydispersity was determined by the q-variation of apparent diffusion coefficient in dilute DLS measurement [72]. The results in Table 5.1 showed that the hard-sphere fluid-crystal transition did not introduce significant fractionation within the experimental uncertainties, whereas the same transition in colloid-polymer mixture did. More significantly, it showed that in sample CP the denser phase (crystal) which favoured larger particles had lower polydispersity than the parent as well as the less dense phase. This is consistent with previous measurements showing that gas-liquid phase separation gave a liquid phase with larger and less polydisperse particles [79, 83].

The fact that there was a significant difference in the amount of fractionation in the

two samples could be explained by the following arguments. In sample CP, the final phases had very different colloid volume fractions ($\sim$ 0.05 and 0.7 according to theory). To reach that state, a large scale migration of colloidal particles from one part of the sample to another was required. This macroscopic movement of particles due to the driving force of the phase separation would certainly facilitate any separation of size species as well. On the other hand, the hard sphere sample HS reached its equilibrium with two phases of relatively similar volume fractions (0.49 and 0.55). The phase separation into such final densities would not require as much macroscopic migration of particles as in the case of sample CP, hence an insignificant fractionation. Therefore any studies on fractionation should consider the kinetic process during which it happens.

5.1.2 Non-equilibrium phase behaviour

The non-equilibrium behaviour of systems with $\xi \approx 0.1$ at low volume fractions ($\phi < 0.2$) has been studied before [14, 22]. This work concentrated on the higher volume fraction region ($\phi \geq 0.5$) where MCT predicts the existence of different glassy states [35, 36]. Observations in this region are shown in Fig. 5.3. In addition to equilibrium phases, samples with very high colloid volume fractions and/or polymer concentrations (filled circles, squares and crosses) failed to crystallize for weeks to months even though equilibrium statistical mechanics predicts either fluid-crystal coexistence or full crystallinity.

Samples with high colloid volume fractions and low polymer concentrations (filled circles in Fig. 5.3) showed all the characteristics of hard-sphere colloidal glass [1]. Weeks after homogenization and left undisturbed, sedimentation showed its effect: very thin layers at the top of the samples developed heterogeneous crystals due to the boundary effect of the meniscus and gravity. Samples denoted by squares in Fig. 5.3, with high polymer concentration and moderate colloid volume fraction, showed signs of

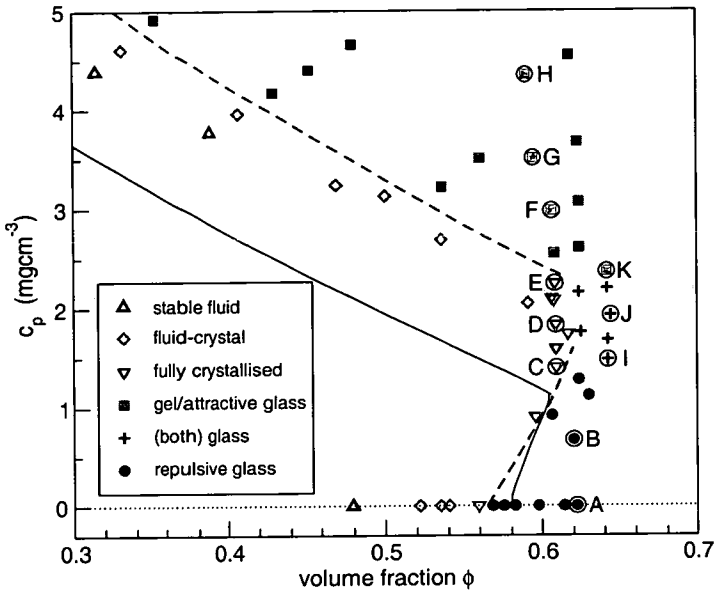

Figure 5.3: The high volume fraction area of Fig. 5.1. Open symbols are samples that reached thermodynamic equilibrium, the others did not crystallize for weeks. The dashed lines are guides to the eye of the observed boundary where crystallization ceases, showing a re-entrant behaviour. The solid line is MCT prediction of the glass transition for the system with $\xi = 0.08$ [37, 35]. Light scattering data for marked samples labeled A–K are shown in sections 5.2 and 5.3.

transient gels. They collapse under gravity after some 'latency time' as observed previously in similar systems [14, 22]. However, the amount of collapse decreased and transient time increased dramatically in higher volume fraction samples. For concentrated samples with colloid volume fraction above 0.55, it took more than 4 weeks to see tiny collapses of less than half a millimeter at the very top of the meniscuses of samples $\sim$ 2cm high. These collapses were distinguished from normal sedimentation by their characteristic sharp and non-flat boundary between the collapsed material and a clear supernatant. No crystallization was observed in these samples however long they were left undisturbed. Interestingly, for non-crystallizing samples with very high colloid volume fraction and polymer concentration (crosses), characteristics of both hard-sphere glass and transient gels were present. After 4–8 weeks, tiny collapses were seen, and also a thin layer of crystal phase appeared just under the collapsing

boundary.

Consider a sequence of samples of similar colloid volume fraction and increasing attraction, for example samples A–H in Fig. 5.3 with $\phi \sim 0.6$. According to thermodynamic equilibrium theory, all these samples should crystallize [19]. Sample A without polymer was a glass. Sample B with a small amount of polymer was also a glass as no homogeneous crystallization was observed for 4 weeks and only heterogeneously nucleated crystals at the meniscus were observed after 13 days. However, sample C with ~ 1.4 mg cm^{-3} of polymer completely crystallized in 1 day. This means the glass transition line has moved to higher ϕ, a trend that has been observed before in similar system [15]. Failure to crystallize was seen again for samples with polymer concentration above ~ 2.5 mg cm^{-1} (samples F,G,H). The behaviour of all the samples in this region taken together show that the line of failure to crystallize had a re-entrant shape.

In pure hard-spheres, crystallization ceases at essentially the same volume fraction as where $f(q, \infty)$ first becomes non-zero, i.e. at the glass transition [2, 5]. If this coincidence still holds for attractive hard-spheres systems, then I have observed a re-entrant glass transition in hard spheres with short-range attraction. This observation agrees qualitatively with MCT results for an AO attraction with $\xi = 0.08$ [37, 35]. The agreement is remarkable despite the MCT results contains no adjustable parameter except a scaling of ϕ so that hard-sphere glass transition is at $\phi = 0.58$.

Previous studies of sticky hard spheres by MCT [35, 36] and computer simulation [37, 43] suggest that the re-entrant behaviour is due to two different mechanisms of glassy arrest. The heuristic picture is as follows. In the 'repulsion-dominated' hard-sphere glass, particles are caged by their neighbours at high enough volume fraction. Short-range attraction clusters the particles of the cage and opens up holes, ultimately melting the glass. However, increasing the attraction further leads to an 'attraction-dominated' glass where particles stick to their neighbours with long-lived bonds. In this terminology, samples A and B are repulsive glasses and F–H are attractive glasses.

Samples I–K must lie in the region where these two types of glass merge as they show characteristics of both types, with further evidence in the dynamics shown in section 5.3. The next sections, with results from light scattering, will give insights into the structure and dynamics of these glasses, and the nature of the re-entrant transition between them.

5.2 Static structure factor

The static structure factors (SSF) of the samples whose symbols are circled in Fig. 5.3 were measured. Note that samples C–E were measured as metastable fluids, i.e. before any crystal nucleation took place. Consider first the results for a sequence of samples (A–H) with $\phi \approx 0.6$, Fig. 5.4. These samples span the re-entrant glass transition line where the crystallization behaviour showed dramatic changes. However, no re-entrant behaviour can be seen in the SSFs. Instead, there are only gradual changes upon increasing the attractive interaction. These gradual changes have been predicted by theory [36], and observed before in other experimental systems [42].

The most obvious and most easily quantifiable changes are in the height and position of the main peak. Broadly speaking, and taking experimental uncertainties into account, the peak reduces in height and shifts to higher q when the attraction is increased (inset Fig. 5.4(a)). These trends are similar to those observed in a similar system of microgel-polymer mixtures which also shows re-entrant behaviour [42]. In detail, the peak position, q^*, remains constant (at $q^*R \approx 3.8$, samples A–D) until just before we enter the attractive glass region (sample E), whereupon it increases by $\approx 5\%$ to reach another constant value ($q^*R \approx 4$, samples F–H). These samples have approximately constant ϕ (in fact it decreases slightly from A to H, Fig. 5.3). The increase in q^* is the result of a significant fraction of neighbouring particles becoming trapped in each others' narrow depletion potential well when the attractive glass forms. Quantitatively,

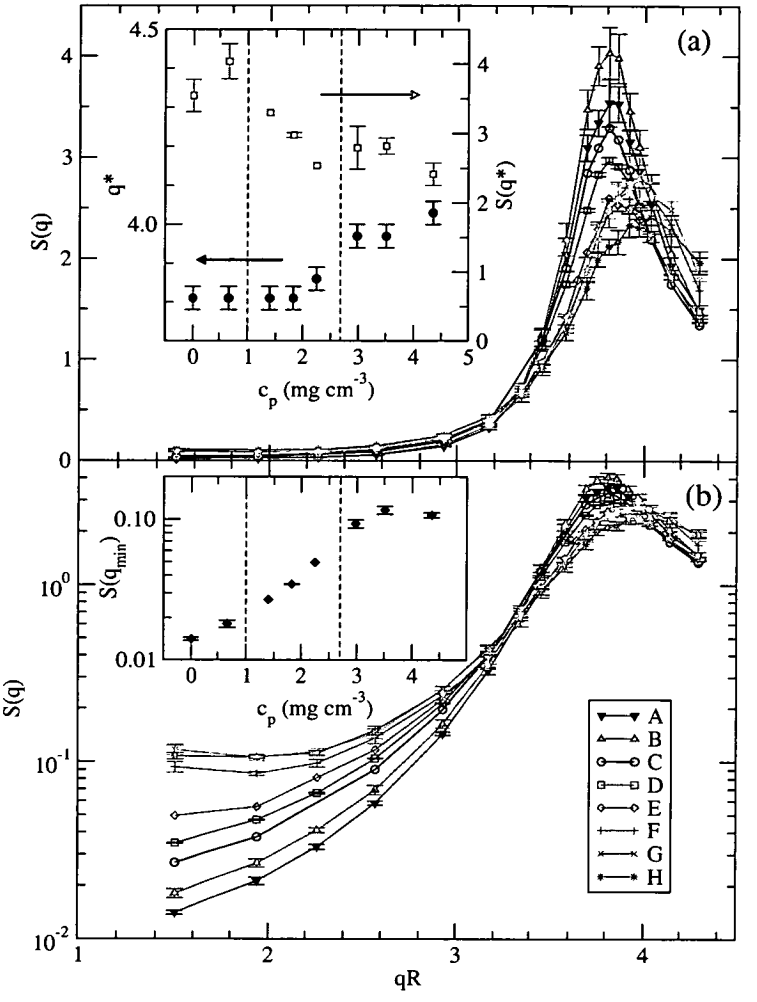

Figure 5.4: Static structures factor of samples A–H ($\phi \sim 0.6$) as function of dimensionless wave vector qR. The lines are guides to the eye. (a) The peak position q^* shifts to higher q, while its height reduces and width increases upon increasing attraction. The inset shows the peak positions and heights of these static structure factors as a function of polymer concentration. (b) The same SSFs plotted with logarithmic vertical axis shows the increase of $S(q)$ at low q. The inset shows $S(q)$ at the lowest wave vector $qR = 1.50$. Vertical dashed lines in both insets indicate the glass transitions observed in Fig. 5.3.

a 5% increase in q^* corresponds to a 15% increase in the local packing fraction, from 0.6 to 0.69; the latter is the same as the random close packing volume fraction for this system (measured by spinning down a sample of known ϕ). In other words, the nearest particles in the attractive glass are practically touching.

The clustering of particles at constant volume necessarily implies that the average number of nearest neighbours should decrease, and that 'holes' are opened up to render the structure more inhomogeneous on the spatial scale of a few particles. The former is reflected in the decrease in $S(q^*)$. Significantly, upon increasing the attraction from zero, the decrease in the peak height starts at the point of the melting of the repulsive glass, and continues until we enter the attractive glass region, whereupon the peak height remains constant (inset Fig. 5.4(a)).

The increased heterogeneity is reflected in a rise in the SSF at low q, Fig. 5.4(b). The smallest q studied was $q_{\min}R = 1.50$, corresponding to a length scale of about 4 particle radii. The value of $S(q_{\min})$ increases nearly exponentially with the polymer concentration between samples A–E (inset Fig. 5.4(b)), and thereafter remains constant. The increased density fluctuations at this length scale corresponds to the opening up of 'holes' due to particle clustering.

Note that all three features considered, q^*, $S(q^*)$ and $S(q_{\min})$, remain virtually constant for all three attractive glass samples, F–H. Once particles drop into each others' narrow attractive potential wells, any further *structural* changes will be hard to resolve. We shall see, however, that the *dynamics* continues measurably to evolve from sample F to sample H: in this regime of almost-touching nearest neighbours, a very small change in the structure has very large dynamic consequences.

All the qualitative features observed in the evolution of the SSFs for samples A–H are also seen in the SSFs for samples I–K at the higher volume fraction of $\phi \approx 0.64$, Fig. 5.5. However, the effects are significantly less obvious, largely because the range of polymer concentration is now much smaller and ϕ is higher. At low q, the values

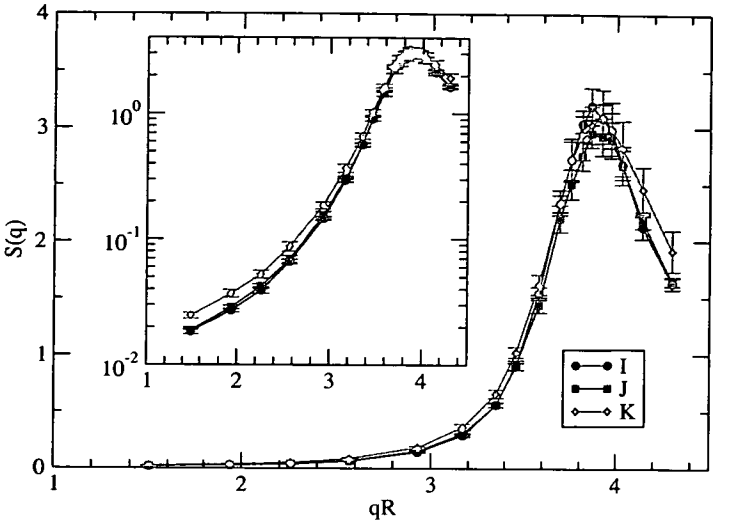

Figure 5.5: Static structure factors of samples I–K with $\phi \sim 0.64$. The inset shows the same data with a logarithmic vertical axis.

of $S(q_{\min})$ are lower than those of similar polymer concentration but lower ϕ (C–E) (Fig. 5.4(b)). This is because at higher volume fraction, a tight local clustering of some particles does not create so much room elsewhere — there is less space for developing heterogeneities.

5.3 Dynamic structure factor

As discussed in section 4.5, I assume the addition of polymer introduce an increase in solvent viscosity by a factor of η_r besides the effective induced attraction. All colloid dynamics will be normalized by this factor. Furthermore, the rate of dynamical decay at wave vector q depends on the length scale being probed; in dilute systems it scales as q^2. Thus, in order to compare the dynamics of different samples at different wave vectors, and to highlight the effects of the attraction, I scaled the delay time variable of the DSFs by the relative viscosity η_r and the dimensionless wave vector $(qR)^2$, so that DSF is presented as a function of the 'scaled time' $(qR)^2\tau/\eta_r$. Note that for the lowest q studied, the scaled time is very close to the real time, while at the highest q, it

is increased by about an order of magnitude.

Aging [84] was found in all non-crystallizing samples. The dynamics slowed down with the 'waiting time' — the time interval between the cessation of tumbling and the beginning of measurement, Fig. 5.6. It is known that the hard-sphere glass ages [54]. I found that the rates of aging in different glasses were different and that its effects were complex. Repulsive glasses aged only in the first day or two, after which they did not evolve within the time window of the measurements. Attractive glasses, on the other hand, showed different dynamics with age for up to 10 days. Aging is complicated enough to be the subject of a separate study and was not investigated systematically in this work. To eliminate as much as possible aging effects on dynamical results within practical limits of waiting time, I present DSFs of glassy samples with age between 1 and 4 days. The dynamics of crystallizing samples (C–E) were measured while they were in the metastable state well before the appearance of crystallization. Below I first show results of different samples at the same q, then at different q for the same sample.

5.3.1 Constant scattering vectors, variable compositions

The DSFs of samples A–H at $qR = 1.50$, Fig. 5.7, clearly evolve non-monotonically with increasing polymer concentration and show re-entrant behaviour. Briefly, samples A and B are non-ergodic within our time window, while samples C–E are ergodic (their DSFs decay completely to zero), and samples F–G become non-ergodic again.

In detail, the DSF of sample A, a pure hard-sphere glass, shows a plateau at $f_A(q, \infty) \approx 0.7$, corresponding to particles getting 'stuck' in their nearest-neighbour cages. This can be compared with previous work [5, 85]. Note that in doing so, it is important to compare samples with the same density *relative to random close packing*: i.e. the same $(\phi_{\rm rcp} - \phi)/\phi_{\rm rcp}$, since $\phi_{\rm rcp}$ differs according to the polydispersity of the colloids [86].

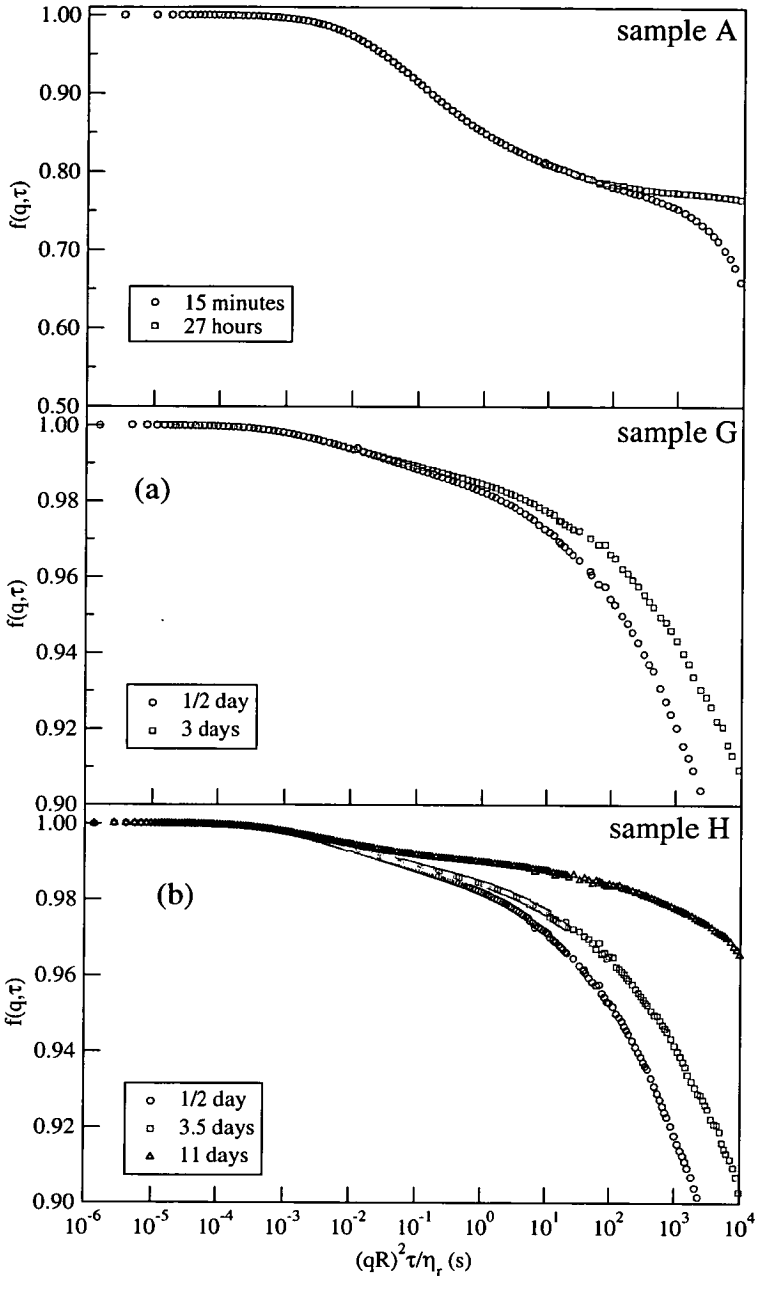

Figure 5.6: Aging in samples A, G and H at $qR = 2.93$. The legend indicates the waiting time between the end of tumbling and the start of measurements. The DSFs slow down and the points of inflection become clearer with increasing age of the samples.

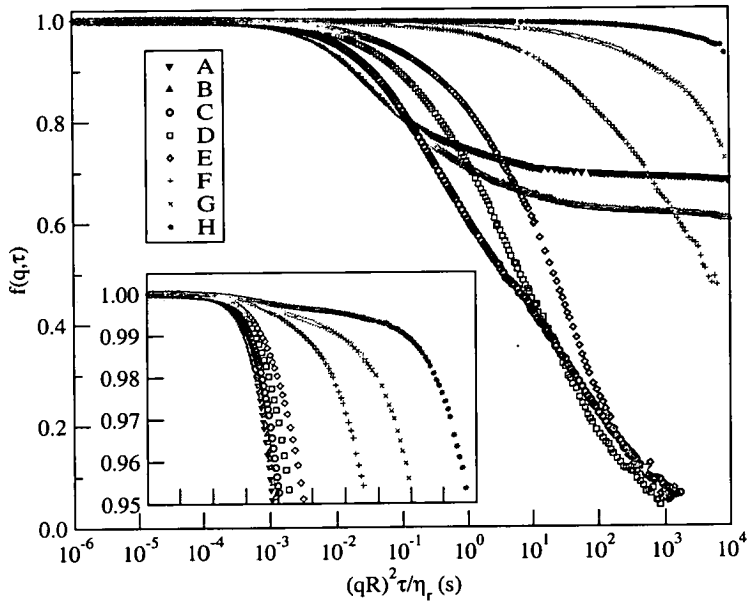

Figure 5.7: Collective dynamic structure factors at $qR = 1.50$ from samples A–H spanning the re-entrant region. The time axis is scaled to dimensionless length scale $(qR)^2$ and relative polymer solution viscosity η_r. The inset shows the same plots on an expanded vertical axis.

With a small amount of polymer added to the hard-sphere glass, sample B shows the same qualitative dynamics. Quantitatively, however, the height of the plateau is lower, $f(q, \infty) = 0.62$. This indicates that particles in B are not as restricted as in A, i.e. the cage is loosened by the attractive interaction, but still remains closed in our time window.

The DSF of sample C decayed completely in (a 'scaled time' of) about 1000 seconds, as did those for the other crystallizing samples D and E. It is interesting to note that the DSFs of these three samples slow down upon increasing polymer concentration but all reach zero at about the same scaled time. The DSF of sample C shows the remnant of a plateau at a scaled time of $\approx$ 10 s. The DSFs for samples D and E exhibit a very stretched *single* decay, rather than a two-stepped process. This is unusual behaviour for a fluid at volume fraction $\phi \sim 0.6$ (at least at first sight).

The intermediate, β, and long-time, α, decays in a dense hard-sphere fluid are at-

tributed to particles 'rattling' in their local neighbour cages, and escaping from these cages, respectively [5]. Attraction hinders the 'rattling' by trapping particles in potential wells, but accelerates the cage opening by clustering. At some polymer concentration (or attraction strength), the two time scales coincide. If at this point the attraction alone is not enough to trap the system in an non-ergodic state, we will observe the melting of the repulsive glass into an ergodic fluid dominated by attraction. This is the case for sample C, where the α and β decays are barely distinguishable in the DSF. At higher polymer concentrations, the cage concept is no longer appropriate for describing the particle dynamics — for it to be valid, a particle has to 'rattle' many times in a cage before it opens. Note that this is a distinctive feature of dense fluids with *short-range* attraction. In a dense fluid with *long-range* attraction, the effective potential well experienced by any particle due to its neighbours is essentially flat. This adds a (negative) constant to the free energy, so the phase behaviour [87] and dynamics of the system are still controlled by repulsion (or, equivalently, entropy).

Note that the shape of the DSF of sample C at $qR = 1.50$ is similar to that shown in curve 2, Fig. 11 of [36]. This DSF was calculated at $qR = 2.1$ for a sample in the reentrant portion of the state diagram in a system that *just* shows a glass-glass transition and an A3 point. Recent calculations for colloid-polymer mixtures [35] suggests that this system, with $\xi \approx 0.09$, should show exactly these features.

The DSFs of samples F–H are, once more, non-ergodic in my experimental time window: they do not decay completely even after 10^4 seconds. Simple extrapolation indicates that it would take these DSFs at least 10^6 seconds to reach zero. The DSFs of samples G and H show points of inflection; that for sample H is clearer and occurs at $f = 0.995$ — a very high value compared to the plateaus in hard-sphere glasses. These high points of inflection can be associated with dynamics originating from particles rattling in very narrow attractive potential wells.

At other wave vectors, Figs. 5.8 and 5.9, the DSFs behave in a similar way, namely rel-

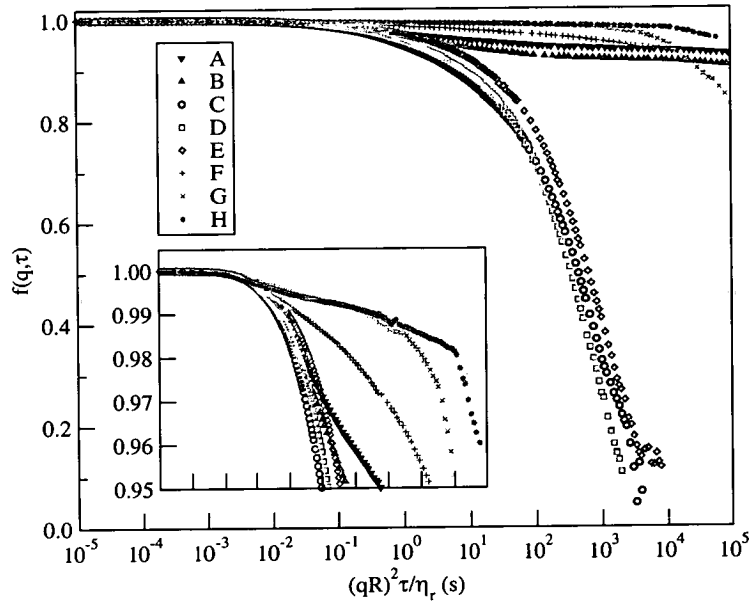

Figure 5.8: DSFs at the peak of the SSFs for samples A–H. The inset shows the same plots on an expanded vertical axis.

atively low plateaus in the repulsive glasses A and B, complete decay in the metastable fluids C–E, and extremely slow dynamics in the attractive glasses F–H, with very high points of inflection in G and H. Note, however, that at the peak of the corresponding SSFs, the DSFs for samples C–E are barely distinguishable (Fig. 5.8).

The plateaus in the DSFs of the repulsive glasses can be used as a measure of $f(q,\infty)$, the non-ergodicity parameter. An estimate of this quantity for the attractive glasses is more problematic, partly due to significant aging in my time window. To proceed, I use the value of f at the point of inflection as a surrogate; and call this the 'measured' $f(q,\infty) \equiv f^{(M)}(q,\infty)$. The evolution of $f^{(M)}(q,\infty)$ with increasing polymer concentration (samples A–H) is shown in Fig. 5.10. The non-ergodicity parameter decreases slightly when moving from A to B, away from the hard-sphere glass. When attraction melts the repulsive glass, $f^{(M)}(q,\infty) = 0$ for samples C–E (not shown). Sample F did not crystallize and showed non-ergodic dynamics up to 10^4 seconds but did not exhibit any discernible point of inflection in its dynamics. Samples G and H had extremely

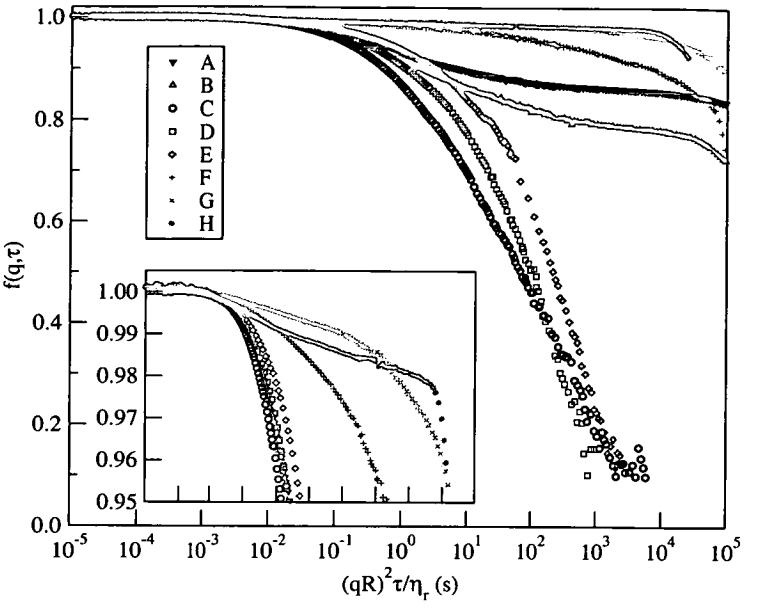

Figure 5.9: DSFs of samples A-H at $qR = 4.30$, to the right of all $S(q)$ peaks. The inset shows the same plots on an expanded vertical axis.

high non-ergodicity parameters of nearly 1. A 'jump' in $f(q, \infty)$ when moving from repulsive to attractive glass was predicted by MCT (Fig. 7 in [36]).

The evolution of the short-time dynamics of the whole sequence of samples is also interesting. Fig. 5.11 shows the short-time behaviour of the DSFs for A–H at large length scale, $qR = 1.50$, where experimental noise is lowest. Note the very small vertical interval, 0.997 to 1.000, spanned in this figure; thus only the first 0.3% of the decays of the DSFs are being analyzed. The DSFs of repulsive glasses A and B possessed relatively long linear parts, corresponding to the first term in τ in the expression derived from the Smoluchowski (many-particle diffusion) equation [28]: $f(q,\tau) = 1 - \frac{D_0 H(q)}{\eta_r S(q)} q^2 \tau + O(\tau^2)$, where D_0 is the free-particle diffusion constant in pure solvent (with no polymer) $D_0 = k_B T / 6\pi\eta_0 R$, and $H(q)$ is the hydrodynamic factor. This linear regime of the DSFs indicates that at short time, individual particles still diffuse freely without the influence from direct interaction with their neighbours. The change in limiting slope as $\tau \to 0$, or the short-time diffusion coefficient $D_s(q) =$

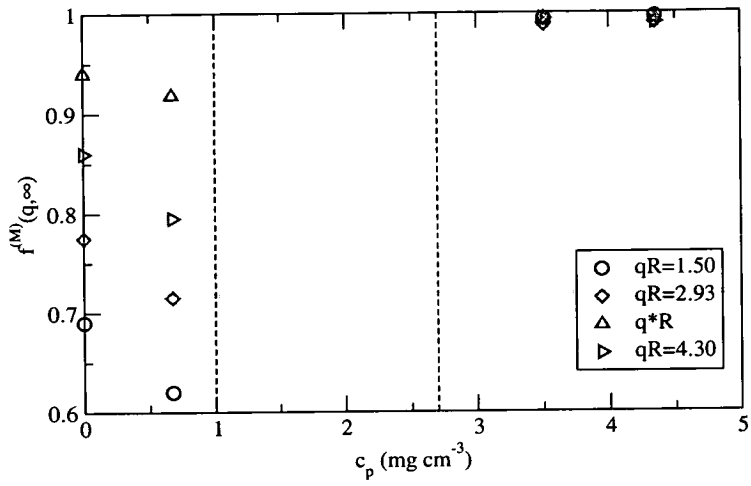

Figure 5.10: The measured non-ergodicity parameters, $f^{(M)}(q,\infty)$, at different wave vectors as a function of polymer concentration in samples (left to right) A, B, G, and H. The dashed lines indicate the glass transitions observed in Fig. 5.3.

$D_0H(q)/S(q)$, can be almost entirely explained by the change in $S(q)$ (Fig. 5.12), including the strong decrease on entering the attractive glass regime. What is more interesting is that the dynamics depart from free diffusion progressively earlier upon increasing attraction (Fig. 5.11). In fact, for the attractive glasses F–H, the particles are confined so tightly by the attractive potential wells that the DSFs display non-linearity almost immediately (cf. also insets to Figs. 5.7–5.9).

Moving to the (shorter) sequence of samples at the higher volume fraction of $\phi \approx 0.64$ and closer to the intersection of the two glass transition lines, samples I–K in Fig. 5.3, we see the emergence of remarkably stretched-out, extremely slow dynamics. Consider first the data at $qR = 1.50$, Fig. 5.13. In terms of short-time dynamics (inset, Fig. 5.13), samples I and J are comparable to samples C and D, while sample K shows a behaviour intermediate between those of samples E and F. At intermediate times, the decay is linear with respect to the logarithm of the scaled time. Thereafter there is an incipient plateau at $f \sim 0.7$ in sample I, reminiscent of the plateau in repulsive glasses A and B, before a further decay, but never beyond ~ 0.62 in my time window. There is no incipient plateau for the other two samples. Note that the DSF of sample I

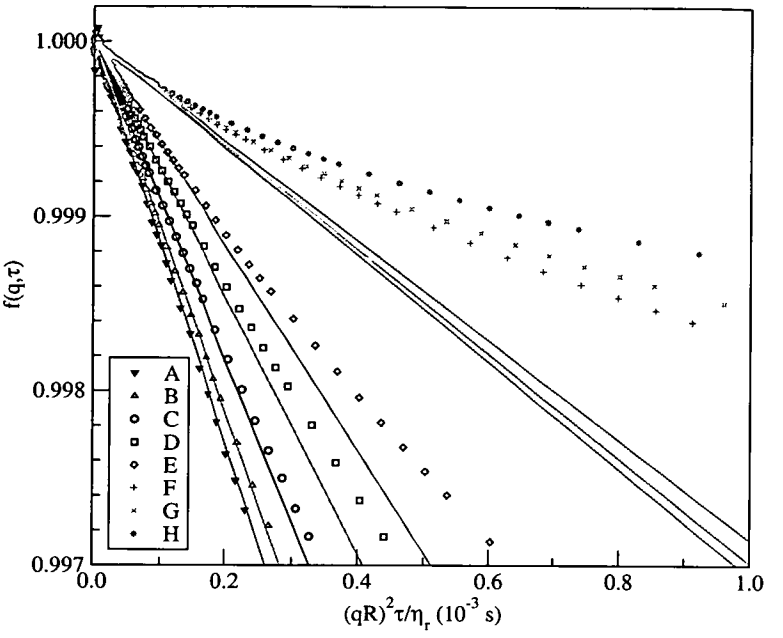

Figure 5.11: The short-time dynamics of samples A–H at $qR = 1.50$. The straight lines are fits to the linear part of the DSFs at $\tau \to 0$. The dynamics departs from an initial diffusive regime progressively earlier upon increasing attraction. The short-time diffusion coefficient in the limit $\tau \to 0$ is also reduced significantly.

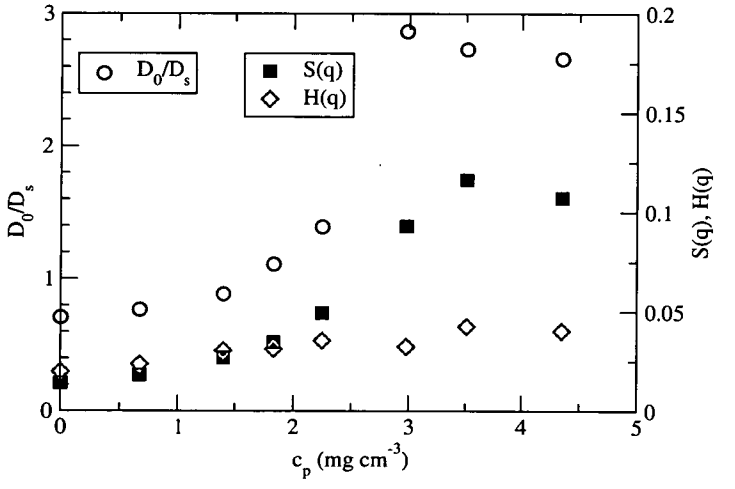

Figure 5.12: The normalized short-time diffusion coefficient D_0/D_s(circles, left scale), static structure factor $S(q)$ and hydrodynamic factor $H(q)$ (right scale) at $qR = 1.50$. D_s and $S(q)$ were extracted from Fig. 5.11 and 5.4 respectively. The decrease in D_s is nearly in line with the increase in $S(q)$ so that $H(q)$ only increased slightly.

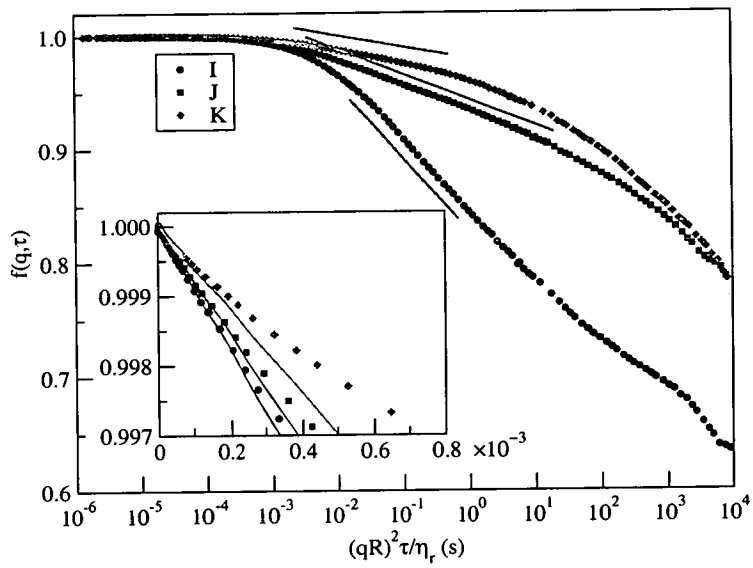

Figure 5.13: The DSFs at $qR = 1.50$ for samples I–K with $\phi \sim 0.64$. Extremely stretched relaxation is found in all three samples with logarithmic decay over long ranges of τ (straight lines). The inset shows the short-time dynamics, which deviate from the diffusive regime from very early times.

shows aspects of the behaviour of repulsion-dominated glasses (long time) and a fluid dominated by short-range attraction (short time). The two regimes are 'bridged' by a stretched log-time decay.

At the peak of the SSF, Fig. 5.14, sample I behaves in a similar way at short to intermediate times, while there is no incipient plateau at long times. Samples J and K develop an incipient plateau as high as ~ 0.993 (inset Fig. 5.14) before turning over to decay more rapidly in logarithmic time.

The fact that these samples show extremely stretched out dynamics, logarithmic in time, suggests that they are very close to the A3 critical point predicted by MCT, where the repulsive and attractive glasses become indistinguishable [36, 88, 89]. In particular, the shape of the DSF of sample I at $qR = 1.5$ is comparable to curve 3 in Fig. 11 of [36], calculated at $qR = 2.1$ for a sample on the repulsive glass transition line very close to where it intersects the attractive glass transition line for a system that just shows an A3 singularity. This is not inconsistent with the position of sample I on

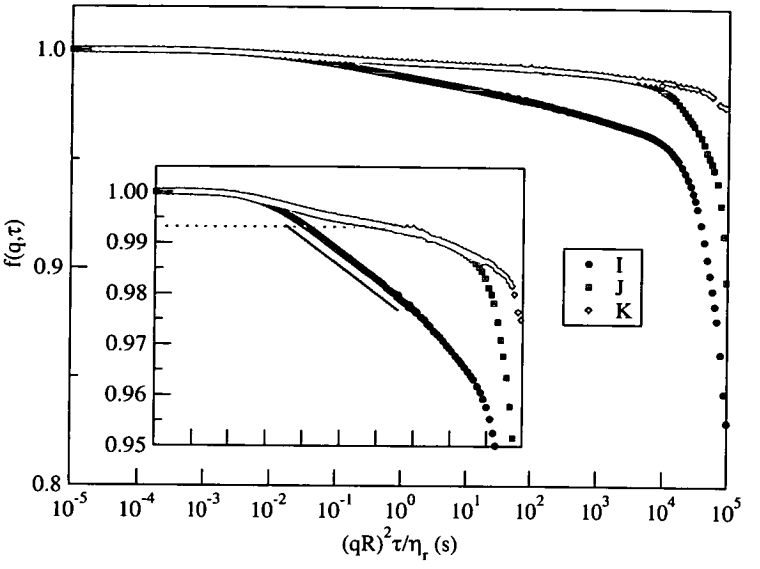

Figure 5.14: DSFs at the peak of the SSH for samples I–K. All decay much slower than at low q. Sample I shows a logarithmic decay for about 3 decades in scaled time. Samples J and K develop very high plateaus (inset).

the state diagram, Fig. 5.3, of this system at $\xi \approx 0.09$ [35].

Heuristically, we may begin to make sense of log-time decays as follows. At high enough volume fraction, the average distance between neighbouring particles will decrease to a value such that they are always well within the attraction range of each other [1]. If the attraction is strong enough, the restriction of particle movement due to the neighbour cage and the restriction caused by bonding between particles take place simultaneously at all times. This competition between two opposite mechanisms may lead to a broad distribution of decay times and therefore a very stretched out DSF [2].

[1] In this system the estimated distance between particles for samples I–K ($\phi = 0.64$) from random close pack ($\phi_{rcp} = 0.69$) is $(\phi_{rcp}/\phi)^{1/3} = 1.03 \sim 1 + \xi/3$, where the attractive potential is half of the maximum depth.

[2] Formally, a τ^{-1} distribution of decay times gives a decay linear in $\log \tau$. Limitations in my data mean, however, that I cannot use them to back out the actual decay-time distribution in our samples.

5.3.2 Constant compositions, variable scattering vectors

In this section, I show for completeness the dynamics of each sample at different scattering vectors in Figs. 5.15–5.18. The change of DSFs with q in repulsive glasses A and B are in agreement with previous work [85, 5]. Other samples show the general trend that the dynamics become slower at scattering vectors with higher $S(q)$. The only exception concerns the intermediate-time dynamics of the attractive glasses F–H (insets, Fig. 5.17). The significance of the rather complicated q-dependence of the intermediate-time dynamics of these samples is not clear. Nor do I know of any detailed calculations to date that can throw light on this issue.

The systematic q-dependent data shown in Figs. 5.15–5.18 allow me to investigate the q-dependence of the measured non-ergodicity parameter, $f^{(M)}(q, \infty)$, in detail. The measured non-ergodicity parameters of glassy samples A, B, G and H are shown as a function of scattering vector q in Fig. 5.19. The data for repulsive glasses A and B vary essentially with the static structure factor, as observed in hard-sphere glasses [85]. Attractive glass G and H on the other hand showed extremely high measured non-ergodicity parameters that hardly vary with q. This agrees with predictions by MCT (c.f. Fig. 8 in [36]).

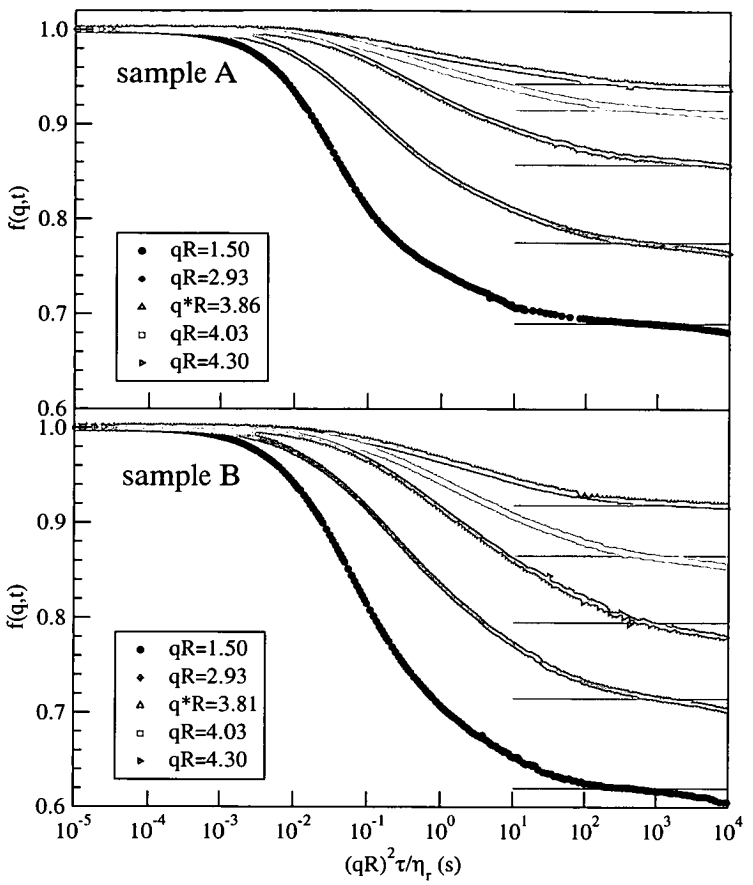

Figure 5.15: The DSFs of samples A and B at different q vectors, q^* denotes the peak position of the static structure factor $S(q)$. The general shape of the DSFs are very similar. Horizontal lines denotes the height of the plauteau (non-ergodicity parameters) that are plotted in Figs. 5.10 and 5.19.

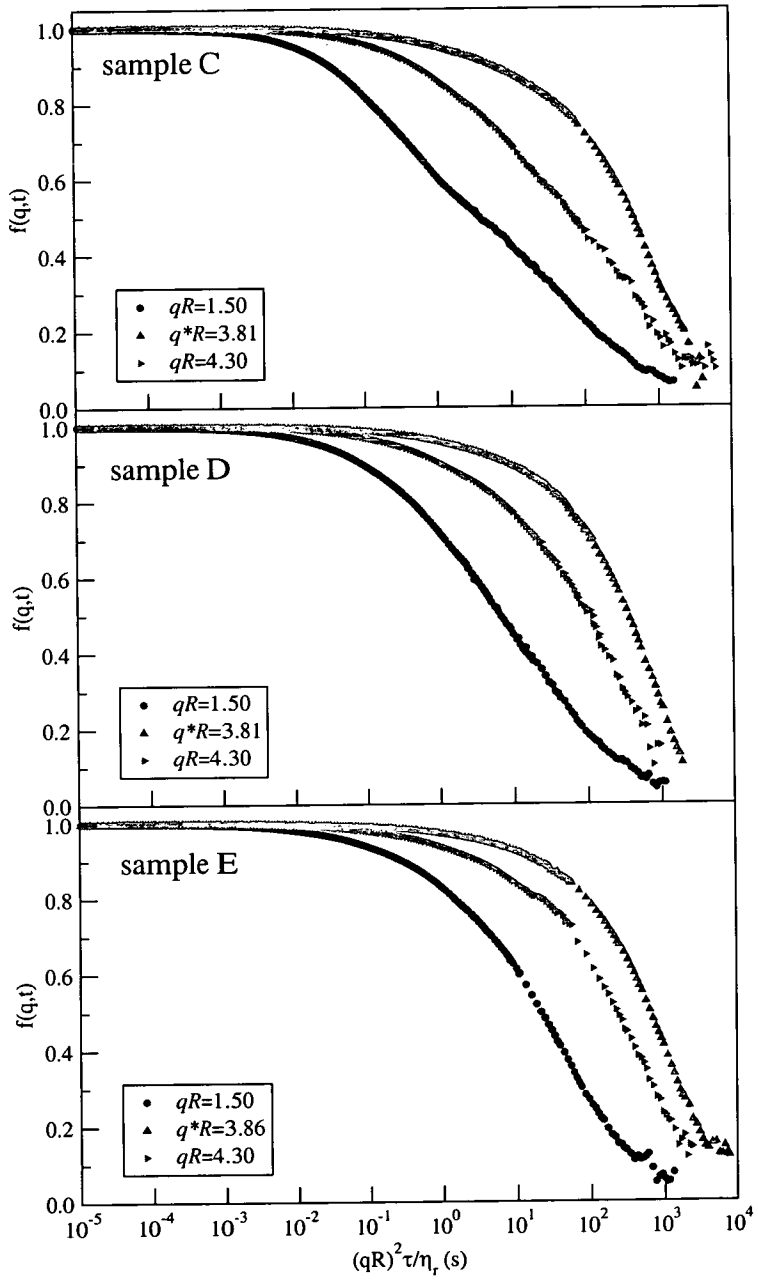

Figure 5.16: The DSFs of samples C–E at different q. The rate of decay varies in the opposite direction to $S(q)$ (c.f. Fig. 5.4). However, all decay to zero at approximately the same scaled time. Except for sample C at the lowest q, all other DSFs do not show two distinct relaxation processes as other dense fluids.

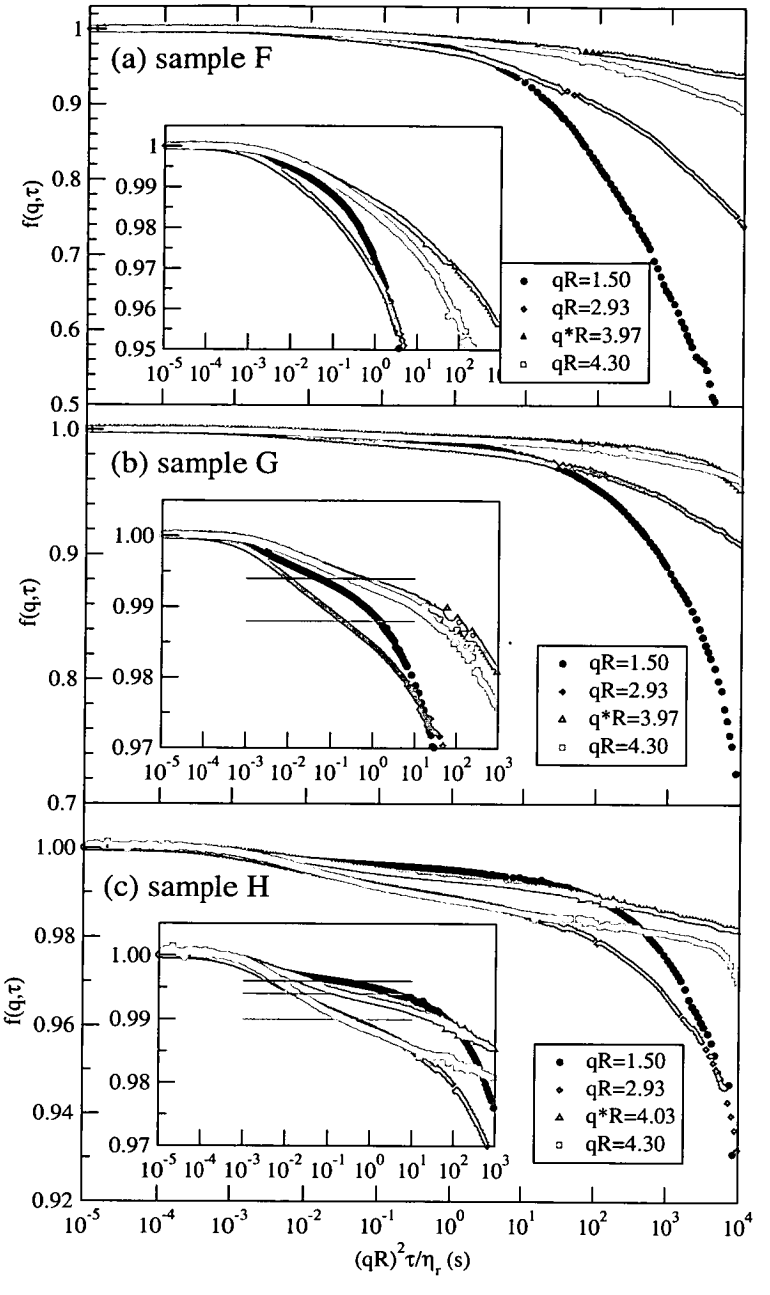

Figure 5.17: The DSFs of samples F–H at different q. The vertical axes span different ranges. Sample F did not show a point of inflection, but G and H have very high points of inflection (horizontal lines), the values of which are used in Figs. 5.10 and 5.19.

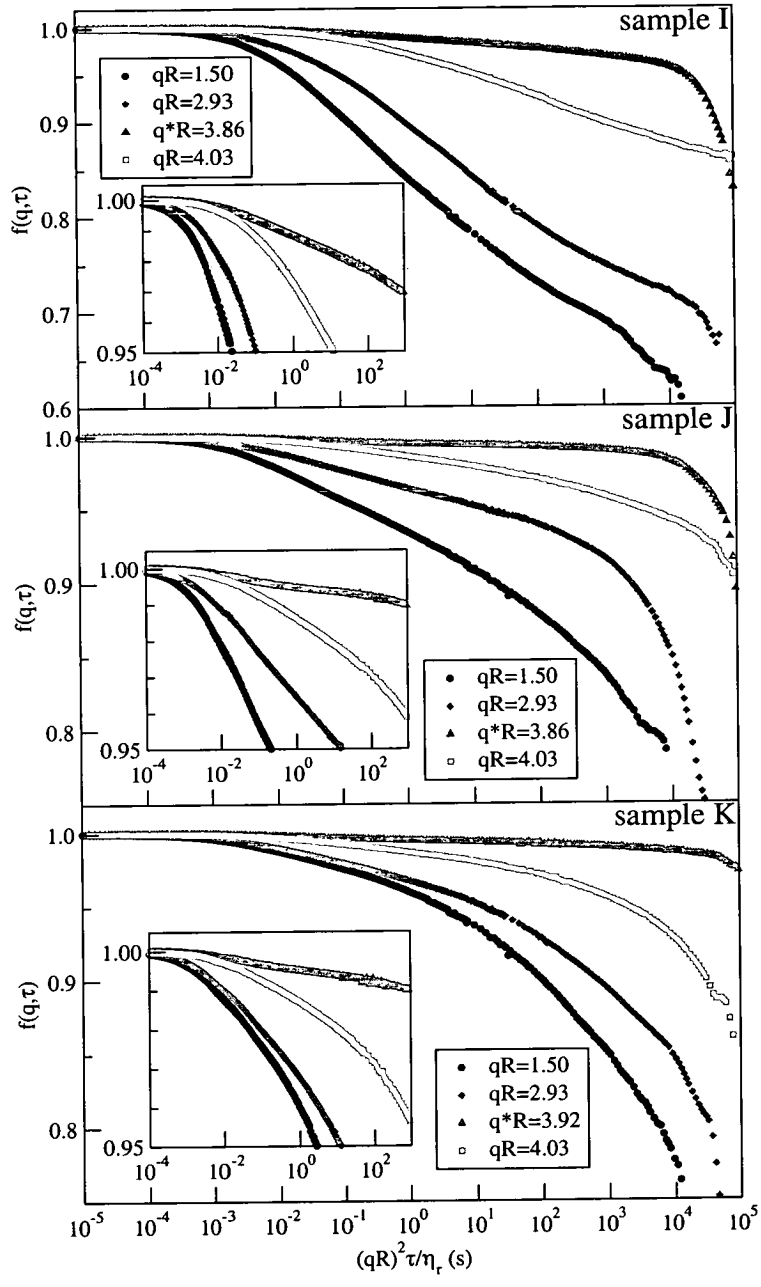

Figure 5.18: The DSFs of samples I, J and K at different q. The insets show the same quantities with expanded vertical axes. The relaxations show similar behaviour at all wave vectors except at the peak of $S(q)$. Sample I decays to a logarithmic section and then appears to turn up to a plateau. Sample J shows a very long section of logarithmic decay. Sample K is similar to J with a shorter stretch of logarithmic decay. In the early decay at the peak of $S(q)$, the DSF of sample I has a long stretch of logarithmic decay whereas samples J and K develop very high plateaus.

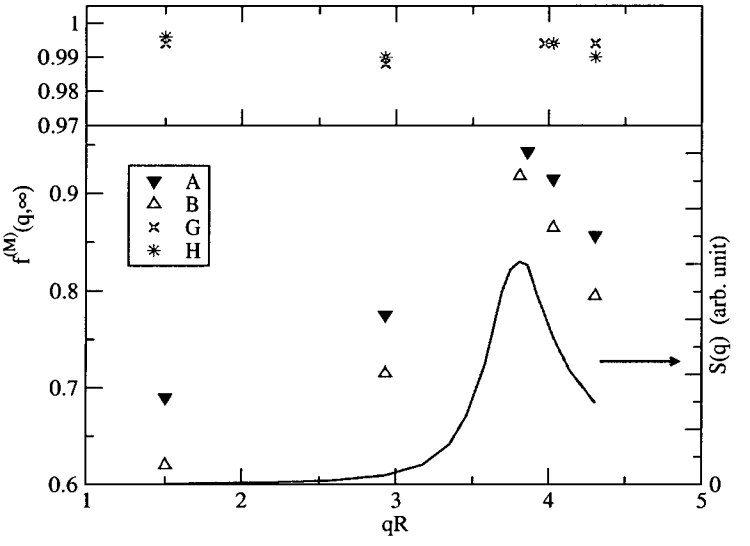

Figure 5.19: The measured non-ergodicity parameters of samples A, B, G and H as a function of scattering vector q (points), and the static structure factor of sample B (line) for comparison. The non-ergodicity parameters of repulsive glasses A and B follow the static structure factor, whereas those of the attractive glass are extremely high and hardly fluctuate with q (upper pane with expanded vertical axis).

Chapter 6

Conclusion

6.1 Summary of Results

In this work I have presented a detailed experimental investigation of the glass transitions in a colloid-polymer mixture with $\xi = 0.09$, a model for a hard-sphere system with short range attraction. Experimental methods include observation of phase behaviour and light scattering which explores the microscopic structure and dynamics of the system. I also presented the echo dynamic light scattering technique used to obtain ensemble-averages in DLS measurements.

6.1.1 Echo DLS

Echo DLS is a simple method of measuring ensemble-averaged correlation functions by rotating the sample in a dynamic light scattering setup. The correlation functions obtained consist of peaks (echoes) at delay time equal to exact multiples of the rotational period. The envelope of these echoes follows the ensemble-averaged correlation function of the sample obtained otherwise. Theoretical analysis and computer simulations predict the profiles of the echoes and show that their shape is not altered by

sample dynamics. Therefore correction to imperfect sample rotation can be made using the areas under the echoes. The echo DLS method requires only simple hardware to be added to any DLS setup, yet gives very good and quality-verifiable data over a delay time range $1 - 10^4$ seconds and beyond in a similar measurement time. It is ideal as a practical compliment to other methods for measuring long time dynamics of many classes of non-ergodic samples not least the glasses studied in this work.

6.1.2 Phase behaviour

The equilibrium phase behaviour of the system under study agreed with predictions by theory [19] and previous experiments [13]. It was also found that fluid-crystal coexisting samples at low volume fraction reached their final state via a two-step process: a gas-liquid separation followed by the crystallization of the liquid phase. This was attributed to the colloid size polydispersity which brought the fluid-crystal coexistence boundary closer to the gas-liquid binodal. The fractionation in the gas-liquid separation produced a less polydisperse liquid phase that finally crystallized.

Samples with high enough volume fraction and/or polymer concentration did not reach the predicted crystallized phases but stay amorphous for long periods of time. The positions of these samples on the phase diagram clearly showed a re-entrant behaviour: the attraction melted the hard-sphere-like *repulsive glass* and pushed the glass transition to a higher volume fraction. However, with strong enough attration, the system was stuck in an *attractive glass*. The microscopic structure and dynamics of these glasses were then explored with light scattering.

6.1.3 Structure and dynamics of glasses

It was found that in increasing attraction across the re-entrant region, the structure of the system changes gradually. Locally particles are drawn closer together thus create

more heterogeneity at longer length scale. As soon as the system enters the attractive glass, neighbouring particles are almost touching and the structural changes seem to saturate.

On the other hand, the collective particle dynamics studied by DLS reveals a clear re-entrant glass transition. With little attraction, the system at high enough volume fraction is 'stuck' in a repulsive glassy state where the arrest is due to caging by neighboring particles. My data support the suggestion [39] that attraction causes particles to cluster, thus opening up holes in the cages and melting the glass. At the same time, the attraction slows down the particle dynamics. It was found that the repulsive glass melts when the characteristic time of the attraction-dominated particle dynamics becomes comparable to that of cage opening. The resulting ergodic fluid shows a distinctive dynamical feature: despite the fluid's high density, its DSF does not show distinct α and β relaxation processes.

Increasing the attraction further leads to a different kind of arrest where the strong attraction between particles creates long-lived bonds and prevents structural rearrangement, giving rise to an attraction-dominated glass. These short-range bonds manifested in the dynamic structure factors as 'points of inflection' much higher than the plateaus of repulsive glass.

In the region where the two glass transition lines are expected to meet, I observed very slow, log-time dynamics in the DSFs. These stretched dynamics which correspond to broad distribution of decay times could be the result of a competition between two opposite mechanisms of glass forming: caging and bonding. The observed dynamics agree well with predictions for samples near the critical 'A3' point in mode-coupling theory.

6.2 Suggestions for future work

6.2.1 Comparison with MCT

Qualitatively, the scenario of two types of fundamentally different glasses agrees well with predictions from MCT calculations (with those reported in [35] being closest to the present experimental system). Quantitatively, however, these results stand as a challenge to MCT (or any other theory): the detailed calculations needed for direct quantitative comparison have not, to my knowledge, been performed.

A detailed comparison between experiment and theory faces a number of non-trivial problems. First and foremost, since calculated and measured glass transition thresholds differ, choices exist as to what constitute 'corresponding state points' for the purpose of making the comparison. In the case of pure hard spheres, where $\phi_g^{\mathrm{MCT}} \approx 0.52$ and $\phi_g^{\mathrm{expt}} \approx 0.58$, it is accepted practice to compare measurements and calculations at the same relative volume fraction $(\phi - \phi_g)/\phi_g$ [5]. The situation is more complex in a colloid-polymer mixture, since a state point is now specified by the densities of both components. The predicted glass transition lines show quantitative disagreement with experiments over the whole composition plane (cf. Fig. 1 in [37]). To compare calculated and measured SSFs and DSFs, a protocol for identifying 'corresponding state points' is needed.

Secondly, the attractive interaction between two particles is always specified directly as a potential energy in calculations. The corresponding experimental variable is the polymer concentration in the free volume, c_p^{free}. This is currently guessed at using an uncontrolled and untested approximation based on scaled-particle theory [19], and is likely to lead to large systematic errors in systems with high colloid volume fractions.

Finally, the marked and complex aging behaviour of the attractive glasses complicates the definition of a non-ergodic state for the purposes of comparing with MCT. Despite these potential difficulties, however, my data suggest that it may be worthwhile

performing a series of calculations at fixed ϕ and increasing attraction crossing the re-entrant gap in between the repulsive and attractive glass transition lines for a system of hard spheres interacting with something like an Asakura-Oosawa potential [35].

6.2.2 Aging in glasses

It is clear from my preliminary study that attractive and repulsive glasses show qualitative different aging behaviour. Classical MCT does not predict aging, but it is a generic feature of experimental glasses of all kinds [84]. One could speculate that aging is the slow process of exploring neighbouring energy landscape minima via activated hopping. It thus provides another window to look at the nature of the two glasses. A number of theoretical approaches are emerging, and simulation is a valuable tool. It is possible that the activated processes seen in simulations [90] are responsible for the final decays of the dynamics in our attractive glasses and their aging behaviour, ultimately avoiding the ideal MCT divergence of relaxation time. It is probable that further study of this phenomenon in this model colloid-polymer mixture should throw significant light on this intriguing (and generic) phenomenon.

6.2.3 Fragile and strong glasses

It was suggested [69] that the two glassy states found in attractive hard spheres could be seen in the context of fragile and strong glass former in atomic and molecular glasses. They are classified according to the way the viscosity diverges as the glass transition is approached from the liquid side [7]. The viscosity of strong glass formers diverges according to an Arrhenius law (i.e. exponentially), while that of fragile glass formers does not. Hard sphere glass are then fragile. One may speculate that attraction-dominated glasses are 'strong' in this sense — because there is an energy scale (set by the attractive well depth), we may expect an 'activated' (i.e. Arrhenius) viscosity.

Further studies of the rheology of the two glassy states studied here will either confirm or dismiss this scenario. Strong and fragile glasses can also be distinguished by their underlying 'energy landscapes' [91], which could be studied by direct imaging.

6.2.4 Other approaches

MCT has been found to be successful in predicting many features of the glass transition in hard spheres without as well as with a short-range attraction. Much of the physical basis for its success, however, remains to be elucidated. Some features, like aging and hydrodynamic interaction were completely ignored by classical MCT. It is possible to study this system in other theoretical approaches which have been less used to discuss colloidal glasses to date.

Some of these may give insight into the glassy states found in this work. Energy landscapes [91] with relation to fragile-strong glasses and aging have already been alluded to. This approach is somewhat related to the random trap model [92]. The melting of a repulsive glass by adding attraction may be discussed in terms of 'free volume' [93]. The local environment of each particles, essential to these approaches, can be deduced from direct imaging.

Appendix A

Theoretical polydisperse fluid-crystal phase diagram

This appendix describes detailed procedures to calculate the polydisperse fluid-crystal coexistence boundary. Details of the equilibrium theory that these calculations are based on can be found in [19, 20]. The free energy of a polydisperse crystal phase based on cell theory is taken from [81].

A.1 Free energies

As discussed in section 2.1.2, the dimensionless free energy concentration $h(\phi)$ is used to derive the colloid chemical potential and osmotic pressure in each phase (Eqs. 2.10 and 2.11). It consists of two parts, a colloidal term and a polymer term (Eq. 2.9):

$$h(\phi) = \frac{F_c}{k_B T}\frac{4\pi R^3}{3V} - n_p^{\text{free}}\alpha(\phi)\frac{4\pi R^3}{3} \,. \tag{A.1}$$

Let us define the *free polymer volume fraction* $a_p = (4/3)\pi r_g^3 N_p/(\alpha V)$. Note that this is not the *polymer activity* mentioned in [20]. The free polymer number concentration

n_p^{free} can be expressed in terms of the dimensionless a_p in the above equation:

$$h(\phi) = \underbrace{\frac{F_c}{k_BT}\frac{4\pi R^3}{3V}}_{h_c(\phi)} \underbrace{-\frac{a_p\alpha(\phi)}{\xi^3}}_{h_p(\phi,a_p)} . \tag{A.2}$$

The second term depends only on free polymer concentration, i.e. on a_p, and colloid volume fraction ϕ. The first term is the colloid term and can be derived from the appropriate equation of state for hard sphere colloids.

Hard sphere colloid equation of states are usually expressed as a function of compressibilty in volume fraction: $Z \equiv PV/(N_c k_B T) = Z(\phi)$. The free energy density due to colloid $h_c(\phi)$ is derived from the equation of states as follow.

$$\frac{F_c}{N_c k_B T} = \int \frac{Z(\phi)}{\phi} d\phi + C \tag{A.3}$$

$$\frac{F_c}{V k_B T} = \frac{N_c}{V}\left(\int \frac{Z(\phi)}{\phi} d\phi + C\right) \tag{A.4}$$

$$\frac{F_c}{V}\frac{4\pi R^3}{3k_BT} = \frac{4\pi R^3 N_c}{3V}\left(\int \frac{Z(\phi)}{\phi} d\phi + C\right) \tag{A.5}$$

$$h_c(\phi) = \phi\left(\int \frac{Z(\phi)}{\phi} d\phi + C\right) , \tag{A.6}$$

where C is an arbitrary integration constant.

For the fluid phase, the compressiblity expression by Carnahan and Starling (Eq. 1 in [94])

$$Z(\phi) = \frac{1+\phi+\phi^2-\phi^3}{(1-\phi)^3} \tag{A.7}$$

was used to obtain $h_c(\phi)$:

$$h_c^f(\phi) = \phi\left(\ln(\phi) - 1 + \frac{\phi(4-3\phi)}{(1-\phi)^2}\right) , \tag{A.8}$$

with an implicit value of C taken as a reference.

For the polydisperse colloidal crystal, the free energy based on a cell theory suggested by Sear [81] gives:

$$h_c^x(\phi) = \phi\left(C - 3\int_0^\infty p(R)\ln(a-(R+\overline{R}))\right) , \tag{A.9}$$

where a is the nearest neighbour distance in a FCC lattice, $a = 2\overline{R}\left(\frac{\phi_{FCC}}{\phi}\right)^{1/3}$, and $p(R)$ is the size distribution function for a polydisperse system.

In the limit of a monodisperse system, $p(R) = \delta(R - \overline{R})$, the colloid free energy becomes:

$$h^x_{c0}(\phi) = \phi\left(C - 3\ln(a - 2\overline{R})\right) \tag{A.10}$$

For a polydisperse system, I used the "hat" distribution function for colloidal size, ie. for a system with polydispersity σ,

$$p(r) = \begin{cases} 0 & r < \overline{r}(1-\sigma) \\ \frac{1}{2\sigma} & \overline{r}(1-\sigma) < r < \overline{r}(1+\sigma) \\ 0 & r > \overline{r}(1-\sigma) \end{cases} . \tag{A.11}$$

With this form of size distribution function, the free energy density for polydisperse systems is (taken $\overline{R} = 1$)

$$h^x_{c\sigma}(\phi) = \phi\left(\frac{3}{2\sigma}\left((a-2-\sigma)\ln(a-2-\sigma) - (a-2+\sigma)\ln(a-2+\sigma)\right) + 3 + C\right) \tag{A.12}$$

Note that the expressions of $h^x_c(\phi)$ in Eqs. A.10 and A.12 are kept so that the constant C is the same as in Eq. A.9. The value of C will be adjusted in the phase boundary calculation for the monodisperse case (Eq. A.10) so that the coexisting *hard sphere* fluid and crystal volume fraction is *as close as possible* to 0.494 and 0.545. A perfect match is not possible due to the accuracy of the cell model.

A.2 Phase boundary calculation

Substituting the expressions of $h^f_c(\phi)$ and $h^x_c(\phi)$ for colloidal fluid and crystal respectively to Eq. A.2, one obtains two free energy density functions $h_f(\phi)$ and $h_x(\phi)$ for fluid and crystal phases in colloid-polymer mixture with a_p as a parameter. It can

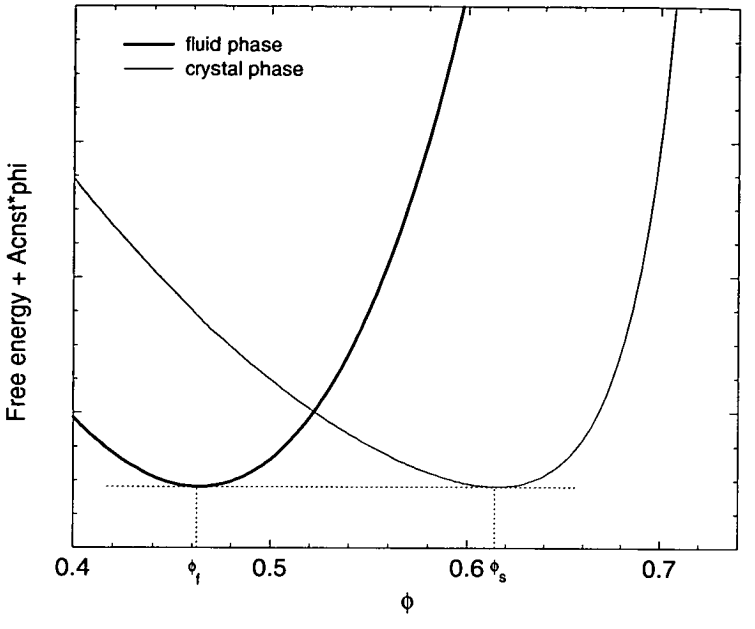

Figure A.1: Common tangent method used to calculate the volume fractions of coexisting phases. Both $h(\phi)$ curves for fluid and solid are progressively added a linear term $A\phi$ until both minima are equal. The values of ϕ at the minima are the coexisting volume fractions.

be shown that the colloid chemical potential and osmotic pressure are the slope and intercept of the tangent to $h(\phi)$ (Eqs. 2.10 and 2.11).

Therefore the coexisting volume fractions of fluid and crystal are the contact points of a common tangent to $h_c^f(\phi)$ and $h_c^x(\phi)$. It should also be noted that adding a linear term $A\phi$ to *both curves* (after calibrating the integration constant C one against the other) does not change the ϕ coordinates of the tangential points of the common tangent to the 2 curves. Therefore it is easier to calculate the common tangent by progressively adding $A\phi$ with varying A until both minima of the curves are on the same horizontal tangent (Fig. A.1). The results of coexisting volume fractions for different values of a_p are collected to construct the thoeretical phase diagram in the (a_p, ϕ) plane. The corresponding phasediagram in experimental space (c_p, ϕ) is calculated by converting a_p to c_p using the corresponding ϕ of each phase.

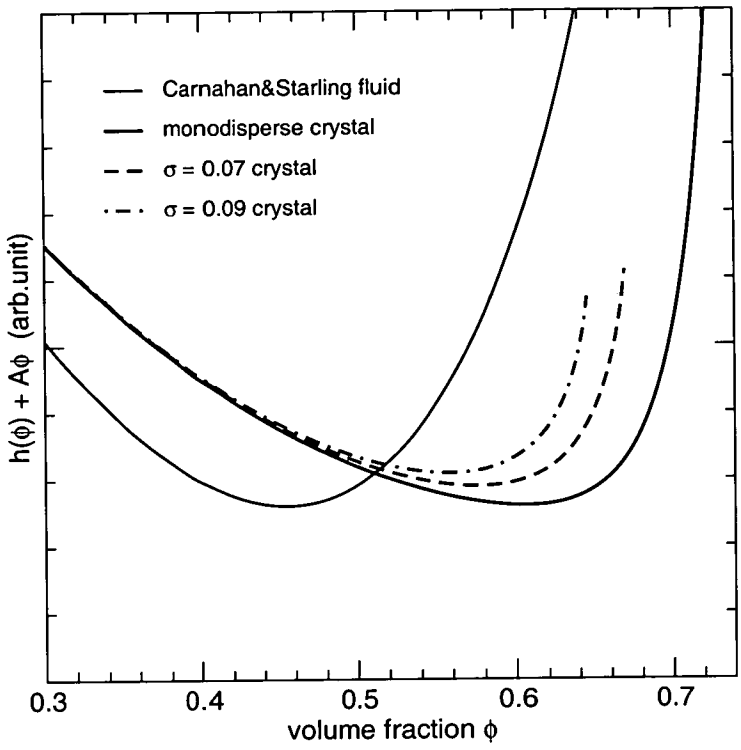

Figure A.2: Free energy density of fluid phase (thin line) and crystal phase (thick lines) of diferrent polydispersities calculated with a top hat size distribution in the cell model: monodisperse limit (continuous line), $\sigma = 7\%$ (dash line), $\sigma = 9\%$ (dot-dash line). The same arbitrary linear term of ϕ was added to all the curves. The common tangent to fluid and crystal free energy branches determines volume fractions of coexisting phases.

The effect of polydispersity is to increase the crystal free energy (Fig. A.2). This makes the coexisting volume fractions of fluid and crystal closer, resulting in a narrower fluid-crystal coexistence region as seen in Fig. 5.2.

Bibliography

[1] P. N. Pusey and W. van Megen. Phase-behavior of concentrated suspensions of nearly hard colloid spheres. *Nature*, 320(6060):340–342, 1986.

[2] P. N. Pusey and W. van Megen. Observation of a glass transition in suspensions of spherical colloidal particles. *Phys. Rev. Lett.*, 59(18):2083–2086, 1987.

[3] W. G. Hoover and F. H. Ree. *J. Chem. Phys.*, 49:3609, 1968.

[4] C. A. Angell, J. H. R. Clarke, and L. V. Woodcock. *Adv. Chem. Phys.*, 48:397–453, 1981.

[5] W. van Megen and S. M. Underwood. Glass-transition in colloidal hard spheres - measurement and mode-coupling-theory analysis of the coherent intermediate scattering function. *Phys. Rev. E*, 49(5):4206–4220, 1994.

[6] E. R. Weeks, J. C. Crocker, A. C. Levitt, A. Schofield, and D. A. Weitz. Three-dimensional direct imaging of structural relaxation near the colloidal glass transition. *Science*, 287(5453):627–631, Jan 2000.

[7] C. A. Angell. Formation of glasses from liquids and biopolymers. *Science*, 267(5206):1924–1935, 1995.

[8] P. Calvert. Material sciences - a spongy way to new ceramics. *Nature*, 317(6034):201–201, 1985.

[9] Andreas Stein and Rick C. Schroden. Colloidal crystal templating of three-dimensionally ordered macroporous solids: materials for photonics and beyond. *Current Opinion in Solid State & Materials Science*, 5(6):553–564, 2001.

[10] S. Asakura and F. Oosawa. *J. Chem. Phys.*, 22:1255, 1954.

[11] D. Rudhardt, C. Bechinger, and P. Leiderer. Direct measurement of depletion potentials in mixtures of colloids and nonionic polymers. *Phys. Rev. Lett.*, 81(6):1330–1333, 1998.

[12] W. C. K. Poon. The physics of a model colloid-polymer mixture. *J. Phys.: Condens. Matter*, 14(33):R859–R880, 2002.

[13] S. M. Ilett, A. Orrock, W. C. K. Poon, and P. N. Pusey. Phase-behavior of a model colloid-polymer mixture. *Phys. Rev. E*, 51(2):1344–1352, 1995.

[14] W. C. K. Poon, A. D. Pirie, and P. N. Pusey. Gelation in colloid-polymer mixtures. *Faraday Discuss.*, 101:65–76, 1995.

[15] W. C. K. Poon, J. S. Selfe, M. B. Robertson, S. M. Ilett, A. D. Pirie, and P. N. Pusey. An experimental study of a model colloid-polymer mixture. *J. Phys. II (France)*, 3(7):1075–1086, 1993.

[16] D. M. Shotton. Electronic light-microscopy - present capabilities and future-prospects. *Histochemistry and cell biology*, 104(2):97–137, 1995.

[17] Eric R. Weeks and D. A. Weitz. Properties of cage rearrangements observed near the colloidal glass transition. *Phys. Rev. Lett.*, 89(9):095704, 2002.

[18] Y. N. Ohshima, H. Sakagami, K. Okumoto, A. Tokoyoda, T. Igarashi, K. B. Shintaku, S. Toride, H. Sekino, K. Kabuto, and I. Nishio. Direct measurement of infinitesimal depletion force in a colloid-polymer mixture by laser radiation pressure. *Phys. Rev. Lett.*, 78(20):3963–3966, 1997.

[19] H. N. W. Lekkerkerker, W. C. K. Poon, P. N. Pusey, A. Stroobants, and P. B. Warren. Phase-behavior of colloid plus polymer mixtures. *Europhys. Lett.*, 20(6):559–564, 1992.

[20] P. B. Warren, S. M. Ilett, and W. C. K. Poon. Effect of polymer nonideality in a colloid-polymer mixture. *Phys. Rev. E*, 52(5):5205–5213, Nov 1995.

[21] Evert Jan Meijer and Daan Frenkel. Colloids dispersed in polymer solutions. a computer simulation study. *J. Chem. Phys.*, 100(9):6873–6887, 1994.

[22] W. C. K. Poon, L. Starrs, S. P. Meeker, A. Moussaid, R. M. L. Evans, P. N. Pusey, and M. M. Robins. Delayed sedimentation of transient gels in colloid-polymer mixtures: dark-field observation, rheology and dynamic light scattering studies. *Faraday Discuss.*, 112:143–154, 1999.

[23] Wolfgang Götze. Recent tests of the mode-coupling theory for glassy dynamics. *J. Phys: Condens. Matter*, 11(10A):A1–A45, 1999.

[24] M. E. Cates. Arrest and flow of colloidal glasses. In D. Iagolnitzer, V. Rivasseau, and J. Zinn-Justin, editors, *Proceedings of the International Congress on Theoretical Physics*. Birkhäuser, 2002.

[25] W. Götze and L. Sjogren. Relaxation processes in supercooled liquids. *Rep. Prog. Phys.*, 55(3):241–376, 1992.

[26] W. Götze. In J.-P. Hansen, D. Levesque, and J. Zinn-Justin, editors, *Liquids, Freezing and Glass Transition*, Les Houches Summer Schools of Theoretical Physics, pages 287–503. North Holland, Amsterdam, 1989.

[27] J. K. G. Dhont. *An introduction to Dynamics of Colloids*. Studies in Interface Science. Elsevier, Amsterdam, 1996.

[28] P. N. Pusey. Colloidal suspensions. In J.-P. Hansen, D. Levesque, and J. Zinn-Justin, editors, *Liquids, Freezing and the Glass Transition*, chapter 10, pages 764–942. Elsevier, Amsterdam, 1991.

[29] W. Hess and R. Klein. Long-time versus short-time behaviour of a system of interacting brownian particles. *J. Phys. A: Math. Gen.*, 13(1):L5–L10, 1983.

[30] Bruce J. Berne. Projection operator technique in the theory of fluctuations. In B. Berne, editor, *Statistical Mechanics, Part B: time-dependent processes*, pages 233–257. Plenum Press, 1977.

[31] W. Götze and M. Sperl. Logarithmic relaxation in glass-forming systems. *Phys. Rev. E*, 66(1):011405, 2002.

[32] Kyozi Kawasaki and Bongsoo Kim. A dynamic mean-field glass model with reversible mode coupling and a trivial hamiltonian. *J. Phys: Condens. Matter*, 14(9):2265–2273, 2002.

[33] U. Bengtzelius, W. Götze, and A. Sjölander. Dynamics of supercooled liquids and the glass transition. *J. Phys. C*, 17(33):5915–5934, 1984.

[34] Matthias Sperl. Dynamics in colloidal liquids near a crossing of glass- and gel-transition lines. preprint, cond-mat/0308425.

[35] J. Bergenholtz, W. C. K. Poon, and M. Fuchs. Gelation in model colloid-polymer mixtures. *Langmuir*, 19(10):4493–4503, 2003.

[36] K. Dawson, G. Foffi, M. Fuchs, W. Götze, F. Sciortino, M. Sperl, P. Tartaglia, Th. Voigtmann, and E. Zaccarelli. Higher-order glass-transition singularities in colloidal systems with attractive interactions. *Phys. Rev. E*, 63(1):011401, 2001.

[37] K. N. Pham, A. M. Puertas, J. Bergenholtz, S. U. Egelhaaf, A. Moussaïd, P. N. Pusey, A. B. Schofield, M. E. Cates, M. Fuchs, and W. C. K. Poon. Multiple glassy states in a simple model system. *Science*, 296(5565):104–106, 2002.

[38] M. Sperl. Dynamics in colloidal liquids near a crossing of glass- and gel- transition lines, 2003. preprint cond-mat/0308425.

[39] J. Bergenholtz and M. Fuchs. Nonergodicity transitions in colloidal suspensions with attractive interactions. *Phys. Rev. E*, 59(5):5706–5715, 1999.

[40] F. Mallamace, P. Gambadauro, N. Micali, P. Tartaglia, C. Liao, and S.-H. Chen. Kinetic glass transition in a micellar system with short-range attractive interaction. *Phys. Rev. Lett.*, 84(23):5431–5434, 2000.

[41] T. Eckert and E. Bartsch. Re-entrant glass transition in a colloid-polymer mixture with depletion attractions. *Phys. Rev. Lett.*, 89(12):125701, 2002.

[42] T. Eckert and E. Bartsch. The effect of free polymer on the interactions and the glass transition dynamics of microgel colloids. *Faraday Discuss.*, 123:51–64, 2003.

[43] A. Puertas, M. Fuchs, and M. E. Cates. Comparative simulation study of colloidal gels and glasses. *Phys. Rev. Lett.*, 88(9):098301, 2002.

[44] J.-P. Hansen and I. R. McDonald. *Theory of Simple Liquids*. Academic Press, London, 2nd edition, 1986.

[45] Loup Verlet and Jean-Jacques Weis. Equilibrium theory of simple liquids. *Phys. Rev. A*, 5(2):939–952, 1972.

[46] J. Bergenholtz, M. Fuchsn, and T. Voigtmann. Colloidal gelation and nonergodicity transitions. *J. Phys.: Condens. Matter*, 12(29):6575–6583, 2000.

[47] J. Bergenholtz and M. Fuchs. Gel transitions in colloidal suspensions. *J. Phys.: Condens. Matter*, 11(50):10171–10182, 1999.

[48] Peter N. Pusey. Dynamic light scattering. In P. Lindner and Th. Zemb, editors, *Neutrons, X-rays and Light: Scattering Methods Applied to Soft Condensed Matter*, chapter 9, pages 203–220. North-Holland, 2002.

[49] P. N. Pusey and W. van Megen. Dynamic light-scattering by non-ergodic media. *Physica A*, 157(2):705–741, 1989.

[50] Klaus Schätzel. Supression of multiple scattering by photon cross-correlation techniques. *J. Mod. Optics*, 38(9):1849–1865, 1991.

[51] P. N. Segrè, W. van Megen, P. N. Pusey, K. Schätzel, and W. Peters. 2-color dynamic light-scattering. *J. Mod. Optics*, 42(9):1929–1952, 1995.

[52] A. Moussaïd and P. N. Pusey. Multiple scattering suppression in static light scattering by cross-correlation spectroscopy. *Phys. Rev. E*, 60(5):5670–5676, 1999.

[53] L. Cipelletti and L. Ramos. Slow dynamics in glasses, gels and foams. *Curr. Opin. Colloid Interface Sci.*, 7(3–4):228–234, 2002.

[54] W. van Megen, T. C. Mortensen, S. R. Williams, and J. Müller. Measurement of the self-intermediate scattering function of suspensions of hard spherical particles near the glass transition. *Phys. Rev. E*, 58(5):6073–6085, 1998.

[55] L. Cipelletti, S. Manley, R. C. Ball, and D. A. Weitz. Universal aging features in the restructuring of fractal colloidal gels. *Phys. Rev. Lett.*, 84(10):2275–2278, 2000.

[56] L. Ramos and L. Cipelletti. Ultraslow dynamics and stress relaxation in the aging of a soft glassy system. *Phys. Rev. Lett.*, 87(24):245503, 2001.

[57] M. Bellour, A. Knaebel, J. L. Harden, F. Lequeux, , and J.-P. Munch. Aging processes and scale dependence in soft glassy colloidal suspensions. *Phys. Rev. E*, 67(3):031405, 2003.

[58] J. Török, S. Krishnamurthy, J. Kertész, and S. Roux. Self-organization, localization of shear bands, and aging in loose granular materials. *Phys. Rev. Lett.*, 84(17):3851–3854, 2000.

[59] J. Török, S. Krishnamurthy, J. Kertész, and S. Roux. Slow relaxation due to optimization and restructuring: Solution on a hierarchical lattice. *Phys. Rev. E*, 67(2):026108, 2003.

[60] E. Overbeck, C. Sinn, T. Palberg, and K. Schätzel. Probing dynamics of dense suspensions: Three-dimensional cross-correlation technique. *Colloid. Surface. A*, 122(1–3):83–87, 1997.

[61] A. P. Y. Wong and P. Wiltzius. Dynamic light-scattering with a ccd camera. *Rev. Sci. Instrum.*, 64(9):2547–2549, 1993.

[62] L. Cipelletti and D. A. Weitz. Ultralow-angle dynamic light scattering with a charge coupled device camera based multispeckle, multitau correlator. *Rev. Sci. Instrum.*, 70(8):3214–3221, 1999.

[63] S. Kirsch, V. Frenz, W. Schartl, E. Bartsch, and H. Sillescu. Multispeckle autocorrelation spectroscopy and its application to the investigation of ultraslow dynamical processes. *J. Chem. Phys.*, 104(4):1758–1761, 1996.

[64] P. Hébraud, F. Lequeux, and J. P. Munch. Yielding and rearrangements in disordered emulsions. *Phys. Rev. Lett.*, 78(24):4657–4660, 1997.

[65] J. Müller and T. Palberg. Probing slow fluctuations in nonergodic systems: Interleaved sampling technique. *Progr. Colloid Polym. Sci.*, 100:121–126, 1996.

[66] K. Schätzel, M. Drewel, and S. Stimac. Photon-correlation measurement at large lag times: improving statistical accuracy. *J. Mod. Optics*, 35(4):711–718, 1988.

[67] K. Schätzel. New concepts in correlator design. *Inst. Phys. Conf. Ser.*, 77:175, 1985.

[68] Klaus Schätzel. Laser light scattering review. In *NASA Laser Light Scattering Advanced Technology Development Workshop*, 1988.

[69] W. C. K. Poon, K. N. Pham, S. U. Egelhaaf, and P. N. Pusey. 'unsticking' a colloidal glass, and sticking it again. *J. Phys.: Condens. Matter*, 15(1):S269–S275, 2003.

[70] L. Antl, J. W. Goodwin, R. D. Hill, R. H. Ottewill, S. M. Owens, S. Papworth, and J. W. Waters. The preparation of poly(methyl methacrylate) lattices in non-aqueous media. *Colloids Surf.*, 17(1):67–78, 1986.

[71] S. Auer, W. C. K. Poon, and D. Frenkel. Phase behavior and crystallization kinetics of poly-12-hydroxystearic-coated polymethylmethacrylate colloids. *Phys. Rev. E*, 67(2):020401, 2003.

[72] P. N. Pusey and W. van Megen. Detection of small polydispersities by photon-correlation spectroscopy. *J. Chem. Phys.*, 80(8):3513–3520, 1984.

[73] S. E. Paulin and Bruce J. Ackerson. Observation of a phase transition in the sedimentation velocity of hard spheres. *Phys. Rev. Lett.*, 64(22):2663–2666, 1990.

[74] G. C. Berry. Thermodynamic and conformational properties of polystyrene. i. light-scattering studies on dilute solutions of linear polystyrenes. *J. Chem. Phys.*, 44(12):4550–4564, 1966.

[75] Peter G. Bolhuis and David A. Kofke. Monte carlo study of freezing of polydisperse hard spheres. *Phys. Rev. E*, 54(1):634–643, 1996.

[76] Paul Bartlett. A geometrically-based mean-field theory of polydisperse hard-sphere mixtures. *J. Chem. Phys.*, 107(1):188–196, 1997.

[77] Paul Michael Golz. *Dynamics of Colloids in Polymer Solutions*. PhD thesis, University of Edinburgh, 1999.

[78] M. Stickler and N. Sütterlin. Concentration dependence of the viscosity of dilute polymer solutions: Huggins and schulz-blaschke coefficients. In J. Brandup and E. H. Immergut, editors, *Polymer Handbook*, pages VII/183–202. John Wiley & Sons, 1989.

[79] David John Fairhurst. *Polydispersity in Colloidal Phase Transitions*. PhD thesis, University of Edinburgh, 1999.

[80] P. N. Pusey. The effect of polydispersity on the crystallization of hard spherical colloids. *J. Physique*, 48(5):709–712, 1987.

[81] R. Sear. Phase separation and crystallisation of polydisperse hard spheres. *Europhys. Lett.*, 44(4):531–535, 1998.

[82] Virginie C. Materlozzo. *Crystallisation and Phase Separation in Colloidal Systems*. PhD thesis, University of Edinburgh, 2001.

[83] R. M. L. Evans, D. J. Fairhurst, and W. C. K. Poon. Universal law of fractionation for slightly polydisperse systems. *Phys. Rev. Lett.*, 81(6):1326–1329, 1998.

[84] J-P. Bouchaud. Aging in glassy systems: new experiments, simple models, and open questions. In M. E. Cates and M. R. Evans, editors, *Soft and Fragile Matter and Nonequilibrium Dynamics and Metastability and Flows*, Scottish Universities Summer School in Physics, pages 285–304. Institute of Physics Publishing, 2000.

[85] W. van Megen, S. M. Underwood, and P. N. Pusey. Nonergodicity parameters of colloidal glasses. *Phys. Rev. Lett.*, 67(12):1586–1589, 1991.

[86] W. Schaert and H. Sillescu. Brownian dynamics of polydisperse colloidal hard-spheres - equilibrium structures and random close packings. *J. Stat. Phys.*, 77(5–6):1007–1025, 1994.

[87] B. Widom. Intermolecular forces and the nature of the liquid state. *Science*, 157:375, 1967.

[88] L. Fabbian, W. Götze, F. Sciortino, P. Tartaglia, and F. Thiery. Ideal glass-glass transitions and logarithmic decay of correlations in a simple system. *Phys. Rev. E*, 59(2):R1347–R1350, 1999.

[89] F. Sciortino, P. Targaglia, and E. Zacarelli. Logarithmic relaxation in dense short-ranged attractive colloids. preprint, cond-mat/0304192.

[90] E. Zacarelli, G. Foffi, F. Sciortino, and P. Tartaglia. Glass-glass transition in dense short-range attractive colloidal systems. preprint, cond-mat/0304100.

[91] F. H. Stillinger. A topographic view of supercooled liquids and glass-formation. *Science*, 267(5206):1935–1939, 1995.

[92] Cécile Monthus and Jean-Philippe Bouchaud. Models of traps and glass phenomenology. *J. Phys. A: Math. Gen.*, 29(14):3847–3869, 1996.

[93] Morrel H. Cohen and G. S. Grest. Liquid-glass transition, a free-volume approach. *Phys. Rev. B*, 20(3):1077–1098, 1979.

[94] N. F. Carnahan and K. E. Starling. Thermodynamic properties of a rigid-sphere fluid. *J. Chem. Phys.*, 53(2):600–603, 1970.